AFFDL-TR-68-148

THE INTERACTION OF LOW-ENERGY ATMOSPHERIC IONS WITH CONTROLLED SURFACES

R. H. PRINCE and J. B. FRENCH

Institute for Aerospace Studies
University of Toronto

TECHNICAL REPORT AFFDL-TR-68-148

DECEMBER 1968

This document has been approved for public release and sale; its distribution is unlimited.

AIR FORCE FLIGHT DYNAMICS LABORATORY
AIR FORCE SYSTEMS COMMAND
WRIGHT-PATTERSON AIR FORCE BASE, OHIO

130

NOTICE

300 - January 1969 - CO455 - 63-1411

AFFDL-TR-68-148

THE INTERACTION OF LOW-ENERGY ATMOSPHERIC IONS WITH CONTROLLED SURFACES

R. H. PRINCE and J. B. FRENCH

FOREWORD

This is the final report of work accomplished by the Institute for Aerospace Studies, University of Toronto, under Contract AF33(615)-3855. This work started on 1 April 1966 and was completed under a one-year extension on 1 April 1968. This was a joint research program between the U. S. Air Force and the Canadian Defense Research Board. The Air Force funding was from Laboratory Director's Funds.

This work was administered under the direction of the Air Force Flight Dynamics Laboratory with James Clark as project scientist. The Air Force portion of this work is a continuation of in-house studies initiated in 1961 by James Clark of various methods for reducing the skin friction drag of aerodynamic bodies. This specific work on Ion-Surface Interactions is concerned with the realization of substantial drag reduction and improved aerodynamics for flight at extreme altitudes and speeds (from transition flow to full orbital flight). Some of the applications of this work in the near future are to longer-lived low altitude observational satellites and to high L/D near orbital vehicles capable of performing efficient orbital plane changes aerodynamically.

At UTIAS, the work was performed by R. H. Prince as the thesis in his Ph.D. program. The work was supervised by J. B. French as his professor and staff advisor.

This technical report has been reviewed and is approved.

H. W. BASHAM
Chief, Control Elements Branch
Flight Control Division
Air Force Flight Dynamics Laboratory

ABSTRACT

The ejection of electrons associated with the Auger neutralization of N_2^+, H_2^+ and N^+ ions at the (100) face of a tungsten single crystal and a polycrystalline molybdenum surface has been studied for the first time in the energy range 10 to 30 eV under controlled surface conditions. The dependence of the electron yields and energy distributions on ion energy has been investigated in detail for the above ion-surface combinations. A detailed description is given of the ion beam used in these studies. Ions are generated in a low-pressure discharge, electrostatically focussed and mass-analyzed by a refocussing magnetic spectrometer to remove undesired ion, neutral and metastable species. The ion kinetic energy spread is low (approximately 0.4 eV at half-maximum) and the beam intensity is as high as 10^{-8} amperes. The combination of ultra-high vacuum techniques to lengthen the time required to reach adsorption equilibrium after flashing, and special guarding and analog data-reduction techniques to reduce instrumentation time response, permitted the study of transient adsorption effects as well as the more usual equilibrium studies. Surface structure has been established by optical and electron-transmission microscopy, and by X-ray back-diffraction. Surface contamination was inferred using the retarding-field diode technique, permitting measurement of work function which is sensitive to surface adsorption levels.

The fact that the electron yields for diatomic ions are considerably lower than those for the inert gas ions treated well by Hagstrum's theory led Propst and Lüscher to propose that the neutralized ion may be vibrationally excited as a consequence of the interaction. They suggested a qualitative procedure by which the inert-gas theory could be modified. In the present report, a quantitative calculation has been performed in this low-energy regime for which kinetic broadening effects may be safely neglected. The simplified theoretical treatment provides good agreement with Propst and Lüscher's data for 50 eV N_2^+ ions on polycrystalline tungsten, using a value of the escape parameter f (the anisotropy of excited metal electrons) taken from Hagstrum's work. A slightly larger anisotropy permits good agreement with the present data for the (100) face of a tungsten single crystal, indicating a stronger focussing of electrons towards the surface normal, a result found by Hagstrum for the case of single crystal semiconductor surfaces. This observation is further substantiated by data for the H_2^+ ion which was chosen because of its great similarity to N_2^+.

TABLE OF CONTENTS PAGE

4. INSTRUMENTATION

LIST OF ILLUSTRATIONS

FIGURE TITLE PAGE

SYMBOLS

Some locally-defined symbols appearing only within a single section are not listed below:

$D(\sigma)$	Number of adatoms desorbed per incident ion (Desorption probability)
D_{15}, D_{30}	Desorption probability for ions of incident energy 15, 30 eV respectively
E	Energy relative to the bottom of the conduction band
E_a (or a)	Maximum Auger electron kinetic energy ($E_i - 2\phi$)
E_d	Energy of dissociation of a molecule
E_F	Energy of the Fermi level relative to the bottom of the conduction band
E_i	Ionization energy of atom or molecule
$E_i'(s)$	Effective ionization energy at surface ion separation s.
E_k	Energy of excited metal electron relative to vacuum level
E_o	Energy of vacuum level relative to bottom of conduction band
E_v	Energy of vibration of excited neutralized diatomic ion
E_x	Electronic excitational energy of ion or atom relative to ground state
e	Electronic charge
f	Fitting parameter describing anisotropy of spatial distribution of excited metal electrons ($f^2 = P_{\Omega_1}/P_{\Omega_2}$)
h	Planck constant
I_i	The true incident ion current at the target ($I_i = I_s + I_T$)
I_s	Current measured at the spherical electron collector
I_T	Current measured at the target
$J_\Omega(\theta_2, E_k)$	Number of free electrons per steradian at angle θ_2 having energy E_k
$J_\Omega(\theta_2)$	Angular distribution of free electrons per steradian at θ_2
k	Boltzmann constant
m	Ion mass

$N(E)$	Density of final states available to excited metal electrons
$N_c(E)$	Density of initial states of conduction band electrons
$N_i(E_k)$	Kinetic Energy distribution of excited metal electrons inside the surface prior to escape
$N_o(E_k)$	Kinetic energy distribution of free(secondary) electrons
$N_v(E_v)$	Vibrational energy distribution of neuturalized molecular ion
$P_e(E_k)$	Fraction of excited electrons of energy E_k which surmount the surface barrier (Escape probability)
$P_{\Omega 1}(\theta_1)$	Angular distribution function of electrons inside surface having finite escape probability ($\theta_1 < \theta_c$)
$P_{\Omega 2}(\theta_1)$	Angular distribution function of electrons inside surface having zero escape probability ($\theta_1 < \theta_c$)
R	Fraction of incident ions reflected without neutralization (Reflection coefficient)
$S(\sigma)$	Fraction of incident gas particles trapped at surface, at coverage σ (Sticking probability)
s	Surface-ion separation
s_o	Most probable surface-ion separation at point of neutralization
$T(E)$	Auger transform
t	time
V	Electric potential (usually with respect to ion source anode)
V_s	Potential of collector sphere relative to target
v	Vibrational quantum number
v_o	Ion velocity

Greek Symbols

α_i	Secondary electron yield per incident ion
ϵ	Base of natural logarithms
θ_1	Angle relative to surface normal inside surface

θ_2	Angle relative to surface normal outside surface
$\theta_c(E_k)$	Critical value of θ_1 beyond which electron of energy E_k is diffracted below surface tangent.
ρ	Dimensionless collector current I_s/I_i
σ (t)	Coverage of surface adatoms (cm^{-2}) at time t after flash desorption
$\sigma_o, \sigma_{15}, \sigma_{30}$	Surface coverage at time t in absence of beam, and with incident beam energies 15 and 30 eV respectively
ϕ	Minimum energy required to liberate conduction band electron (work function)

BLANK PAGE

BLANK PAGE

I. INTRODUCTION

It has been slightly more than a decade since the achievement of Sputnik I extended the flight regime to free-molecule flow, placing the emphasis on gas-surface collisions compared to collisions among molecules. It might be said that the great interest in the area of gas-surface interactions is centered on an attempt, still not yet achieved, to understand and formulate the complex boundary conditions for what are otherwise the simplest of flow fields. It is not unreasonable that the expanding technology which first posed the problems of satellite aerodynamics now permits their simulation in the laboratory, and in particular, this laboratory. The use of high-energy molecular beams to simulate satellite flight and methods of generating them are described in a review by French (1). The energy regime of interest corresponding to a stream of molecules having the directed velocity of satellite flight is 8-15 eV for nitrogen, and since extreme difficulties exist in developing nozzle source molecular beams for energies in excess of 10 eV, ion-exchange beams are an attractive alternative. It was thus natural to consider the construction of this type of beam in conjunction with nozzle source beams, and a low energy ion beam was constructed (2) from a design used by Amdur and Mason(3) and Utterback(4). In the conventional arrangement, the ion beam is permitted to enter a neutralization chamber of pressure of the order of 10^{-4} torr, from which perhaps 10% of the incident ions leave as neutrals and the remaining ions are removed electrostatically. Unfortunately, the effusive neutral flow from such a chamber is so excessive as to make clean-surface experiments with non-inert gases very difficult. A reduction in the chamber pressure merely reduces the proportion of neutralized ions, so that the "signal-to-noise ratio" remains fixed at an unacceptably low level. Consequently, rather than pursue the neutral-surface interaction, it was decided to investigate the ion-surface interaction using satellite-velocity atmospheric ions for which data was almost non-existent. As will be later described in detail, the ion-surface interaction at these energies is essentially ion neutralization and consequent electron ejection to satisfy energy conservation. Information concerning the neutralization process is implicit in the number and energy distribution of ejected electrons. It is the purpose of this thesis to observe these indicators of the neutralization process under varying, but well-established ion and surface conditions. This mechanism is partially responsible for local electron and ion densities different from ambient produced by motion of a satellite at altitudes between 120 km and 300 km and which results in increased effective cross-sections for high frequency radiation. In addition, the net flux of assorted particles and radiation at a satellite surface will determine the surface charge of the vehicle and the nature of the plasma sheath.

The probability of ion neutralization is essentially unity at metallic surfaces, so that with minor reservations concerning directional and energy perturbations, neutral beam scattering experiments of the type performed by O'Keefe and French(5) could be performed using charge-exchanged beams for which the neutralization takes place at the surface itself, removing problems associated with effusive flow, and with at least an order greater conversion efficiency. This point will be discussed more fully in section 6, but it emphasizes the fact that the use of molecular beams as a gas-dynamic tool is a recent development, and is yet another motive for undertaking this type of research. The conventional charge-exchange beam is the result of interest in crossed-beam reaction experiments where no surface interaction is involved, and with the ease of hindsight we can caution against adapting the solution of one specialized area to another.

The study of electron ejection from a metal surface by impingement of ions has received considerable attention in the literature and is summarized by Massey and Burhop(6) and Kaminsky(7). Unfortunately, most of the work performed prior to 1950 is inconsistent due to the unspecified nature of the surfaces involved.

There are two reasonably distinct mechanisms by which electrons may be ejected from a surface as a consequence of ion bombardment. At energies above an ill-defined threshold of several hundred eV, ions eject electrons by a kinetic mechanism in which appreciable momentum is transferred from the ion to lattice atoms and subsequently to bound electrons in a manner that is still poorly understood. Nevertheless, this mechanism exhibits a strong dependence on incident energy in contrast to the mechanism at low incident ion energies which is the so-called "potential" ejection or Auger (radiationless) state transition, described in detail in section 2 and Appendix A.

At this point, it suffices to say that two metal electrons are involved, one of which neutralizes the ion and the other absorbing the energy released by this transition.

A number of theoretical models for this process exist, principally evolving from the experimental and theoretical work of Hagstrum (8-14) which in turn is based on the earlier work of Shekhter(15) and Cobas and Lamb(16). These models are first-order perturbation theories in which the Coulomb interaction between the two participating electrons is the perturbation which causes the transition. A slightly different approach is taken by Propst(17) in that the radiation field established by the neutralizing electron is the perturbation that excites the second electron. The role of the incoming ion is to provide a low-lying vacant electronic level for the Auger process. A new approach using the quantum mechanical theory of scattering has been derived by Wenaas and Howsmon(18) which removes some objectionable elements inherent in the former theories and appears to correctly describe the experimental data. The essential criterion is that the ionization potential, E_i, of the incoming ion must exceed twice the metal work function, i.e. $a = (E_i - 2\phi) > 0$ in order that an external (secondary) electron be produced.

Energy "a" is the maximum kinetic energy attainable by an ejected electron if the mechanism is independent of the ion kinetic energy, and is well substantiated by experimental work.

Aside from the work of Hagstrum, probably only that of Propst and Lüscher(19), Vance(20), and Mahadevan et al(21), can be considered sufficiently well specified with respect to gas adsorption. It is desirable for comparison with theory that the ion energy be as low as possible, and only Hagstrum has used incident ion energies below 50eV. The only work pertinent to the present tungsten experiments is that of Propst and Lüscher who have published data for 50eV He^+, N_2^+, H_2^+ and O_2^+ ions incident on a clean polycrystalline tungsten surface. Vance and Mahadevan have published data for these ion species at a polycrystalline molybdenum surface at energies higher than the present work. There is excellent agreement with the extrapolation of these higher energy results t he pertinent low-energy regime presently considered. A summary of representative secondary electron yields at the minimum published ion energies is shown plotted in Fig. 1 against the "energy excess" for the mechanism ($E_i - 2\phi > 0$) for tungsten and molybdenum surfaces. No attempt to apply a simple linear behaviour to the process is intended (although it is a good approximation), rather the straight line is used merely to illustrate the fact that the yields for diatomic ions are uniformly lower than a corresponding inert gas of similar ionization potential, and that the theory of Auger emission while it can account reasonably well for the inert gas yields does not include a mechanism describing the true behaviour of diatomic ions. It is this behaviour in particular which is of interest in this work, since the atmospheric species N_2^+, N^+ and H_2^+ are considered. Propst and Lüscher (19) made the reasonable suggestion that since diatomic ions have the ability to vibrate and rotate, perhaps the neutralized ion is excited in these modes and that this energy sink is absorbing energy otherwise used in electron ejection. They suggested a procedure by which the inert-gas theory of Hagstrum could be modified to include the possibility of molecular vibration in the final state. A quantitative calculation of the N_2^+-tungsten interaction is given in Appendix A which predicts reasonably well the experimental results of both Propst and Lüscher and the present work.

Although the preliminary ion beam previously described (2) was of adequate intensity and reasonably monoenergetic, the purity was questionable, since the neutral component (possibly excited) as well as undesired ion species remained an integral part of the beam. Magnetic ion selection was subsequently employed in the version described in this report, as well as some re-arrangement of the lens operation.

The experiment has illustrated and emphasized the effects of surface contamination; it has been the aim of this thesis to specify as completely as possible the physical and chemical properties of the target material. Even with this ability it is necessary to perform the desired experiment on a sufficiently short time scale because of gas adsorption. A large amount of effort was spent in perfecting the apparatus to satisfy this requirement with the result that we are able to observe the transient effects of adsorption on the energy distribution functions which to our knowledge is the first time this has been done.

In summary, the intention of the experiment is to obtain data concerning the yields and energy distribution functions of secondary electrons produced at metal surfaces by the impact of atmospheric ions in the satellite velocity regime. In particular, we wish to infer from the observations the likelihood of molecular excitation as a result of neutralization, and to observe the effects of ion kinetic energy and surface contamination on the process.

2. THEORETICAL DISCUSSION OF THE AUGER PROCESS

2.1 Review of the Inert-Gas Theory

In the ion energy range under study, we are concerned with those processes which occur sufficiently far from the surface that primarily the incident particle s potential energy is of interest. There are three possible types of electronic transitions involving an ion near a metal surface namely, resonance, Auger and radiative. We are concerned here with the radiationless (Auger) transitions since the probability of radiation accompanying ion neutralization is extremely low (~ 5 x 10^{-7}) even for ions of thermal energies. This is because the characteristic radiative lifetimes (~ 10^{-8} sec) by far exceed the time spent by the ion in the vicinity of the surface (~10^{-14}sec). The ions must therefore be neutralized by processes involving tunnelling of metal electrons through the surface barrier. Figure 44 shows a sketch commonly used to describe the situation that exists when an ion approaches a metal surface. One electron (2) falls into the vacant atomic level by either process A (Auger Neutralization) or possibly by the two-stage process B (Resonance Neutralization and Auger de-excitation).

The energy released in this transition is then absorbed by a second electron (1). As long as the relative velocity between incident ion and metal surface is much smaller than the orbital velocities of atomic electrons, the neutralization process can be treated as quasi-stationary (adiabatic) by time-independent perturbation theory. In the treatment by Propst (17), the perturbation that excites the second electron is the radiation field established by the first metal electron in falling to the atomic ground state. A second approach, by Hagstrum (10,13), is that the Coulomb interaction between the two participating electrons is the required perturbation. Although in the non-relativistic limit, the two methods are equivalent, the second method has yielded more profitable results to date, and will be considered here.

An entirely different approach, removing the somewhat artificial concept of quasi-stationary calculation of the transition matrix elements, is under consideration by Howsmon and Wenaas (18). This involves the application of the quantum-mechanical theory of scattering rather than the previously-used perturbation theory, but it is difficult at this time to predict the behaviour of other than simple ion species.

It may be argued that although there are excited molecular states available for the resonance neutralization process B, the two-stage process is unlikely on both theoretical and experimental grounds. Firstly, it is clear that the number of participating electron states in the metal is limited and that the variation of energy levels near a metal surface further restrict the possibility of resonance neutralization since such transitions must usually occur at larger ion-surface separations, where the transition probabilities for either process are low. Secondly, the form of the electron energy distributions resulting from Auger de-excitation is quite different from the experimental functions, which closely resemble those predicted on the basis of Auger neutralization alone. Thus the theoretical treatment will be entirely restricted to the consideration of the Auger neutralization process. We wish to calculate the distribution in kinetic energy, N_o (E_k), of electrons outside the metal (the observable products of the phenomenon) in terms of parameters associated with the ion and the metal. The total electron yield, γ_i, is then the integral of $N_o(E_k)$ over all energies E_k. $N_o(E_k)$ is related to the distribution in energy of excited (Auger) electrons inside the metal, N_i (E_k), by a probability of electron escape, P_e (E_k), expressing the fraction of electrons of energy E_k which have sufficient energy and appropriate direction to surmount the surface potential barrier.

The form of $P_e(E_k)$ will depend strongly on the angular distribution of Auger-excited metal electrons prior to escape, but always rises from zero at the vacuum level, $E_k = E_o$, to a value approaching 0.5 at large E_k. The principal adjustment of theory to experiment is provided by parametric variation of this function. All ions approaching the surface will not undergo Auger neutralization at the same distance from the surface, but the probability of neutralization will be distributed in distance s in a peak-shaped function, having a maximum at $s = s_o$. The resulting integration over distance may be avoided if it is assumed that all transitions occur at a single ion-metal separation. This simplifying procedure is equivalent to assuming a mean value of transition distance that is close to s_o without serious effects on the theoretical result. If an exponential rate function is assumed, the width at half-maximum of the transition probability function may be estimated as less than 0.5 A(independent of ion velocity v_o), while the value of s_o is velocity-dependent but of the order of 4 to 5 Å. Furthermore, the over-all probability of Auger neutralization rapidly approaches unity at low values of v_o so that in the energy range under study essentially all ions will participate in an Auger transition before the ion gets close enough for other means of its neutralization to become operative. This result is in agreement with the observation of very low reflection of ions as ions at low incident kinetic energy. Under the above assumptions, the $N_i(E_k)$ distribution will thus be proportional to the product of the number of initial and final states resulting in the excitation of an Auger electron of energy E_k. It is implicit that the transition probabilities are independent of these initial and final states, that is, every combination is equally probable. The dependence of $N_i(E_k)$ on the conduction band state density $N_c(E)$ may now be seen.

Equating the energy liberated by electron (2)(Fig. 44) to that gained by electron (1) leads to a statement of energy conservation:

$$E_1 + E_2 = 2E = E_k + 2E_o - E_i'$$

where E is the mean value of E_1,E_2 and E_i' is an effective ionization energy which will in general differ from the free-space value E_i due to the ion-metal interaction. At large s_o considered here, this interaction is principally an attractive image potential (Coulomb) such that $E_i'(s_o) \approx E_i - 3.6/s_o$ where s_o is in Angstroms, and large with respect to the surface lattice constant. The upper limit on E_k, the kinetic energy of a free Auger electron can now be seen to be

$$(E_k)_{max} = E_a = (E_i' - 2\phi)$$

when both electrons are taken from the top of the conduction band at energy $E=E_F=(E_o - \phi)$. At low incident ion energies, the observed energy maximum of free electrons will thus provide an estimate of E_i' and hence s_o. From the conservation of energy statement, electrons populating the energy interval dE at E_1 and E_2 will produce excited electrons in the element dE_k at $(E_k + E_o)$ as will all pairs of electrons symmetrically located at Δ about a mean energy E. Thus we should expect $N_i(E_k)$ to be proportional to an integral over the product of state densities in the conduction band, that is, proportional to T(E) given by

$$T(E) = \int N_c(E-\Delta)N_c(E+\Delta)d\Delta$$

where the integration stops when either the top or bottom of the conduction band is reached. This is the so-called Auger transform. We further expect the $N_i(E_k)$ distribution to be proportional to the density of final states available to excited electrons, N(E) which has a value only for $E > E_F$. Thus

$$N_i(E_k+E_o) = G.\ N(E_k+E_o).\ T\left[\tfrac{1}{2}(E_k+2E_o-E_i')\right]$$

where G is a normalization factor obtained by setting the area under the $N_i(E_k)$ distribution equal to one electron per incident ion. i.e.

$$\frac{1}{G} = \int_{E_F}^{\infty} N(E_k+E_o).T\left[\tfrac{1}{2}(E_k+2E_o-E_i')\right] dE_k$$

By this means, the theory yields an Auger electron distribution normalized per incident ion, which may be compared with normalized experimental distributions only if Auger neutralization is the only neutralization process occuring.

The problem of how these excited electrons escape from the metal must now be considered. A fraction of such electrons have a component of momentum P_n normal to the surface that exceeds the surface barrier E_o, viz

$$\frac{P_n}{2m} \geq E_o$$

This condition defines a momentum cone of half-angle θ_c where

$$\cos\theta_c = \left(\frac{E_o}{E_o+E_k}\right)^{\frac{1}{2}}$$

such that the momentum vectors of electrons which escape lie within this cone. An alternative view may be obtained by considering refraction of the electron trajectory at the surface barrier. For a given E_k, excited electrons outside the cone defined by θ_c are refracted into the surface plane, and do not leave the metal. If we assume that the angular distribution $P_\Omega(\theta_1,E_k)$ is isotropic, $(=\frac{1}{4\pi})$ the escape probability is then given by

$$P_e(E_k) = \int_0^{2\pi}\int_0^{\theta_c} P_\Omega(\theta_1,E_k)\sin\theta_1 d\theta_1 d\phi = \tfrac{1}{2}\left[1 - \left(\frac{E_o}{E_o+E_k}\right)^{\frac{1}{2}}\right] \quad E_k > 0$$

$$= 0 \qquad E_k < 0$$

The angular distribution is probably peaked in the direction normal to the surface, however, since the theoretical $N_o(E_k)$ distributions obtained for the isotropic assumption are consistently lower than experimentally-measured distributions. We can therefore either assume that the angular distribution resembles an oblate spheroid, or that it is bi-modal having two isotropic but different distributions for θ less than or greater than θ_c. The latter technique is employed here, since the resulting fitting parameter (the ratio of these probabilities) is readily comparable with other work. The artificial discontinuity in angular distribution is not as serious as it seems, since integration over angles removes the dependence on the form of the angular distribution. By setting $f^2 = P_{\Omega 1}/P_{\Omega 2}$ where $P_{\Omega 1}$ and $P_{\Omega 2}$ are the angular probability functions for $\theta < \theta_c$ and $\theta > \theta_c$ respectively (Fig.49), we may derive a parametric escape function

$$P_e(E_k) = \frac{1}{2}\,\frac{1-\left(\dfrac{E_o}{E_o+E_k}\right)^{\frac{1}{2}}}{1-\left(1-\frac{1}{f^2}\right)\left(\dfrac{E_o}{E_o+E_k}\right)^{\frac{1}{2}}} \qquad E_k > 0$$

$$= 0 \qquad E_k < 0$$

We expect the parameter f to describe the "focussing" of excited metal electrons by atom centres, and should thus be a strong property of the solid itself, and depend weakly on the particular ion-surface combination. In terms of the above function, we may now calculate the external electron energy distribution function $N_o(E_k)$ as

$$N_o(E_k) = Ni(E_k + E_o) .\ P_e(E_k)$$

and the total yield γ_i as

$$\gamma_i = \int_0^\infty N_o\,(E_k)dE_k$$

This procedure of calculation omits several mechanisms which broaden the energy distribution $N_o(E_k)$, principally the dependence of transition rate on distance and the finite lifetimes in initial and final states (Heisenberg broadening). These effects are difficult to incorporate from the outset of the derivation. It is simpler to neglect these effects and calculate a simplified solution which may be modified at a later stage by convoluting the Auger transform T(E) with a Gaussian function which accounts for the several broadening mechanisms.

It may be stated here that only by this means can the effect of ion kinetic energy be incorporated into the theory.

This procedure is valid for low incident ion energies, but for the very low energies considered in the present work the value of considering broadening effects is questionable. Further comments will be made on this subject in Sec. 2.2, and Appendix A.

2.2 Extension of the Theory to the Case of Diatomic Gas Ions

It was hypothesized earlier that the failure of the relatively successful inert gas theory to predict the observed electron yields for diatomic gas ions was due to vibrational excitation of the neutralized molecule. Vibrational excitation only is considered because the energy quanta are large compared to those for rotation, but in addition the vibrational periods ($\sim 10^{-14}$ sec) are compatible with the time scale of the interaction. The rotational periods are typically two orders greater in magnitude. For the purposes of discussing this process, it is somewhat more convenient to consider rather than the system of Fig.44, one comprised of the incoming ion and all electrons in the metal (taken as n in number). This state is transformed into the isoelectronic system of the neutralized molecule (possibly excited), a free electron, and (n-2) metal electrons. Hence, we may write for the initial state (Fig.45) considering the case of diatomic nitrogen,

(A) $N_2^+ + ne_m$ N_2^+ ion in ground state, n metal electrons

The final state will lie intermediate to systems (B) and (C) below.

(B) $N_2+(n-2)e_m+e_k$ N_2 molecule in ground state, (n-2) metal electrons, 1 free electron

(C) $2N+(n-2)e_m+e_k$ Two N atoms in ground state, (n-2) metal electrons, 1 free electron

The potential curves corresponding to the above systems may be represented as in Fig. 45, realizing that the exact shapes of the curves are unknown, but that the representations may be qualitatively useful. For large ion-surface separations, the potential energy of state (A) is assumed to be zero, and independent of the ion kinetic energy. The attractive portion of the interaction potential is due to the Coulomb (image) forces, while the repulsive (Pauli) interaction at close range is due to atomic core overlap. For the ion-surface separations of interest, however, the interaction potential is closely given by the 1/s dependence alone. System (B) is derived from the first by removing an electron from the metal to neutralize the ion, and absorbing entirely the excess energy with a second (excited) metal electron. If both electrons are taken from the Fermi level, then at large separation, the potential of state (B) is $(E_i-2\phi)$ below the first (i.e. the excited electron has a maximum energy). There are, however, n^2 combinations of the two electrons possible, corresponding to a band of energy states extending upwards from the latter curve to that representing the case of both electrons taken from the <u>bottom</u> of the conduction band. For every such potential curve there is in addition a band of vibrational states extending upwards to state (C) which is displaced from curve (B) by the dissociation energy of the nitrogen molecule, 9.8eV*. The potential well for state (C) has a depth 8.4 eV which is twice the binding energy of a nitrogen atom at a tungsten surface. From energy conservation, only those final states lying below state (A) can result in the formation of a free electron. Under the assumption that the Franck-Condon principle is valid, transitions occur vertically at a given ion-surface separation, s, so that the energy interval between such a final state and state (A) is the electron kinetic energy E_k. This is equivalent to assuming that the electronic transition affects neither the position nor the momentum of the molecule.

It may be seen in Fig. 45 that dissociation of the molecule is not possible at large s_0 but is conceivable at close proximity due to the relatively large binding energy of the nitrogen atom to the surface. It is also apparent that the maximum kinetic energy of excited electrons may exceed or be less than the value $(E_i-2\phi)$ depending on the detailed nature of the molecular interaction potentials at close range. The effect of the vibrational states will be to produce a large increase in the density of the final states lying close to the initial state (A). Transitions to these states will result in excited electrons of lower average energy and hence lower probability of escape. The electron yield should therefore decrease in accordance

---

* There is some doubt concerning the dissociation energy of the nitrogen molecule. Assuming the dissociation products $^2D + {}^4S$ the value is 9.8eV, while a more popular choice is $^2D + {}^2D$(7.37 eV)(47).

with experiment. We will attempt to quantitatively calculate the new $N_o(E_k)$ distribution without knowledge of the close-range interaction (large s_o) by modifying the procedure used by Hagstrum (10,13) described in summary in section 2.1. We again assume that all transitions are equally probable, and further stipulate that the molecule is not dissociated by the interaction, ensuring ion kinetic energy conservation. The energy available for excitation is at most $[E_i\ (s_o)-\phi\ ]$ so that only at large s_o is dissociation energetically possible; the transition probabilities are low in this case and it is unlikely that the <u>entire</u> energy excess is absorbed by the molecule alone. Small anharmonicity of the vibrational oscillator may be included by writing the vibrational energy levels as (44)

$$E_v = hc\omega_e\ (v + \tfrac{1}{2}) - hc\omega_e x_e\ (v + \tfrac{1}{2})^2 + \ldots\ldots$$

where v is the vibrational quantum number, ω_e is the vibrational wave number (2360 cm^{-1}), $\omega_e x_e$ is the anharmonic constant (14.46 cm^{-1}), c is the velocity of light, and $\hbar$ is Planck's constant. As shown to scale in Fig.45, vibrational quantum numbers up to v=25 are possible at large s_o, although this value may be exceeded if the transition occurs at close range (in general, at high incident energies). With the consideration of vibrational excitation, the vertical displacement from initial to final state becomes the sum of E_k and E_v. For a given value of E_v, there is a probability density function $N_v(E_v)$ which is proportional to the number of permissible states of electron energy E_k, subject to the inequality

$$E_i - 2E_o \leq (E_k + E_v) \leq E_i - 2\phi$$

This is an expression for the range of states available for final state (B); a negative value of E_k is permissible, but implies that the electron cannot escape the surface barrier. The density of final states available to excited electrons is N(E) so that

$$N_v(E_v) \quad = \quad C \int_{E_F}^{(E_i - 2\phi\ +\ E_o - E_v)} N(E)dE \qquad 0 \leq E_v < E_d$$

where the upper bound is obtained from the above inequality and is a function of E_v itself. The result of this calculation for a 1/2 power N(E) distribution is shown in Fig.46. It is a distribution favouring low vibrational excitation as expected, and is truncated at the dissociation limit. For E_v above $(E_i - 2\phi)$ the production of an external electron is not possible. The energy conservation equation now becomes

$$E_1 + E_2 = 2E = (E_k + E_v) + 2E_o - E_i'$$

so that in calculating the number of initial states resulting in an excited electron of kinetic energy E_k, the appropriate Auger transform is now

$$T\left[\tfrac{1}{2}\ (E_k + E_v + 2E_o - E_i')\ \right]$$

The inclusion of vibrational excitation results in a shift of the Auger transform to lower energies providing the mathematical means by which the total electron yield is reduced. Since numerous values of E_v are possible for a given E_k, we must weight the Auger transform by $N_v(E_v)$ and integrate over all permissible values of E_v. Similarly, in calculating the number of final states available for a given E_k, we must consider that for each value there are a number of values of E_v such that the level has a degeneracy $(v_k + 1)$ where v_k is the vibrational quantum number corresponding to an energy of (E_a-E_k) or E_d, whichever is smaller. The formulation for the distribution of excited electrons prior to escape thus becomes

$$N_i(E_k+ E_o) = G.(v_k+ 1)\, N(E_k+ E_o)\int_{E_v} N_v(E_v)\; T\left[\tfrac{1}{2}(E_k+ E_v+2E_o-E'_i)\right]dE_k$$

where G is again a normalizing constant so that we obtain one excited electron (which may or may not escape) for every incident ion. Using the parametric escape function $P_e(E_k)$ we again obtain the observable free electron distribution function

$$N_o(E_k) = N_i(E_k + E_o).\ P_e(E_k)$$

In Appendix A, specific expressions for these functions are calculated for the $(N_2^+ - W)$ system at low incident ion energies. These results should also be applicable to the $(H_2^+ - W)$ system since the ionization potentials are nearly identical. Furthermore, although the dissociation energy of N_2 is twice that of H_2, the vibrational levels are approximately twice as dense, so that we expect approximately the same results.

Although the spatial distribution of free electrons was not experimentally obtained due to the small current levels available, an estimate of the form of this distribution was attempted. With reference to Fig. 49, consider an electron inside the metal approaching the surface at angle θ_1 with respect to the surface normal, at polar angle ϕ, and possessing energy $(E_k + E_o)$. The trajectory undergoes a refraction at the surface, so that the free space angle θ_2 is given by

$$1 - \frac{\sin^2\theta_1}{\sin^2\theta_2} = \frac{E_o}{E_o+E_k}$$

From this relationship, we previously obtained the critical angle θ_c (a function of E_k), for which the angle $\theta_2 = \pi/2$. The probability that an electron is found in a solid angle $\sin\theta_1 d\theta_1 d\phi$ with energy (E_o+E_k) is proportional to the excited energy distribution $N_i(E_o+E_k)$ and the parameteric angular probability function $P_{\Omega_1}(E_k)$ given by

$$P_{\Omega_1}(E_k) = \frac{1}{4\pi}\left[1- \left(1- \frac{1}{f^2}\right)\left(\frac{E_o}{E_o+ E_k}\right)^{\frac{1}{2}}\right]^{-1}$$

Hence, the number of electrons in this elemental solid angle prior to escape is

$$N_i(E_o+ E_k).\ P_{\Omega_1}(E_k)\,\sin\theta_1 d\theta_1\, d\phi\, dE_k$$

These electrons are refracted into an elemental solid angle $\sin\theta_2 d\theta_2 \, d\phi$ outside the surface related to the former solid angle by a realtionship obtained from the diffraction equation, namely

$$\sin\theta_1 d\theta_1 = \left[1 - \left(\frac{E_o}{E_o+E_k}\right)\right]\left[\frac{\cos\theta_2}{\cos\theta_1}\right]\sin\theta_2 \, d\theta_2$$

The number of electrons per unit solid angle at θ_2 due to electrons characterized by (E_o+E_k) and θ_1 is thus

$$J_\Omega(\theta_2,E_k) = N_i(E_k+E_o) . \; P_{\Omega_1}(E_o+E_k)\left[1 - \left(\frac{E_o}{E_o+E_k}\right)\right]\left[\frac{\cos\theta_2}{\cos\theta_1}\right] dE_k$$

To obtain $J_\Omega(\theta_2)$ the total number of electrons per unit solid angle at θ_2 (the form of an experimental measurement) we would like to integrate over all energies. However, we cannot separate physically (or mathematically) the variables θ_1, E_k since any combination yielding the same value of θ_2 through the diffraction relation are equivalent for purposes of calculating the total flux. Consequently, we must sample points uniformly from the distribution of these two variables, and sum over all combinations yielding electrons in $d\Omega_2$ at θ_2, viz.

$$J_\Omega(\theta_2) = \sum_{(\theta_1 E_k)\rightarrow\theta_2} J_\Omega(\theta_2,E_k)$$

The incremental angles $\Delta\phi_1$ must be chosen so that we sample uniformly in solid angle-space since only the probability <u>density</u> $P_{\Omega_1}(E_k)$ is independent of θ_1 and not the <u>number</u> of electrons found in a unit solid angle at θ_1. The details of this procedure are given in Appendix A and Fig. 52. The result is that the angular flux $J_\Omega(\theta_2)$is definitely non-cosine in nature, possessing a strong lobe towards the surface normal. Although the scatter is large due to the selection of a relatively large sampling unit, the distribution is reasonably well approximated by a spiral, i.e.

$$J_\Omega(\theta_2) \simeq K\left(\frac{\pi}{2} - \theta_2\right) \qquad 0\leq\theta_2\leq\frac{\pi}{2}$$

A cosine distribution normalized to the same area is shown for comparison.

3. EXPERIMENTAL APPARATUS

3.1 Description

The apparatus used is shown pictorally in Figs 2,3 and schematically in Figs 4,5. Figure 2 stresses the instrumentation involved and shows the two equipment racks, the left one being principally the vacuum system controls (getter-ion pump control units, bakeout control and pressure gauges), and the right one primarily ion beam and experimental instrumentation. Figure 3 shows clearly the ion beam envelope and the experimental flange which is designed so that the entire target assembly may be withdrawn intact with its electrical connections. Figure 4 is a schematic diagram of the apparatus showing the location of internal components. Briefly the system operates as follows. Gas is admitted from storage bottles through a metering valve into the ion source, where ionization by electron impact is performed. Ions are extracted from the source and accelerated to an energy suitable for magnetic mass analysis by the 60-degree sector-field analyzer. The desired ion species is subsequently decelerated and focussed in two stages on the target T. Secondary electrons produced by this interaction are energy-analyzed by applying varying potentials to the collector sphere S, and observing changes in the collector sphere current I_s. The target assembly is shown in detail in Fig. 5, and contains devices for both removing adsorbed gases and detecting their presence.

3.2 Vacuum System

The apparatus may be conveniently separated into three distinct pressure regions: the ion source, lens system, and interaction chamber, of which only the latter requires ultra-high vacuum techniques. For reasons described in the next section, the most suitable pressure for the ion source is in the 10^{-3} torr range, so that the intervening regions prior to the interaction chamber must reduce the background pressure by approximately six orders of magnitude. The charge-retention property of vacuum pump oils eliminates standard oil-diffusion pumps from use in this type of apparatus, since even with heavy trapping (which is both expensive and inefficient) a surface film of oil will almost certainly form on the lens surfaces.

If the beam were to strike such a surface, charge will be retained, violating a basic assumption of electrostatic lens theory that the lens surfaces are equipotential. The effect is an oscillation of the beam intensity and position with a time constant of the order of minutes. The alternatives are getter-ion pumps or trapped mercury diffusion pumps.

The former were chosen because of simplicity of operation without the necessities of constant fore-pumping and trapping, immunity from power line failures and the high degree of cleanliness possible. There are disadvantages, however, and these include high cost, low pumping speeds for inert gases (which can produce pressure instabilities), stray magnetic fields and backstreaming of the "working fluid", charged particles. The latter two factors were of some concern in this work. Two 75 ℓ/sec diode pumps were used for the lens and spectrometer regions as shown in Fig.4, and a 100ℓ/sec pump of the newer triode type for the interaction chamber. The .010" dia, orifice separating the ion source from the second lens region is a compromise between the magnitude of the extracted ion current and the gas load on the 75ℓ/sec pump required to maintain a sufficiently low pressure in the lens such that elastic scattering is negligible.

The entrance and exit apertures of the mass spectrometer (8 mm. dia) may then be used to differentially pump the remainder of the system. The entire vacuum envelope is constructed of type 304 stainless steel, and bellows are incorporated to permit alignment of the various sections utilizing external adjustment screws. The bakeable ultra-high vacuum interaction chamber is approximately 18 inches in diameter and is sealed using copper-gasketed shear-type flanges of the commercially available type, with the exception of the upper lid of the chamber which is sealed using an OFHC copper O-ring under a compressive loading of approximately 2,000 lbs/linear inch. The remainder of the vacuum system is sealed using viton O-rings which are not bakeable beyond 200°C, but which permit the voltage isolation of the ion source and spectrometer tube, which are not at ground potential. Mylar sheet is used to prevent electrical contact of these flanges, and appears to be a material compatible with vacuum in the 10^{-9} torr to 10^{-8} torr range. The remaining insulators in the unbaked portion of the apparatus are of Teflon, while boron nitride has been used exclusively in the bakeable chamber.

The pump-down procedure is as follows: A rotary two-stage mechanical pump (Welch 1402) in series with an efficient liquid-nitrogen trap is used to reduce the system pressure to approximately 10^{-3} torr, at which time the isolation valves may be closed and the three getter-ion pumps should readily start. After approximately 30 minutes have elapsed from the commencement of the pump-down procedure, the system pressure is 10^{-6} torr or better, and overnight will further drop to 10^{-8} torr or less, depending on the nature of contamination introduced. Strip heaters of 6 kw capacity are attached to the interaction chamber permanently, and are turned on at this time. The heaters are thermostatically controlled, and may be applied in a timed cycle with the protection of an interlock with the getter-ion pump control. Thermocouples are attached at several points on the chamber surface to monitor temperature variations with location and time.

Although the heaters are capable of raising the chamber temperature to 450°C (and have done so), it is preferred to set a ceiling of 300°C and extend the baking period to perhaps 24 hours. Considerable difficulty was experienced with cracking of the large upper seal during cool-down, if the baking temperature exceeded this limit. It appears that the OFHC copper ring suffers excessive creep and permanent set at these elevated temperatures and loads. This limitation is of little consequence in the present case since the attainable base pressures are dependent on the pressure-time product in the baking period and not the absolute temperature level.

If the standard precautions concerning the handling of components have been followed, the base pressures in the system, as read by the getter-ion pump control units are $\sim 5 \times 10^{-9}$ torr in the unbakeable sections are $\sim 5 \times 10^{-10}$ torr in the bakeable interaction chamber rising into the 10^{-9} torr range during beam operation.

No special precautions were taken concerning the purity of the source gas, since the installation of a magnetic ion analyzer removes the danger of beam contamination. The metering valve is in series with a shut off valve, however, so that the inlet line may be evacuated ensuring the inlet gas is up to the stated commercial high purity level. This is of little consequence, since as is described in Sec. 2.3.3. the major source of ionic impurities prior to magnetic analysis is due to the evolution of gases from within the vacuum system itself.

Finally, a baffle to prevent electrons and radiation emitted from the getter-ion pump from reaching the collector sphere was installed, which operated most efficiently if maintained approximately +300 volts above ground. The positive potential deliberately attracts such electrons and although the secondary electron yield is greater than unity, the electrons produced at the baffle have insufficient energy to escape. By contrast, if the baffle is made electron-repelling, the efflux will be slightly reduced, but the backstreaming electrons will merely be deflected and strike the lower surface of the interaction chamber where their numbers will increase at the first collision, since the sum of reflection coefficient and secondary electron yield exceeds unity. The latter point is illustrated by the fact that although the high voltage within the pump body is negative (electrons are effusing to ground potential above), the net current reaching the baffle at ground potential is positive (approx. 2×10^{-2} amperes/torr). This is possible since the electrons have energies of several hundred eV as determined by biasing the baffle. For most metals γ_e is unity at incident electron kinetic energies of 200 eV.

By applying a positive bias of several hundred volts, the spurious current reaching the collector sphere from this source was reduced from 5×10^{-5} amperes/torr to about 5×10^{-7} amperes/torr which is well below the noise level of the instrumentation at the operating pressures.

3.3 Ion Beam

3.3.1 Ion Source

The operation of the ion source has been described in considerable detail in Ref.2, and only a review of the important aspects will be included at this time. The operation of the source may be classified as ionization by electron impact in a low-pressure discharge of the Townsend type, in which an electron source (heated filament) is required to maintain the discharge. The electron energies are restricted to less than 30eV to limit the production of metastable ions, although the production of metastable molecules is optimized at these energies. In addition to ionizing electron-molecule collisions, a number of secondary emission processes are active at the cathode, such that a considerable enhancement of the discharge current occurs, most of which is ion current. The main objective is to produce a monoenergetic ion beam of sufficient intensity, and since the final ion energy at the target is determined by the sum of its initial kinetic energy and the source-target potential drop, we demand that the ion temperature in the source be maintained close to room temperature and that the extracted ions are formed in a region of small potential gradients. The former restraint implies that the source plasma be highly diffuse without electron-ion thermalization, and the latter that the extraction field penetrating the source should be weak. In the absence of plasma or space charge effects, the final ion kinetic energy distribution will be determined solely by the fringing electrostatic field established by the extraction electrode outside the source orifice, and will lie entirely at energies less than the nominal energy indicated by the source-target potential drop. At high electron beam currents and low source pressures we would expect a negative space charge depression of the potentials in the source that would shift the ion kinetic energy distribution to lower energies by several volts. As the gas pressure in the source is increased, ionization will yield sufficient positive space charge to cancel the electronic space charge. Hagstrum(8) has in fact observed the ion kinetic energy distribution to <u>exceed</u> the nominal value due to this effect. In the present experiment, it is believed that all three effects are active, since although the electron current is sufficiently high that space charge effects are present (established by observing the source voltage-current characteristic in the absence of the source gas), the maximum in the ion kinetic energy distribution lies only slightly (approx 0.75 eV) below the anode potential.

The typical operating conditions are filament-to-anode potential difference 30 volts, discharge current 100 ma., source pressure 10^{-3} to 10^{-2} torr, and extracted ion current approximately 10^{-7} amperes maximum. The cathode is a spiral-wound tungsten wire of .010" dia., and is heated by a regulated current of approximately 8 amperes DC.

Since it is pertinent to the operation of the ion source, the effect of charge-transfer ions on the kinetic energy distribution should be mentioned. The region immediately outside the source orifice is relatively dense since the source is generating a classical room-temperature molecular beam in addition to the extracted ion flow. Ions moving along the beam centerline with low energies at this point are highly capable of symmetric charge transfer reactions (4) which result in the formation of a second family of ions, distinctly separated in energy from those formed within the source at the nominal beam energy. If this region has a positive potential relative to the target it is possible for these ions to reach it, but in a poorly-focussed manner since the lens potentials are established for the principal family. This effect has been deliberately observed, and substantiated by the observation that the relative populations in the two groups is sensitive to the extraction potential and the source pressure. It is a simple matter to ensure that the potential structure does not favour this effect, and the required extraction potential can be readily estimated by requiring that the centerline potential at the source orifice (which may be derived from Ref. 26) be below target potential. By the latter analytic method, or by observing the required extraction potential such that the location of the low-energy charge transfer family is shifted below target potential, a minimum extraction kinetic energy of about 30 eV is required to ensure no charge-exchange ions in the beam at final focus.

3.3.2 Lens System

The ion beam on leaving the ion source is subjected to the action of four electrostatic lenses of various types, for which a detailed description is available in Ref. 26 for example. The electrostatic lens charts referring to point-focus lenses of circular cross-section to be found there are derived from electrolytic tank or rubber models and are in a form readily adaptable for design of lenses in the absence of space-charge effects. Lenses having rotational symmetry about the lens axis were used throughout the present apparatus because of their well-established properties and ease of manufacture and alignment. There is also a focussing action of sorts obtained in the double-aperture lens consisting of the source orifice and the .080 inch orifice in the extraction electrode which draws ions from the discharge(1st lens)

Attached to the extraction electrode is a 10 cm. cylinder, 43 mm. inner diameter, which together with the following concentric cylinder of length 24 cm. and 34 mm. inner diameter constitutes the second lens, (Fig.4). The second tube is mounted on the aperture plate at the spectrometer entrance so that the gap between the cylinders permits pumping of the lens interior by the 75 l/sec getter-ion pump below. The first lens produces a virtual image on the source side of the apertures, so that a diverging cone of ions enters the second lens which is accelerated to a nearly parallel focus at the spectrometer entrance. The appropriate lens voltage (kinetic energy) ratio is about 6.3 compared to the chart value of about 7, so that at this point, the beam has been accelerated to approximately 200 eV and is focussed to a 4 mm diameter spot. We may neglect the existence of the mass spectrometer until the next section, since it is a refocussing type which reproduces the convergent beam at the exit aperture where the 200 eV beam diverges into the next lens. The ion beam is now decelerated by the 3rd and 4th lenses to the desired incident kinetic energy. The third lens is a two-cylinder lens consisting of identical tubes 18 cm. long and 34 mm. inside diameter, with an axial separation of 3 mm, and operated at a voltage ratio of about 4. An aperture plate is attached to the second tube, and constitutes one half of the double-aperture 4th lens which may be operated at a variable voltage ratio from 3 to 15 with very little change in focal length, provided the ion beam is nearly parallel at entry. Both apertures are 8 mm, in diameter and are separated by the same dimension. The second aperture plate is very close to the collector sphere which, when used to retard electrons emitted from the target, will have a slight focussing effect. The insensitivity of the 4th lens focal length (40 mm) to the voltage ratio enables the maintenance of beam focus under these conditions. The other advantage of this configuration is that the low energy beam need not be transmitted over a long distance which permits higher space-charge-limited current levels. For a given geometry and ion energy there is an upper limit to the current which may be transmitted, and it may only be attained if the initial convergence of the charge column is in accordance with the Universal Beam Spread Curve (27). The extent to which these considerations apply is discussed in Sec. 3.3.5, however, it may be stated here that we have attempted to match this upper limit throughout the lens system. It is of no avail to exceed the space-charge limit of a subsequent stage, in fact it can be undesirable since it implies that particles will strike lens surfaces and apertures.

After some initial evaluation of the lens system in a moderate-vacuum test facility, no further mechanical adjustments were deemed necessary in the completed system.

The lenses operate at fixed geometry, and focus is achieved by adjustment of potentials supplied by a voltage divider network incorporating high resolution potentiometers (Bourns series 3640).

3.3.3. Mass Spectrometer

In order to study the interaction of ions with surfaces as proposed in this experiment, it is imperative that the surface is bombarded with a single, known ion species, and that unwanted uncharged components are effectively removed. The main concern here is that metastable molecules, which are produced copiously by an impact-type ion source operated near threshold, are completely prevented from reaching the target. The products of metastable de-excitation at a surface are highly similar (if not identical (10)), to those of the ion neutralization process under study. It is also important that the desired ion species be in a known state with regard to rotational, vibrational and electronic excitation. This latter point will be discussed in section 6.3. The requirements indicate that a deflection instrument should be used, and not an in-flight device such as a crossed electrostatic and magnetic field analyzer. Furthermore, since the ion beam is divergent on entering the analyzer, higher transmission of the instrument will be obtained if direction-refocussing is employed. Although this effect was first observed by Dempster in 1918 using a 180 degree deflection field, it is a general property of wedge-shaped magnetic fields for which the particles are refocussed at a deflection angle equal to the angle between the field boundaries. If a divergent beam of ions of equal momentum enters the magnetic field perpendicular to the field boundary, and is deflected such as to leave the field normal to the other field boundary, there will be refocussing of the ion paths as described analytically by Stephens (28). The nature of the focussing is such that the entry and refocussing points are colinear with the apex of the wedge-shaped field.

For ease of beam operation, it is desirable that all potentials remain fixed so that by varying the magnetic field strength any desired ion species may be focussed onto the target. An electromagnet was constructed similar to one described by Nier (29), and is capable of deflecting ion species up to 50 a.m.u. The mean radius of curvature of the instrument is 5.5 inches, and the pole gap spacing is 13/16 inches, allowing a small clearance around the vacuum envelope which is reduced to a thickness of 3/4 inch at this point. The yoke and pole pieces are constructed of commercially pure core iron, and the field intensity is supplied by two inter-changeable series-connected coils each containing 160 turns No.16 awg enameled copper wire. The coil resistance is approximately 1 ohm, so that the power is delivered at low voltage and high current, which makes a solid-state constant-current supply ideal for the purpose. The flux density obtained by this method is linear with coil current in the range of interest from 100 to 800 gauss and has the value 143 gauss/ ampere and a remnant flux density of about 30 gauss. This calibration was performed at the centre of the pole face using a Hall-effect probe (Bell No. BH-206), which was also used to obtain a flux density traverse along the beam trajectory.

The fringing of the field is such that the flux density is reduced to 1/ϵ times the peak density at about one pole gap spacing beyond the pole boundary. Allowance was made for this in estimating the location of the wedge -field boundaries, and in addition the entire electromagnet is radially adjustable so that the instrument transmission may be maximized. No shimming of the pole pieces was attempted since as pointed out by Stephens (28), this field inhomogeneity fulfills to some degree the conditions for third-order refocussing and is not disadvantageous. The remnant flux density profile was similar in shape, and it was not found necessary to reduce it at any time. The required magnetic flux density is given by

$$B^2 = \frac{2.08 \times 10^4}{r} \cdot V \cdot \left(\frac{m}{e}\right) \qquad (\text{gauss})^2$$

where V is the spectrometer voltage with respect to the source, r is the trajectory radius (cm) and (m/e) is the mass-to-charge ratio in a.m.u. For the present case, this expression reduces to

$$B = 147 \left(\frac{m}{e}\right)^{\frac{1}{2}} \quad (\text{gauss})$$

for the spectrometer at 200 volts. Mass spectra may be thus accurately obtained by using the Hall probe output mentioned earlier to locate mass number on the abcissa on an X-Y recorder without introducing the non-linearities of the coil voltage-flux dnesity relationship. The mass-resolution of the instrument is limited primarily by the aperture dimensions relative to the radius of curvature, secondly by the inherent momentum spread of the incident ions and only slightly by the initial divergence of the beam. Using relations developed by Stephens (28) we can analytically account for the observed mass resolution $\Delta m/m$ of about 0.03. The energy spread permitted by the exit aperture is approximately $\Delta E/E = .025$ so that the analyzer performs no velocity-filtering function on a given ion species, since the beam energy spread is typically much less (Sec. 3.3.4).

Typical ionic spectra obtained by magnetic analysis are shown in Figs. 6 and 7 for nitrogen and hydrogen sources respectively, and some discussion appears in section 3.3.5.

3.3.4. Beam Performance

The ion beam has been repeatedly operated using N_2 and H_2 as source gases at energies up to 30 eV, and the intensity obtained at final focus as a function of the ion kinetic energy there is shown in Fig.9. The divider network used to supply lens potentials has been referenced to the ion source, so that the ion kinetic energy at locations other than the target is independent of the anode potential. This convenient arrangement permits the ion beam energy (anode potential) to be continuously varied while maintaining lens focus, as illustrated in the figure. The behaviour of the intensity-energy curve suggests that at low energies there are space-charge repulsion effects in the final lens since the ion energies are <u>fixed</u> elsewhere in the system. A 3/2-power curve is shown for comparison. At higher energies, the intensity is limited by the number of ions generated in the source, and the fraction of these transmitted by the mass spectrometer. In fact, above 20 eV kinetic energy, the beam intensity is almost constant at about 6×10^{-9} amperes (approx. 3×10^{10} ions/second) which is the "emission-limited" value. The intensity is stable over a period of many minutes and except for electrical fluctuations, variations are due to drift in the ion source properties of emission current, pressure and gas composition.

The intensities obtained for the N^+ species are a few percent of those for N_2^+ due to the low ratio of cross-sections for 30 eV electrons while the maximum H_2^+ intensity is of the order of 10^{-9} amperes. It is lower partly due to the lower ionization cross-section but mainly because the mole fraction of H_2 in the source will not reach the level attainable for N_2 which is the major impurity constituent among others in that portion of the vacuum system. (see Fig.7 for example). No evidence of H^+ ions was observable outside the source, although under conditions described in Sec. 3.3.5. relatively high concentrations of the tri-atomic H_3^+ ion could be produced. The kinetic energy spread of the beam was estimated by retarding the ions at the target. The resultant distribution function is highly similar to that reported previously (1,2), and is independent of the particular nominal energy.

The distribution exhibits a decay towards lower energies characteristic of the source potential distribution such that the width at half-maximum is 0.4 eV, with 50% of all ions within a 0.5 eV range, and 90% within a 2 eV range of energies.

There are limitations to the apparatus that should be emphasized. Although the majority of ions are well-focussed at the target to perhaps a 3 mm. dia, spot, the variation of beam focus with ion energy is such that at about 10 eV the fraction of incident ions missing the target and striking the secondary electron collector has reached a few percent. The apparatus is then unsuitable for electron-emission yield studies since the typical values of γ_i

are of this order. Furthermore, the beam focus will deteriorate at higher energies if strong negative potentials are applied to the electron collector sphere as in the electron-retarding field analysis. These considerations have limited the study of electron energy distributions to those for ions of 15 eV kinetic energy or greater, for which negative potentials of up to 8 volts may be applied to the spherical collector without serious lens failure. The total yields may be obtained to slightly lower energies, however, since the sphere is electron-attracting in this mode. The lens failure is more rapid for the lighter ion species which suggests that the mechanism is at least partly megnetic in nature, most likely due to the stray getter-ion pump fields. The above constraints do not apply if the beam is to be used in a field-free environment for aerodynamic simulation, for example. For this purpose, flux simulation of up to 3×10^{11} ions/cm^2- sec is possible, at 3eV or greater.

3.3.5. Discussion and Remarks

The ion spectra of Figs. 6 and 7 always contain, though in variable proportions, a group of peaks from mass number 12 to 19 which is present regardless of the inlet gas source. They must therefore be characteristic background gases in the source, either desorbed from the cathode filament or by the discharge, or evolved from the getter-ion pump. Getter-ion pumps are known to liberate not only gases inherently trapped within the electrode structure but also gases that have been previously pumped. An extreme illustration of the latter is the so-called Argon-instability characteristic of all getter-ion pumps in varying degree. Stainless steel even at room temperature is a source of hydrogen, and accounts for the predominantly hydrogen background found in the bakeable interaction chamber about which we shall have further comment in section 4.3.2. Evolution of gases from either the surface or bulk of metals heated in pumps and the source can account for the ethane-methane group of C^+(12), CH^+(13), CH_3^+ (15), CH_4^+ (16) as well as ammonia NH_3^+ (17). Oxygen appears both as a diatomic ion O_2^+ (32) and as the atomic species O^+(16) as well as reacting with the source gas producing NO^+(30) and as observed by extending the normal (m/e) range, also in the oxide forms N_2O^+(44) and NO_2^+(46). Water vapour H_2O^+(18) and its radical OH^+(17) are both to be expected, as well as fluorine (19) which can be attributed to the teflon insulation and viton O-rings used in the unbakeable sections. When using hydrogen as the source gas, this group remains present, but in addition we observe two peaks of roughly equal peak height at mass numbers two and three. Although it would be desirable to produce atomic hydrogen ions in such large concentrations it cannot be expected from the cross-section ratio which is only a maximum of .005 at the optimum electron energy of over 100 eV. Nevertheless, it was initially proposed that the peaks were in reality at mass number 1 and 2, and that the spectrometer behaved in some non-linear fashion at low field strengths. The point was conclusively resolved by briefly operating the source on helium and noting (as shown in Fig.8) that its location was exactly in accord with the abscissa calibration. It was then postulated that as a consequence of the discharge rather than purely electron impact collisional processes, the triatomic ion H_3^+ is being produced by the reaction

$$H_2^+ + H_2 \longleftrightarrow H_3^+ + H \qquad \text{(thermal)}$$

which is discussed by both Goodyear and von Engel (30) and Varney (31). The onset energy for this reaction is thermal only, and the cross-section is large * on the scale of the primary reaction

$$H_2 + e^- \rightarrow H_2^+ + 2e^- \quad (15.4 \text{ ev})$$

A requirement that there must be a large excess of neutral hydrogen available is certainly satisfied since the degree of source ionization is very low. Strong evidence for this reaction is shown in Fig. 8, in which the dependence of the relative concentrations of H_2^+, H_3^+ is observed as a function of source pressure. The current of H_2^+ rises linearly with pressure while that of H_3^+ rises quadratically as expected. Varney (31) reports that the abundance of H_3^+ exceeds that of H_2^+ when pressures in the source exceed a surprisingly low value, between 10^{-2} and 10^{-1} torr. We observe (Fig.8) that the ratio of peak heights is unity for a source pressure of approximately 3×10^{-2} torr in agreement with Varney. Finally, even though the amount of H^+ to be expected is small, we nevertheless observe none down to current levels four orders below that of H_2^+. It must be concluded that the small quantities of H^+ in the source are highly reactive with considerably larger concentrations of active gas ion species, and that recombination of H atoms into unexcited molecules is highly probable at these pressures, especially at the source walls. The recombination coefficient at a tungsten surface is believed very close to unity (30) so that in addition to recombination at the cathode surface, we can expect the entire anode to be effective since after many hours of operation the source walls are coated with evaporated filament material.

Problems of space charge were referred to in section 2.3.2. and will be briefly discussed. We will calculate the maximum space-charge limited current value for each section of the lens system for N_2^+ ions, according to reference 27, making reasonable estimates of the beam diameters. Consider the extraction tube for ions of 35 eV diverging into the second lens, where the beam occupies approximately a 1 cm diameter disc. The maximum current possible is 2×10^{-7} amperes. The beam is then accelerated to 200 eV and focussed to a diameter of 4 mm by the second lens tube for which the maximum current is about 3×10^{-7} amperes. The beam now enters the spectrometer and by considering the lack of refocussing normal to the plane of curvature, the maximum current beyond the spectrometer exit aperture is estimated to be one-third the incident current, or 1×10^{-7} amperes. This is exactly the maximum current possible in the second 3rd lens tube, in which the beam is decelerated to typically 70 eV. The final lens has a short focal length, but at the minimum working energy of 10 eV the current limit is 2×10^{-8} amperes for the use of half the lens aperture, or approximately 1×10^{-7} amperes for a 30 eV beam. Thus the limitation throughout the system is uniformly about 1×10^{-7} amperes, which from Fig.9 is slightly greater than ten times the limiting current between 20 and 30 eV ion kinetic energy that represents the total current reaching the 4th lens. This means that we are operating at roughly ten percent of the space-charge-limited current at all locations assuming that the beam configuration is optimum, which is unlikely. The most severe limitation occurs in the final lens at low energies, even though the sphere diameter is as small as the desired analyzer resolution permits (sec 3.4.3.). It is interesting to note that the charge column length which minimizes the ion current reaching the sphere (a beam minimum at the target) is twice that which maximizes the target

---

* Saporoschenko J. Chem. Phys 42, 2760, (1965) states that the reaction is exothermic (1.17 eV) and estimates the cross-section to be ~ $50 \times 10^{-16} cm^2$.

current (a beam minimum midway between 4th lens and target), and that the ratio of appropriate ion currents would be 0.25 since the dependence on length is quadratic. This is borne out experimentally, indicating that in performing electron emission experiments, the final lens must be adjusted so as to minimize positive sphere current, i.e. maximize negative current reaching the sphere.

Finally it is worthwhile to suggest possible improvements to the ion beam system. The source would be more efficient for the same gas load if molecular beam techniques were employed to provide a high local density in the region of ion-formation only, and if in addition the ionizing electron beam were magnetically collimated. Vance (20) has used this combination, forming the molecular beam by flowing the gas through an array of parallel channels as treated by Giordmaine and Wang (32). The fringing magnetic fields originating in the getter-ion pumps could possibly be reduced by shielding although this is difficult without reducing the effective pumping speed. If a reduction in beam signal were accepted, the mass resolution of the ion analyzer could be improved by reducing aperture dimensions, with a corresponding increase in the effectiveness of differential pumping. The problems associated with the deterioration of the final beam focus when electron-retarding fields are present in the collector sphere could possibly be somewhat alleviated by placing a saddle field (einzel) lens (26) before the sphere. Some functional coupling could be employed to maintain beam focus during this mode of operation, as used with success by Hagstrum et al (33).

3.4 Interaction Assembly

3.4.1. Target Mounting and Heating

The target used in the experiments is cut from a zone-refined single crystal, has the form of a disc, 6 mm in diameter, and 2 mm thick and is heated by electron bombardment. Three mounting holes have been provided around the periphery, but the experimental requirements dictate the mounting system. The principal concern is that the target must cool rapidly enough that experiments may be performed before an appreciable amount of gas is adsorbed. Immediately after target heating to approximately 2,500°K we know that regardless of the mounting system, the target will cool rapidly by means of radiative heat transfer to the intermediate temperature range at which conduction or diffusion dominate. The time spent in this purely radiative mode is of little concern, since the duration is very short (seconds) and the sticking probability for adsorbable gases is very low at these temperatures. The interval of importance is that following radiative heat transfer, during which it is desirable to cool the target rapidly. A target mount was constructed as shown pictorally in Fig.5. The target is cooled in liquid nitrogen and fitted into a recess at the end of a hollow molybdenum sting, which in turn is attached to a copper block which acts as a heat sink. Holes are drilled through the wall of the molybdenum section to provide power to a heating filament situated directly behind the target disc, and also to present a section of relatively high thermal resistance between target and heat sink. The exact selection of thermal resistances is of great importance, since it is a compromise between required heating power and cooling time, hence careful analysis was performed during design. The thermal inertia of the molybdenum and copper sections is not negligible so that the cooling mechanism is a combination of conduction and diffusion. The analysis was made assuming distinct sections between target and thermal ground and matching conditions at the boundaries. A time-dependent solution is obtained consisting of a summation of eigenfunctions of which only several terms are required to estimate the behaviour at large times, i.e. we are interested in the total time to reach 600°K (τ) for example. The final configuration chosen resulted in a value $\tau \sim 8$ seconds in contrast to a time of 80 seconds assuming purely radiative heat transfer, so that we are able to perform experiments very soon after flashing. The heating filament is a spiral configuration of .015 in. diameter tungsten wire, and is biased negatively at up to 1.5 kV rms by a full-wave bridge capable of delivering 400 ma. In operation the rear surface of the target is bombarded by an electron current of typically 300 ma at 1 kv for a period of about 10 seconds. There is a discrete pressure pulse observable due to the target degassing and further application of heating power merely begins to remove adsorbed gases from the entire target assembly, raising the interaction chamber pressure unnecessarily. The copper base is mounted on a frame using boron nitride spacers and may be moved radially in the vacuum chamber within a tube attached to the experimental flange (Fig.4), by which the entire experimental arrangement may be removed intact. The radial adjustment is used only for the initial beam-target alignment, while external adjusting screws are used to adjust the chamber position by means of a bellows section. Once aligned, the experimental assembly may be withdrawn and replaced without the need for further adjustment.

3.4.2. Surface Diode

In order to monitor the state of adsorption existing at the target, a retarding field diode was constructed using the surface as anode and an adjacently-mounted filament as cathode (Fig.5). The operation of the device is described and illustrated in section 5.3. It is necessary that the electron emission be highly localized so that only changes in the target disc state are observed, and not the entire target assembly. This is achieved by producing a small area of reduced work function at the centre of the wire by means of cataphoretic deposition of thorium, using a procedure described by Hanley (34).

A coating bath consisting of 5 gm of powdered thoria (2000mesh) and 0.075 gm thorium nitrate added to 100 ml. of 95% alcohol was used. The tungsten filament used as the "heater" of the thorium cathode is .005 inches in diameter, and is spot-welded to supports which are also used to attach the target assembly to its supporting frame. The thoria is deposited by placing an anode (Ni) beneath the tungsten wire and adjusting a series resistance so that a deposition current of about 1 ma (approx. 100 ma/cm^2) exists for about 5 seconds. By this method, Hanley (34) reports that the deposition favours smaller particles in the bath, such that the coating is almost entirely made up of particles of diameters between 0.25 and 1 micron. The local thermionic work function is reduced by almost 2 eV(34), (35) so that the ratio of the thoriated cathode emission ($\sim 10\mu$ amperes) to that for pure tungsten is approximately 10^4 at the operating temperature of ~ 1500°K. There is no danger at this temperature of evaporating the thorium, and it is sufficiently high that the cathode temperature at the centre of the filament is determined by a radiation balance with its surroundings. The latter point is important since in the present case it is advantageous to operate the filament in a constant heating-current mode, rather than using the filament resistance as an indicating of cathode temperature for purposes of temperature stabilization during target heating. This is because the time required to reduce the background thermal radiation to a negligible level is shorter than that required to return the temperature distribution along the filament to its previous form. A reduction of the target temperature to 600°K will ensure that the cathode temperature is within 1% of its previous value, whereas a longer time is required (since conduction down the filament and its supports in inefficent) to return the filament end conditions to their former values. There is a possibility that thorium may be deposited into the target face during the heating period, but the rapid desorption at temperatures > 1900°C (35) ensures that the target face is free of thorium after flashing to 2500°K prior to the performance of experiments.

3.4.3. Secondary Electron Energy Analyzer

The objective of the experiment is to obtain the total yield of secondary electrons per incident ion, γ_i, and their distribution function $N_o(E_k)$ for various ion species, kinetic energies and surface conditions. These parameters may be readily obtained by means of a retarding-field analysis of the secondaries, using a spherical retarding-field analyzer (Fig.5) described analytically by Simpson (36). The behaviour of the collector current is observed as a function of its potential and by making reasonable assumptions may be interpreted to derive γ_i and $N_o(E_k)$. There are few measuring devices which do not introduce distortions, and this type of analyzer is no exception. We must consider the distortion from ideality created by the finite size of the electron source (target) relative to the sphere dimensions, the existence of an aperture to permit the entry of the ion beam, the uncertainty concerning the zero-field condition and the second-order effects which are active. The effect of the finite target size most serious at low values of E_k is to recapture some electrons which would ideally escape the target and reach the sphere since the local field acts on the electron's velocity component which is normal to the target surface. The result is that an energy distribution may appear to extend to zero energy, even though theoretically there is a finite lower limit, e.g. in the (He^+-W) system (10). It then becomes difficult to decide whether the experimental distribution indicates some energy-broadening physical mechanism or merely an error of measurement, or both. This "energy aberration" must then be considered a limiting factor of the energy resolution of the analyzer, and is given approximately for a concentric sphere analyzer by (36),

$$\frac{\Delta E}{E} = \left(\frac{a}{b}\right)^2$$

where "a" is the diameter of an inner sphere equivalent to the target assembly, and "b" is the collector sphere diameter. If we approximate the target assembly by 1 cm. diameter sphere, then for the 3 inch diameter collector sphere used $\Delta E/E$ is of the order of .02. The implication is that there is uncertainty concerning the effective potential barrier of about 0.1 volts which must be taken as an inherent distortion factor built into the apparatus.

Due to the existence of contact potentials, the analyzer may not in fact be field-free when the externally applied retarding field potential is zero. A correction may be estimated by observing the retarding field characteristic for electrons thermally ejected from the target, but since the geometry is not ideal, the interpretation is difficult and requires extrapolation (8). The result of this technique did however result in an estimate of the error from this source that is comparable to the uncertainty in the effective potential barrier, so that no correction was considered justified. The aperture required for ion beam entry is of the same diameter (8 mm) as the preceding lens aperture, so that if the sphere interior is field-free, the fraction f_a of electrons that will not be collected from this cause is at most 0.5% assuming an isotropic spatial distribution of secondary electrons. For the sphere slightly positive, as when measuring the total yield γ_i, this fraction will be somewhat less, but is considered negligible under all conditions in the analysis following. The emission of electrons (tertiaries) from the collector due to the impact of the low-energy secondary electrons produced at the target is small and will also be neglected. We shall now consider the remaining space currents that exist within the sphere and the method by which the required data may be deduced from their behaviour. There are three reasonably distinct regions of operation of the analyzer. Firstly for the sphere potential V_s sufficiently positive, the secondary electron current is completely collected and reflected ions, if any, are repelled. Secondly, for the sphere biased strongly negative, the secondary electron current is completely suppressed and the collector current will be equal to the reflected ion current, if any. Thirdly, for sphere potentials between these limits, the electron current will be partially suppressed; we shall analyze this region, since it yields the assymptotic behaviour by considering the appropriate limits. At a particular value of negative sphere potential V_s (target at ground) a fraction f_k of the emitted electron current $\gamma_i I_i$, having energies in excess of $(-V_s)$, will surmount the potential barrier according to the distribution function $N_o(E_k)$, viz.

$$
\begin{aligned}
f_k(V_s) &= 1 - \int_0^{-V_s} N_o(E_k)\,dE_k & V_s &< 0 \\
&= 1 & V_s &\geq 0
\end{aligned}
$$

Of these, a fraction f_a may exit through the sphere aperture. A fraction R of the incident ion beam may reflect as ions, so that a positive current RI_i can reach the sphere in this potential region. The net currents reaching the sphere and target are thus, respectively

$$I_s = -(1-f_a)\,f_k\,(\gamma_i I_i) + RI_i$$

and

$$I_T = I_i + f_k\,(\gamma_i I_i) - RI_i$$

The sum of these two currents is

$$(I_s + I_T) = I_i\,(1 + f_a f_k \gamma_i)$$

and is very nearly the true incident ion current I_i since $f_a f_k \gamma_i$ is of the order of 10^{-3} or less. Keeping in mind that f_k is a function of V_s, the non-dimensional current ratio ρ is given by

$$\rho = -\frac{I_s}{I_T + I_s} = (1 - f_a)\, f_k\, \gamma_i - R$$

$$\simeq f_k \gamma_i - R \qquad f_a << 1$$

For V_s sufficiently positive, the ion reflection term (if it exists) will reduce to zero, so that putting $f_k = 1$

$$\rho_+ = \gamma_i$$

while for V_s strongly negative $f_k \to 0$, and

$$| \rho_- | = R$$

Between these limits, the derivative of ρ with respect to V_s will be proportional to the distribution function $N_O(E_k)$ provided $\frac{dR}{dV_s}$ is small as is certainly the case for negative V_s, viz.

$$\frac{d\rho}{dV_s} \simeq \gamma_i \frac{df_k}{dV_s} = \gamma_i N_o (E_k)$$

Finally,

$$N_o(E_k) = \frac{1}{\gamma_i} \left(\frac{d\rho}{dV_s} \right) = \frac{1}{\rho_+} \left(\frac{d\rho}{dV_s} \right)$$

Experimentally, we arrange that V_s vary linearly with time, so that

$$N_o(E_k) \ \alpha \ \frac{d\rho}{dt} \qquad V_s \leq 0$$

Unfortunately, in the present experiment we cannot distinguish between stray primary ions reaching the sphere and ions reflected at the target. It is felt that the small positive current observed at large negative values of V_s is due to inadequate 4th lens focus under these conditions, rather than indicating a reflection coefficient $R \sim 10^{-3}$. In order to minimize errors in measuring I_s due to resistive leakage, the sphere is mounted on a guard ring of nearly identical potential (Fig.5) so that the voltage drop across the insulators (boron nitride) is of the order of millivolts only. In addition, the sphere is enclosed by a cylindrical guard ring to reduce spurious currents due to the getter-ion pump operation and the effects of capacitance (sec. 4.1.1). In conclusion, it is obvious that it is a far simpler matter to obtain only the total secondary electron yield γ_i, since the effects to be considered in order to obtain accurate energy distributions are numerous, and require specialized techniques, to be described in section 3.

4. INSTRUMENTATION

4.1. Measurement of Electron-Current Characteristics

4.1.1. Guarding Techniques

In section 3.4.3, the real space currents within the energy analyzer were discussed, but there are additional virtual (displacement) currents which exist by virtue of parasitic resistive and capacitive elements in the device shown schematically in Fig. 10. These problems may be alleviated considerably if the electron collector remains at a fixed potential, and the target potential is varied to provide a retarding field analysis. In such a case, the entire set of lens and source potentials must be referenced to the target to maintain constant ion kinetic energy (30). This solution is only partially satisfactory since there is still a significant remnant effect which can be resolved by a method (to be described) that may be applied to a system in which the sphere potential is variable, and the target level fixed, yet still reduce the spurious signals to the same level. The electron currents to be measured have a range of magnitudes of the order 10^{-12} to 10^{-10} amperes, while we wish to vary the sphere potential by ± 10 volts within a time compatible with clean surface experiments, i.e. within a ten second period. The amplitude of the potential variation places a stringent requirement on most insulators, and in the present case, we are limited to bakeable materials such as alumina and boron nitride which in a compact geometry have resistance values of perhaps 10^{14} ohms. For an impressed voltage of 10 volts, the leakage current would be 10^{-13} amperes or 10% of the minimum level stated above. This conditions would be intolerable since it would require extensive corrections to obtained data and would hinder the implementation of high-speed analog techniques. The solution is simple, however, since the voltage stress across the insulators may be reduced to a negligible level by mounting the assembly on a guard ring at collector potential. In practice, the voltage stress can be reduced to the millovolt level imposed by the measuring instrument, which is a negative feedback device of high loop gain.

The rate of change of the collector potential will result in further spurious currents unless compensation is provided, according to

$$i = C\left(\frac{dV_s}{dt}\right)$$

Suppose that $dV_s/_{dt}$ is 1 volt/second, then a stray capacitance of 10 pf will contribute a error of 10^{-11} amperes. While it is true that since we apply a linear voltage time waveform the current should represent a constant offset, its magnitude is so large that a severe common-mode rejection situation would result. The capacitances of interest are the target-to-sphere capacitance C_s, and the sphere-to-ground capacitance C_g. The former has a value of approximately 2 pf (obtained by applying a linear waveform), and the latter may be as high as 200 pf. Since these values represent a geometric configuration we cannot remove them, but merely transfer them in the circuit, or provide compensations. The sphere-to-ground capacitance C_g consists of components due to the target assembly geometry and shielded conductors both internal and external to the vacuum system. The component due to cables can be minimized by locating the electrometer favourably and can be transferred to the input of the measuring instrument by floating the outer conductor at nominal collector potential (instrument ground) making sure that this additional capacitance will not be overly detrimental to the intrument response speed. The component due to the collector geometry may be partially transferred in this manner by surrounding the collector with a surface also at nominal collector potential. This cylindrical guard ring is also used as a mounting surface for the collector insulators as previously described. There remains about 20 pf between the sphere and the target assembly mounting frame as well as the sphere-to-target capacitance of 2 pf, which is present regardless of whether the sphere or target is fixed in potential. Our problem now is essentially how to apply a time-dependent waveform to a capacitor (which of necessity requires a current waveform) without passing the charging and discharging current through a DC ammeter attached to one plate of this capacitor. The solution (Fig.10) is that we may apply this waveform by capacitive coupling rather than direct DC coupling and furthermore if the electrometer is placed across the resulting capacitance bridge, a nulling of the bridge is possible when the ratios of capacitance and resistance are correct.

This method of bridge balancing (S - NULL) permits collector potential variations of 1 volt/second with resultant spurious current as low as 10^{-14} amperes, and is achieved by adjustment of the variable capacitance at three levels until the value (C_s+C_g) is reached; (the resistive arms are equal). The choice of the resistance ratio and the impedance level is dictated by the amplitude of voltage sweep available (since we divide it) and by a compromise between waveform distortion due to finite voltage source impedance and noise generated by finite electrometer-ground impedance. A similar solution allows nulling of the spurious target current due to C_s. For this case we again form a bridge network, but since the capacitance is already low, we prefer to adjust the resistive ratio. In addition, the waveform applied to the bridge must be inverted, and this operation is ideally performed by an operational amplifier inverter (6) of variable gain, (T-NULL).

4.1.2. Calibration

The electrometers used to measure the I_s and I_T currents contain high-valued resistors that are typically subject to a tolerance of ± 3%. In order to improve the accuracy of measurement, two calibration circuits were constructed (Fig.12), which permit compensation in the analog circuitry following. Circuit A provides I_s and I_T currents of a known ratio (γ_i= .0373) of value expected in the experiment. The current ratio is established by a voltage divider consisting of low temperature coefficient metal film resistors driving a matched pair of 10^{11} ohm resistors. The divider ratio was measured using a differential voltmeter of high precision (digital nulling type) so that once obtained, the current ratio is independent of the battery voltage. Implicit in the calibration is the assumption that the loop gain is such that the electrometer input is virtually at ground potential. Circuit B requires the same assumption to provide a test for the denominator scaling, and establishes a condition I_s=I_T such that I_i= 0.

4.2 Analog Techniques to Obtain Normalized Energy Distribution Functions

The philosophy followed in developing this portion of the instrumentation is that it is extremely desirable to perform all data-reduction operations simultaneously with the data gathering. Furthermore, in order to directly compare the changes in distribution function resulting from a change in a physical parameter (ion energy, surface work function, etc), the output data must be normalized to the ion beam current I_i. There are two approaches to this problem. One is to maintain constant beam current under all conditions by a feedback stabilizing system as used by Hagstrum (33), the other is to accept variations in I_i, but perform operations on the normalized current ratio ρ . There are disadvantages to either system, but it is felt that the technique to be described is the best to date.

In the constant ion current system, a signal proportional to the true beam current I_i is used to control the ionizing electron current in the source and hence vary I_i. There is a limitation on the degree to which the ion current flucuations may be reduced without oscillation occuring due to excessive closed loop gain. Hagstrum (33) reports that the variations in I_i during a sweep of collector potential are no greater than 0.2% by this method. A limitation however, is that if one wishes to compare distributions for conditions resulting in a wide ion current spread, a current level attainable by the most detrimental case must be used throughout, with the result that the quality of the data is not maximized in every case.

In the other method of operation (normalizing with respect to a variable ion current) there is a difficulty in devising a fast, accurate analog divider to obtain the non-dimensional electron current ρ. Propst and Lüscher (37) describe a system of self-balancing servo loops which is neither flexible nor fast, requiring sweep times of 100 seconds and servo-motors of high performance. Analog division is performed in the present experiment by means of a digital voltmeter (sec 4.3) with high precision and sampling rates, that was constructed in this laboratory because the unique combination of desired specifications was not commercially available. By this means, we obtain a numerical readout of the current ratio ρ (and hence γ_i) as well as its voltage analog within 0.1%, in conjunction with a sampling rate that permits the entire distribution function to be obtained during a 10 second interval. This time interval permits the observation of clean-surface experiments in the presence of adsorbable gases without resorting to exotic vacuum techniques. With these points considered, the analog computation (Fig.10) may be described.

The electrometer used to measure the I_s current is a Keithley model 600A which is battery operated and may be connected as a feedback amplifier when measuring small currents (FAST mode). The output impedance is relatively high, however, (17kΩ), and in the feedback mode, neither output terminal is connected to instrument ground. Our first task is to eliminate the common mode voltage at the output terminals which is most suitably performed by the configuration shown, employing three operational amplifiers. Each output terminal is attached to a voltage follower with gain to ease the common rejection requirements and to provide an impedance level compatible with the 600A output level. The differential gain is nominally 10 and the conversion to a single-ended signal is performed using an add-subtract circuit of nominally unity gain. Common mode rejection is established by applying V_s to the electrometer ground while the input is open-circuited, and adjusting the feedback resistance (CMR) of the unity gain amplifier until the output is zero, provided the amplifiers having initially no offsets. Numerator scaling is provided by adjustment of either of the follower feedback resistances. The output from the I_T electrometer (Cary Model 31) is already single-ended, and may be correctly scaled by a simple inverting amplifier of nominal gain 100. A correction to obtain the true ion current (I_s+I_T) is provided by adding the correct fraction of the I_s analog at the summing point. The denominator scaling is established by using calibration circuit B (Fig.12) which provides the condition $I_s = - I_T$ or $I_i = 0$ and requires that the output of amplifier 4 be nulled. The numerator scaling is then adjusted using calibration circuit A, such that the ratio of numerator and denominator is correct as read by the digital voltmeter/ratiometer following. The ratiometer provides an analog output of 8 volts full scale, which is time differentiated using amplifier 5. The combination of input and feedback elements is such that at low frequencies the amplifier may be considered a differentiator, while at high frequencies it is an integrator, effectively filtering noise. Careful consideration must be given to the selection of component values so that waveform distortion is acceptable, and the procedure is described in Ref. 38, for example.

The "frequency of transition" from integrator to differentiator must be set so that the phase shift (which is equivalent in plotting $N_o(E_k)$ distributions to a voltage error) and the amplitude error are small. The former condition is less easily satisfied than the latter, so that the best procedure is to adjust components while actually plotting distribution functions, until a compromise is made between remaining noise levels and phase shift errors.

The six operational amplifiers used are Philbrick type EP85AU, and are conveniently utilized in a Philbrick model RP Operational Manifold (Fig. 12) which permits extremely flexible use. The linear sweep is provided by a Wavetek model 104 Sweep Generator of excellent linearity; its waveform and corresponding time derivative using the differentiator (5) are shown in Fig.13.

4.3 Ratiometer

The function of the ratiometer is to provide an analog voltage output proportional to the ratio of two input voltages and to provide a visual digital indication of the actual value. The instrument constructed, however, is capable of not only this function but may also be used as a conventional Digital Voltmeter, or a time-interval counter of four-digit precision. A view of the instrument is shown in Fig. 14, and circuit diagrams are given in Figs. 15 to 20 inclusive. It is this instrument which enables the collection of experimental data in a meaningful (normalized) form, and has numerous applications of a similar nature in any laboratory.

The most modern design techniques have been employed in its construction and every effort has been taken to permit complete flexibility of operation, including polarity readout for all numerator and denominator polarity combinations, floating decimal point, complete symmetry with respect to inputs, 60% overrange and provision for the measurement of time intervals in two ranges up to 16 milliseconds or 1600 seconds. Each input channel is provided with three voltage ranges, 1, 10, 100 volts, with input impedance of 160 K. Measurements are made at a rate depending on the input level, typically 60 per second, to an accuracy of ± 0.01% of full scale.

Extensive use has been made of now-standard monolithic integrated circuits, both digital and linear, and copper-clad circuit boards as shown in Fig. 14. The digital IC's, approximately 80 in number, are all of the Motorola MC 700P series (plastic case, R.T.L.) and are primarily multifunction types. Of the 10 linear IC's used in the device, two are comparators (Fairchild μA710C), and the remainder are operational amplifiers (Motorola 1433 and 1533). Approximately 500 discrete components are also incorporated in the design.

The required specification indicated that a design extension of a prototype instrument described in Ref. 39 would be suitable. The input voltage ratios are converted into pulse-width signals by the up-down integration technique which permits accuracy independent of variations in the integration time constant occuring outside the short measuring period. The pulse width is then recorded by the four-decade counter portion of the instrument and displayed numerically. The numerical value is converted while still in Binary Coded Decimal (BCD) form to an analog output by a Digital-to-Analog converter which operates on the principle of current steering. A brief description of the detailed operations is given in Appendix B.

5. SURFACE PREPARATION AND CHARACTERIZATION

5.1 Surface Preparation

The target button used is 6 mm in diameter and 2 mm thick, being cut by spark erosion from an epitaxially grown zone-refined single crystal. The resulting blank is flat to within microinches, but the depth of surface damage is considerable. The mechanical polishing process is a progressively finer series of abrasive operations, each of which is an attempt to remove the strain damage introduced by the previous stage, ultimately leading to a smooth, strain-free surface. The initial coarse polishing was performed using water-lubricated graded carborundum papers. After grinding in a single direction only, the surface was washed thoroughly in water and alcohol and examined under an optical microscope, continuing the polishing stage only until all coarser scratches from the previous stage were erased. The specimen was then rotated by 90 degrees and polished using a finer paper, as far as the 4/0 grade. Using varsol as a lubricant, the polishing procedure then entered a second phase in which diamond paste (6 micron down to 1 micron) was progressively used on a cloth-covered rotating disc.

The final polishing agent was .05 micron aluminum oxide powder mixed with diluted alcohol. The resulting speciment surface is highly-reflective and only minor scratches are discernable under the microscope at 1000X magnification.

To reconstitute the surface layer by removing mechanically-introduced strain damage, the target buttons are vacuum annealed at 2000°C. As in the experimental program, target heating is achieved by electron bombardment of the rear surface for brief periods (30 seconds or less) until annealing times approaching ten minutes are reached.

5.2 Characterization of Physical Properties

5.2.1. Laue Back Reflection Studies

In order to verify that the tungsten surface used is truly the (100) face, and that it is free of faceting and excessive mechanical strain, X-ray diffraction photographs were taken both before and after high temperature flashing. The Laue back-reflection method was chosen because of its simplicity and accuracy. In this technique, a beam of white radiation produced by an unfiltered X-ray source (copper, 20 kV) is allowed to fall on a fixed single crystal such that diffracted beams are recorded by a film placed between the source and crystal, (Fig.21). Diffraction is governed by the Bragg law $\lambda = d\sin\theta$, such that at fixed θ each set of planes in the crystal diffracts the appropriate wavelength satisfying the relationship. A cone of reflected rays is formed for each zone of planes in the crystal(Fig.21), and each cone intersects the film along a hyperbola.

It may be seen that the Laue spots for given zones will lie on such hyperbolae, so that the identification of diffraction spots is greatly simplified if attention is directed mainly at those spots which lie at the intersection of several densely populated hyperbolae. The interpretation of the photograph maybe readily carried out by using a Greninger chart and stereographic (Wulff) net to perform a co-ordinate transformation from film plane to stereographic projection. The hyperbolae thus transforms to great circles. The poles may then be readily identified by comparison with a standard stereographic projection of the crystal (44, 45). Fig. 22 is a print obtained from the X-ray film, which is reproduced as a line drawing in Fig. 23. The major poles are shown as dark circles and are shown after co-ordinate transformation in the lower drawing, which is a simplified standard (100) projection. The primary (100) pole is displaced approximately 3 degrees from the film centre possibly due to misalignment of the (100) plane with the surface plane, but more likely due to misalignment of the specimen with respect to incident X-rays and the film plane. Subsequent diffraction patterns show this to be the case, and that the (100) plane is coincident with the surface within 1 degree. The shape of the back-reflection spots is indicative of lattice distortions due to mechanical polishing, although the interpretation is not quantitative. The short arcs seen to pass through some Laue spots are portions of Debye rings observed for polycrystalline materials. The orientation of plane normals in this case is not completely randomized, but restricted, so that only a portion of the complete ring appears. Although no systematic observations were performed, it was seen that the diffraction spots become more ideal after extensive flashing, indicating an improvement in structure following annealing.

The (100) face was chosen for these experiments because of its stability during thermal cycles, and has been found to be so throughout the present experiments, by obtaining Laue patterns before and after the experimental interval. This point was of only minor concern, since the observed faceting of (100) tungsten to type (110) occurs in conjunction with high oxygen adsorption (46), which was not the case here.

5.2.2. Electron Micrographs

The use of electron transmission microscopy enables indirect observation of the surface topography at magnification levels up to 150,000 or greater. Such observations could be ambiguous without progressive optical magnification, since the sampled location is correspondingly smaller in area. The replication of the crystal surface and the electron micrographs were performed by the Ontario Research Foundation, using a JEM 200 facility. The replicating technique is necessary since the target cannot be made sufficiently thin, nor can it be destroyed. A cellulose nitrate solution (Parlodion) is deposited on the surface and permitted to dry. Several coatings may be necessary to provide sufficient film strength for removal. The resulting surface imprint may in some cases be directly used for transmission studies, although the resolution is limited and there is a danger of polymerization at high beam intensities. It is therefore preferable that a carbon replica be subsequently made by vacuum deposition, followed by the dissolving of the parlodion film. If quantitative estimates of surface irregularities are required, the carbon replica may be vacuum coated with germanium evaporated at an oblique source. The resulting shadowing may be used to determine structure dimensions if the angle of deposition is known. In the present case a 45 degree germanium deposition provides "out-of-plane" scaling equal to that of the surface plane. The result of this technique is shown in Fig.24, and represents the only salient feature observed on the (100) tungsten face, after complete polishing and annealing. The dark line running diagonally across the photograph is a step of at most 50A in height, and is commonly the result of a surface fault produced by the annealing process. By this method the crystal conforms to the physical contour mechanically imposed, while maintaining a single exposed crystalline plane. Micrographs taken elsewhere on the replica were essentially featureless, resembling the background of Fig.24. There is no evidence, however, of the severe damage resulting from the spark erosion cutting process. The illustrated surface quality obtained by purely mechanical polishing techniques is vastly superior, however, to similar suraces which had undergone electropolishing processes in this laboratory.

There is additional evidence that the surface uniformity is improved following high temperature annealing such that scratches remaining after the final stage of mechanical polishing may be partially erased. The mobility of tungsten atoms at the temperatures used (~ 2000°C) is not as great as for materials of lower melting point, so that the gain in surface quality by this process is not extreme.

A similar target used by O'Keefe (43) was subjected to high energy electron diffraction analysis which revealed no evidence of microfaceting to orientations other than (100) nor evidence of carbon contamination.

5.3 Characterization of Surface Contamination - RFD

5.3.1. Theory of the Retarding Field Diode

The construction of the surface diode has already been described in section 2.4.2, together with a discussion of the consideration concerning temperature stabilization. We shall now consider the operation and interpretation of the technique. An example of the full current-voltage characteristic for constant cathode (filament) temperature T_c is shown in Fig.25. At low or negative values of applied cathode-to-anode potential, V_a, the anode current i_a reflects the Fermi-Dirac energy distribution of thermally liberated electrons since only those having sufficient energy to overcome the cathode-to-anode potential barrier will reach the anode. There will then be a potential region in which the anode current is limited by space-charge effects, and finally a departure from this curve due to finite cathode emission. The saturation (emission-limited) region is not constant in current, but nearly linear due to an effective reduction in cathode work function ϕ_c caused by strong local fields (Schottky effect). The actual value of the potential change experienced by ejected electrons depends on the instantaneous value of the anode and cathode work functions ϕ_a and ϕ_c i.e. $(V_a + \phi_c - \phi_a)$, so that the retarding field region in Fig.25 appears to extend to positive values of the diode voltage. This is the so-called "Contact potential" effect, so that the true zero-field point lies somewhat to the right of the indicated origin by an amount $(\phi_a - \phi_c)$. This amount can be estimated from Ref. 31, 32 to be between 2 and 2.5 volts since we have purposely reduced the cathode work functions by thoriation to provide localized emission. The point is academic, since as shown below, by operating in the retarding field region, we are interested only in the change in diode voltage and not the precise value. As a consequence, the retarding field technique is capable of yielding information on the changes in work function of the anode, but not on the absolute value (40). By combining the Fermi-Dirac distribution function with Richardson's equation an expression for the anode current i_a may be written for the retarding field region for an ideal planar diode:

$$i_a = AT_c^2 \ \exp\left\{ - \frac{e(\phi_a - V_a)}{kT_c} \right\}$$

where T_c is the target temperature, A is a constant, k is Boltzmann's constant, and i_a, ϕ_a, V_a have been previously defined. If i_a is maintained constant, and T_c is also fixed, then we may observe changes in ϕ_a by measuring instantaneously the anode-to-cathode potential V_a, as shown in Fig.26. The anode current is maintained by a nearly-ideal current source, while the cathode temperature is fixed by a constant-current filament-heating supply. The anode potential is measured with respect to the filament centre(cathode) by an electrometer of high input impedance, or alternately we may impress a variable anode-to-cathode voltage to obtain the entire $(i_a - V_a)$ characteristic as in Fig.25. There are conditions to establish, however, to ensure that the current source is adequately decoupled from variations in diode voltage. The circuit of Fig.26 contains an external current source consisting of a battery of voltage V_b and series resistance $R(10^8\Omega)$ so that the diode current is given by $i_a = (V_b - V_a)/R$.

We expect changes in V_a of the order 0.5 volts, so that if $V_b = 45$ volts, i_a will of necessity vary by perhaps 1%. However, this is not serious if the series resistance R is sufficiently larger than the incremental resistance at the operating point on the diode characteristic, i.e. the current source is sufficiently "stiff". By differentiating the anode current expression, we obtain for the circuit of Fig.26,

$$\left(\frac{\partial V_a}{\partial \phi_a} \right)_{T_c} = \left\{ 1 + \frac{k\,T_c}{e\,(V_b - V_a)} \right\}^{-1}$$

If $kT_c \ll e\,(V_b - V_a)$, as is certainly true for $T_c \sim 1500^{\circ}K$ and $V_b = 45$ volts, then $\Delta\phi_a = \Delta V_a$ to better than 0.5%. It is important to note that the cathode work function (or total possible emission current) does not need to be held constant for this relationship to be valid. This is fortunate, because the dependence of ϕ_c on the adsorbed thorium coverage and structure is pronounced (35). The above relationships have been derived for an ideal planar diode, however, provided that i_a is a function of $(\phi_a - V_a)$, we may make similar comments.

The condition is slightly more stringent, however, in that we must assume i_a= constant, whereas in the ideal diode this condition was unnecessary provided $kT_c \ll e(V_b - V_a)$. In practice, the anode is allowed to float in potential in order to maintain the impressed constant current, and the variation of V_a(or ϕ_a) is plotted against time. This is simpler than plotting the entire characteristic family as in Fig.27, since in the retarding field region, the curves are parallel and any current level will reflect the same potential shifts. The curves of Fig.27 are taken at equal time increments, although the trace time prevents the plotting of a clean-surface characteristic. This problem is not encountered by operating at a single current level (4.5×10^{-7} amperes) as shown, so that the time variation in ϕ_a may be plotted immediately after flashing the target (anode), as in Figs.28, 29. A brief cooling period is required, however, since the anode is heated sufficiently to become a current source, driving the anode potential to large positive values. The origin of the latter curves is the time at which target heating ceased, so that a potential minimum is produced approximately 5 seconds after flashing, indicating the clean-surface condition.

5.3.2. Adsorption Experiments

A number of auxiliary experiments were performed to determine the surface state during the experimental intervals, using the retarding-field diode technique already described. By this method, the degree of surface coverage (and species) may be determined by a correlation with the change in surface potential (or work function). The direction of potential change is determined by the relative importance of the various binding forces (7), but in most cases an adsorbed monolayer results in a surface work function increase of between 0.2 and 1 volt. There have been a number of highly-pertinent LEED experiments recently performed which enable the present surface diode experiments to indicate quantitative results.

Estrup and Anderson (41) have investigated the adsorption of hydrogen molecules at a (100) tungsten surface, and correlate work function and surface coverage, while Madey and Yates (42) describe the other gas of interest, nitrogen. The primary motive is not to investigate the adsorption process in detail, but rather to be certain that the gas species and degree of coverage is established for every electron energy distribution function obtained. A series of experiments were performed both with and without the beam in operation, in which the target was flashed to a high temperature (approx. 2300°K) and the time variation of work function observed (Figs. 28, 29). The curves are highly repeatable, each returning to an assymptotic level characteristic of the equilibrium state, and in addition the magnitude of the work function changes is consistent, with the minima coincident at times near zero. This is interpreted as meaning that the flashing temperature is sufficiently high that a clean state is consistently reached even though the exact temperature value is not precisely known.

The curves are plotted against time rather than the more usual (torr-sec) since the pressure fluctuation is not recorded. This is of no importance since we have obtained the traces at the given experimental pressure levels, and we are merely concerned with identifying a distribution taken a given time after flashing with the corresponding surface coverage. It may be seen that the curves obtained with or without gas admitted to the ion source are similar in shape and magnitude of the change $\Delta \phi$, regardless of whether the source gas is nitrogen or hydrogen. This implies that the background gas component is constant regardless of the source gas, although its pressure level is dependent on its operation, and that with little doubt this adsorbing gas is hydrogen.

It is well-established that hydrogen is the principal remnant gas species in metal bakeable high vacuum systems, being evolved from within the chamber material itself. Furthermore, hydrogen is re-evolved from the getter-ion pump used, when gases such as nitrogen are admitted to the chamber. This phenomenon has been observed in this laboratory by O'Keefe (43) as an instantaneous rise in the hydrogen level as determined by a partial pressure analyzer monitoring the hydrogen peak. The foreign gas is either removed by the ion pump itself or effectively pumped by displacing adsorbed hydrogen molecules at internal surfaces of the chamber. The magnitude of the change in surface work function ($\Delta\phi \simeq + 0.8$ volts) is also in good agreement with that observed for hydrogen adsorption in Ref. 41 and is larger than any other surface orientation or gas combinations.

The initial sticking probability is high, and from the quasi-linear portion of the trace can be estimated to be about 0.67, in comparison with that estimated by Estrup and Anderson (41) of 0.65.

The change in surface potential is almost linear with surface coverage, so that the adsorption traces also represent the variation of σ with time after flashing. The initial adsorption as we have seen occurs with high sticking probability, S, and is accompanied by dissociation of the molecules, such that an ordered array of 5×10^{14} adatoms/cm^2 is produced. (The tungsten substrate has 10×10^{14} atoms/cm^2 arranged in a square array.). The subsequent filling of the remaining adsorption sites to a level 10×10^{14} adatoms/cm^2 is far from random in that hydrogen atoms migrate across the surface producing characteristic superstructures of adatoms in a highly controlled manner. These observed phenomena are difficult to explain using present theory, since it implies that neighbouring adatoms interact over large distances (30A or more). The sign of the surface potential change (negative) indicates that the adatoms possess a net negative charge, and the magnitude indicates that extensive redistribution of charge occurs in the surface layer. (It is approximately twice the change for hydrogen adsorption on (110) tungsten).

It has been observed that after prolonged operation of the ion beam (6 hours or more) using nitrogen as the source gas, the nitrogen background pressure will rise to the point of becoming apparent in the surface potential measurements. The surface work function is then observed to initially decrease with time (β_2 - nitrogen adsorption) in agreement with the findings of Madey and Yates (42), while at later times the work function increases again due to β_1 -nitrogen adsorption. It appears that the more stable β_2 -state ($\Delta\phi$=0.2 volts) is populated before the β_1 -state($\Delta\phi = + 0.5$ volts) begins to fill, until the fractional coverage is about 20%, at which time both states appear to fill at the same rate. The surface temperature is also highly important in that at temperatures of approximately 650°K, well below the onset of desorption (1100°K), the mobility of β_1 -nitrogen enables its conversion to the more stable β_2 -form so that immediately after flashing in a nitrogen background, we would expect the adsorbate to be the β_2 -form (negative work function change).

This behaviour after prolonged beam operation is temporary, since by removing the nitrogen source the background gas returns to its equilibrium composition; hydrogen is constantly evolved in the vacuum system, whereas the source of nitrogen is limited. These effects of nitrogen adsorption at the target are not observed when the background pressure is predominantly hydrogen, and N_2^+ is the incident ion; because the nitrogen flux levels are low. Although the total flux of nitrogen molecules entering the interaction chamber from the spectrometer section (2×10^{-7} torr) is of the order 4×10^{13} per second, only a small fraction (approximately 2×10^{9} per second) can reach the target without collisions with the hydrogen-covered inner surfaces. Even assuming a sticking probability of unity, the time for nitrogen monolayer adsorption is of the order 10^{4} seconds for this group which strike the target directly. It is believed that the bulk of the nitrogen molecules are pumped by chamber surfaces or efficiently pumped by the getter-ion pump. The second group of nitrogen molecules is that composing the ion beam itself. The molecular flux levels at the target are as high at 10^{11} per cm^2-sec, but the beam kinetic energy is so great relative to the well depth of about 2 volts that the sticking probability is considerably lower than unity. O'Keefe (43) estimates the sticking probability for 0.18eV nitrogen molecules at a clean (100) tungsten surface to be 10^{-3}, believed the only measurement made above thermal energies. The probability at the present incident energies of 15 eV to 30 eV is expected to be substantially less than even this value. The time constant for adsorption is thus increased to many times the value 2000 seconds arrived at by assuming complete trapping. The time of importance is thus that for adsorption of the hydrogen background, which is approximately 150 seconds assuming unity sticking probability,S. In reality, the slopes of the adsorption traces of Figs. 28, 29 indicate that $S \simeq 0.7$ at low coverage decreasing to 0.01 or less at high coverage, so that after the above time the adsorption is only 50% complete. The experimental data on clean tungsten reported in the next section is obtained within 15 seconds of target flashing, so that the "clean" state represents 5% hydrogen coverage or less.

5. 3. 3. Influence of Ion Beam

In the previous section it was argued that the adsorption of beam molecules on impact is unlikely since their kinetic energy is large. There is evidence, moreover, that the beam may actually reduce the net number of adatoms (most of which come from the background gas) by virtue of this energy. In Fig. 28 we show three curves for operation with a nitrogen source, two representing conditions under which the beam strikes the target at 30 and 15 eV kinetic energy respectively, and a third for which the mass analyzer is used to prevent N_2^+ impact while the source and background gas loads remain. The time constants characteristic of hydrogen adsorption are seen to decrease in the above sequence, indicating not only that the ion beam is capable of "scrubbing" the surface, but that the process is energy-dependent as expected. It is possible to make inferences from these curves, by considering the change in slope,with regards to the overall effective sticking probability resulting from ionic impact.

Suppose $D_{15}(\sigma)$ and $D_{30}(\sigma)$ represent the number of hydrogen atoms desorbed at coverage σ per cm^2. per incident ion of kinetic energy 15 and 30 eV respectively, i.e. a "desorption coefficient". This coefficient is actually a product of the probability of ion-atom collision and the probability of desorption given such a collision. In this high-energy regime in which the ion energy is significantly greater than those energies characteristic of the adsorbed surface layer, we would expect a hard-sphere interaction dependent on the ion momentum, so that D_{30} and D_{15} might be in the ratio $\sqrt{2}$:1 if the ion-atom collision cross-section is not energy-dependent. Thus,

$$\sigma(t) = G_b \int_0^t S(\sigma)\, d\sigma - G_i \int_0^t D(\sigma)\, d\sigma$$

where G_b and G_i are the background and ion fluxes (per cm^2-sec) respectively, and $\sigma(t)$ is the coverage at time t. The time-derivative is the slope in Figs. 28, 29, viz

$$\frac{d\sigma}{dt} = G_b S(\sigma) - G_i D(\sigma) = G_b S'(\sigma)$$

where S' is an effective sticking probability equal to the true background probability S only in the absence of the ion beam, viz.

$$S'(\sigma) = S(\sigma) - \frac{G_i}{G_b} D(\sigma)$$

This decrease in effective sticking probability is shown in Table 1, for 25, 50 and 75 percent hydrogen coverage. The case for no beam has already been partially described; the sticking probability decreases from 0.67 at 25% coverage to less than 0.1 at 75% coverage. The effect of ion impact is to reduce these values by more than ten percent, even though the neutral-ion flux ratio is 60. The desorption coefficients D_{30} and D_{15} may then be calculated without actually knowing the background flux, but only the ion flux (almost exactly 10^{11} per cm^2-sec). By taking the ratio of these coefficients at the same value of σ, the common ion-neutral collision probability is cancelled so that we obtain an estimate of the dependence on kinetic energy. It is seen in Table 1 that although the absolute values of the desorption coefficients vary widely, the ratios at a given σ are all very nearly $\sqrt{2}$:1. It should be pointed out that these ratios entirely remove any dependence on estimated flux levels, so that the result may be considered significant, viz

$$\frac{D_{30}}{D_{15}} = \frac{\dot{\sigma}_o - \dot{\sigma}_{30}}{\dot{\sigma}_o - \dot{\sigma}_{15}} \approx \sqrt{2}$$

where $\dot{\sigma}_o$ is the time derivative of hydrogen coverage in the absence of ion impact, and $\dot{\sigma}_{30}, \dot{\sigma}_{15}$ that for the impact of 30 and 15 eV N_2^+ ions respectively, as obtained from Fig. 28. The absolute values of the desorption coefficients appear to possess a minimum, however, at approximately half-coverage.

We may conjecture that at low-coverage, the adatoms are highly mobile and loosely-bound and more easily desorbed by ion impact than at half-coverage when the relatively stable 2 x 2 structure (41) is complete. The adsorbate at higher coverage includes large superstructure formations again less strongly bound to the surface, so that qualitatively we would expect a minimum in desorption efficiency with increasing adatom density.

It was not possible to discern any effect of ion beam desorption using H_2^+ (Fig.29) partly because the ion flux is lower by a factor of two, but primarily because the momentum of an H_2 molecule is a factor $\sqrt{14}$ less than that of a nitrogen molecule. The total desorption rate would thus be expected to be about one order less in magnitude, and indistinguishable from routine experimental fluctuations in the (σ-t) traces.

6. EXPERIMENTAL STUDY OF AUGER NEUTRALIZATION

6.1 At a (100) Tungsten Surface

6.1.1. The Nitrogen Ion Species N_2^+, N^+

The energy distribution of electrons ejected from a clean (100) tungsten surface by N_2^+ ions of 15 eV incident kinetic energy is shown in Fig. 30 and is typical of the data obtained. The curve is plotted immediately after flashing the target to approximately 2300°K for several seconds and represents data for a surface clean to less than 5% of full coverage. It is interesting to note that the upper energy limit is in excellent agreement with the value $a = (E_i - 2\phi)$ predicted by energy conservation in the simple model described in Section 2. The distribution is considerably sharper than that obtained by Propst and Lüscher for 50 eV N_2^+ ions at a polycrystalline tungsten surface (see Fig.51) and suggests that either kinetic broadening is significant at 50 eV or that there is a effect due to the single-crystal surface. The total yield is also considerably greater than in the previous work, but is nevertheless about one third that of an inert gas of similar ionization potential (Ar^+). It is this divergence that we attempt to explain by the introduction of molecular vibration energy sinks. The effect of ion kinetic energy is illustrated in Fig.31, for ion energies at 5 eV intervals from 15-to 30- eV. We would expect that the $N_o(E_k)$ curves form a smooth sequence as ion energy is varied, without sudden departures. It is seen that the distribution narrows considerably as ion energy is decreased, and that violation of the simple limit $(E_i - 2\phi)$ is observed at higher energies. In addition, the peak location shifts to lower values of E_k, and the peak height passes through a minimum at about 20 eV incident ion energy.

These trends must be taken as evidence of kinetic broadening effects ignored in the simplified treatment of section 2.2. The behaviour of the total yield γ_i is shown in Fig. 35. It is seen that the difference in yield between the clean and hydrogen-covered surfaces is approximately constant over the energy range considered, an effect observed by Propst and Lüscher (19) as well as Mahadevan et al.(23). There is a decrease in yield with decreasing energy that is reasonably gentle on this energy scale. It has been impossible to obtain distributions and yields at ion energies much below 15 eV (nominal) due to defocussing of the ion beam at the target. The data presented here, however, are considered reliable and free from the effects of lens defects. The onset of lens failure is easily seen in the $N_o(E_k)$ distributions as a violation of the asymptotic approach to the energy axis at large E_k. The data presented is well-behaved in this regard. The reproducibility of the data is illustrated in Fig.32 which represents the influence of adsorbed hydrogen for constant ion energy (30 eV). Curve (1) represents the clean condition and two such curves are shown superimposed. The subsequent transient effects of adsorption are represented by curves (2) to (7) for coverage up to an equilibrium level. Correlation between time and hydrogen adsorption level (or work function change $\Delta\phi$) is provided by the retarding-field diode curve from Fig. 28 for the case of a 30 eV beam. The work function change $\Delta\phi$ is tabulated for each curve in Fig.32 since the curves should be displaced to the left by this amount in order to compensate for the varying contact potential between target and sphere. Although the zero-field point established by thermionic measurements is correct for the case of clean (100) tungsten, it does not apply to the case of a gas-covered surface since the target work-function is increased by an amount as high as $\Delta\phi = 0.8$ volts. It was felt that the replotting of the distributions would be detrimental to the quality of the presented data. In a sense, the shift in potential of the origin of the Auger electron distribution is in itself a measurement of $\Delta\phi$ and hence surface coverage. With this point in mind, the peak of the distribution not only is drastically reduced by the adsorption of hydrogen but also is shifted to lower energies. Similar considerations apply to the family of curves for 15 $\overline{\text{eV } N_2^+}$ at a (100) tungsten surface (Fig.33). The effect of ion kinetic energy on the distributions for hydrogen-covered (100) tungsten is shown in Fig.34. The shift in retarding potential due to target adsorption is plainly visible and may be seen to be very close to the surface diode measurement of 0.8 volts. It is seen that the distributions for the clean and hydrogen-covered surface change with ion kinetic energy in a similar manner with respect to maximum energy (distribution broadness) and peak location. The peak height, however, appears to pass through a maximum at about 25 eV, an effect consistently observed. The variation of the <u>total</u> γ_i with ion kinetic energy is also similar for the clean and hydrogen-covered surface (Fig.35). The latter curves were obtained by plotting the ratiometer output against source anode potential for the spherical collector slightly electron-attracting. Alternately, the total yield may be plotted as a function of time after flashing so that a family of curves representing increasing hydrogen coverage may be obtained. The behaviour of γ_i with time closely resembles the "reflection" of the target work function variation (Fig.28) and suggests that for a given ion-surface combination the yield is quasi-linear with surface work function. This was a conclusion reached earlier when summarizing previous work in the field (see Fig.1).

A comparison of total yield data with that obtained by Propst and Lüscher (19) is shown in Fig.36; some comments regarding the total electron yields is given in section 6.3.

The total electron yield γ_i and its dependence on ion kinetic energy for N^+ ions incident on a clean and hydrogen-covered (100) tungsten surface are shown in Fig.37. It was not possible to obtain meaningful energy distributions due to the low signal-to-noise ratio which exists as a consequence of the small N^+ beam intensities ($\sim 10^{-11}$ amperes).

The total yields exhibit a behaviour and magnitude not unlike the diatomic N_2^+ ion, though the ionization potential of N^+ is approximately 1 volt less. We would expect the N^+ ion to behave in a manner similar to an inert gas of comparable ionization energy and incident velocity. The electron yield for Kr^+, for example, is about .04 (9) at a clean polycrystalline tungsten surface at an incident energy of 40 eV. The comparison is crude since the nature of the interaction potentials at close range will differ due to the high bonding energy of the nitrogen atom, but the yields are nevertheless of comparable magnitude.

6.2 At a polycrystalline Molybdenum Surface

6.2.1 The Nitrogen Ion Species N_2^+, N^+

In order to gain familiarity with experimental procedures prior to installing the single-crystal target, a number of experiments were performed using a polycrystalline molybdenum specimen. Although poorly characterized both physically and chemically, the surface yields interesting qualitative trends pertinent to the Auger process. Furthermore, the surface is perhaps typical of engineering-type materials in a high-altitude flight regime. The physical nature of the surface is believed relatively unimportant compared to its chemical state, which in this case consists of carbon contamination and gas adsorption. The high likelihood of surface carbon contamination due to diffusion of bulk impurities at elevated temperatures is discussed in some detail by Vance (20). In the latter work, the carbon impurity is removed by the somewhat drastic procedure of heating the target for about 30 minutes at 1700°K in 1×10^{-6} torr of oxygen.

The magnitude of the electron yields for the present surface indicates that the contamination level must be high. We consider the carbon to be a chemisorbed layer reducing the electron yield through a change in surface work function. Thermionic measurements performed by Vance indicate that the molybdenum work function is increased from 4.3 eV to about 4.7 eV due to carbon contamination. The electron yields for Ar^+ ions are correspondingly reduced by a factor of almost exactly two, so that in the present case we expect the yields to be similarly lowered from a carbon-free yield that is normally slightly higher than the clean-tungsten values. The adsorption of active gases from the high-vacuum chamber (again believed hydrogen) will further reduce the electron yield to a value perhaps 25% that of a clean molybdenum surface. Regardless of these considerations, we believe that the surface state is stable since the experimental results are reproducible, and that the equivalent work function is approximately 5.5 eV.

The energy distributions of electrons liberated by the Auger neutralization of N_2^+ at this contaminated Mo surface are shown in Fig. 38, and the corresponding total yields in Fig.41. An immediate observation is that in contrast to the results of the previous sections, the electron yield increases with decreasing ion kinetic energy. Recent work by Vance (21) substantiates this decreasing yield with increasing ion kinetic energy and further indicates that there is eventually a minimum in yield at about 75 eV ion energy. The magnitude of the yield indicates that the present surface is undoubtedly carbon-contaminated, since the reduction in γ_i expected from this source is as expected from the previous work with carbon-contaminated Mo (20). The distributions are very narrow, with an maximum energy independent of ion kinetic energy. It is more appropriate to compare this maximum not with $(E_i-2\phi)$ for a clean molybdenum surface but with a value (indicated a') for $\phi \approx 5.5$ eV. There is less evidence of kinetic broadening, moreoever, than for the (100) tungsten data. The energy distribution of electrons produced by the impact of 30 eV N^+ ions is shown in Fig.39 with a similar distribution for N_2^+ for comparison. This is a graphic demonstration of the effect of vibrational energy sinks, since the ionization potential for N_2^+ exceeds that of N^+ by 1 volt. The revised energy maxima predicted for this molybdenum surface are indicated by a' and b' for N^+ and N_2^+ respectively. The limit for N^+ is severely violated by an amount that is difficult to explain purely on the grounds of kinetic broadening. This point is discussed further in section 6.3.

The variation of the total yield for N^+ ions with incident ion energy is shown in Fig.42. The yield exhibits a strong dependence on ion velocity, and rises to a value at low energies which approaches that of a similar inert gas (Kr^+) reported by Hagstrum (12), namely .069 at 10 eV. These increases in yields for decreasing ion energy at a molybdenum surface are not necessarily anomalous to the relatively gentle decreases observed for the tungsten surface. A behaviour of this type was observed by Hagstrum (11,12) and is shown summarized by Kaminsky (7), pg. 269, for these same metals.

6.2.2. The Diatomic Hydrogen Ion H_2^+

The high velocities obtained for the hydrogen ion at even 30 eV result in poor performance of the ion beam at lower energies. This suggests that the problem is magnetic in nature, and most likely results from inadequate magnetic shielding. Nevertheless, an energy distribution function for electrons

---

* The author is indebted to D. W. Vance for communication of these results (Ref, 21, 22) prior to publication.

produced by the impact of 30 eV H_2^+ ions was obtained, and is shown in Fig. 40. The total yield is more readily attainable, however, and is shown in Fig.43 together with the previously described N_2^+ data. Once again the distribution is extremely narrow, and in agreement with the estimated energy maximum a'.

The sharp increase in the yield with increasing incident energy might indicate that kinetic ejection is still important at low energies for H_2^+. This might be expected, since the lighter ions are more efficient at transferring kinetic energy to the bound electrons of surface atoms in a manner believed to be purely velocity-dependent. This mechanism is proposed by Hagstrum to account for low-energy electrons observed for He^+ incident on a tungsten surface, but not predicted on the basis of purely potential ejection. The behaviour of γ_i for H_2^+ - Mo with incident ion energy is in excellent agreement with recent work by Vance (21) at energies down to 30 eV. The magnitude of the present yields indicates that carbon contamination is highly probable, since the present results are in agreement with carbon-contaminated values obtained in Ref. 24. It should be noted that there is a pronounced effect of incident ion energy in contrast to the previously-published inert gas ion data which is more nearly energy-independent.

In Fig.43, it it seen that an extrapolation of the N_2^+ and H_2^+ yields to energies such that the particle velocities are identical, results in an approximate matching of yields. This would be expected due to the high similarity of both ionization energy and vibrational state density. Thus if Fig.43 were replotted as γ_i versus velocity it would represent the yield of either N_2^+ or H_2^+ (E_i = 15.5 and 15.6 electron volts respectively). It is suggested that the electron yield for either ion species initially decreases with incident energy (potential emission with energy level shifts) passes through a minimum, and finally rises due to the eventual predominance of the kinetic broadening mechanism and ultimate transition to the purely kinetic emission process at energies above 100 eV. Vance (21), as previously mentioned, finds a minimum in the yield curve for (N_2^+ - Mo) at approximately 75 eV, so that on purely velocity arguments, we might expect the H_2^+ minimum to occur at ~ 20 eV. These values are in good agreement with Fig.43, as is the stronger variation in yield observed for H_2^+ as compared to N_2^+.

6.3. Discussion of Results

It will be shown that the variation in γ_i with ion kinetic energy may be attributed in every case to effects which broaden the $N_i(E_o+E_k)$ distributions beyond that formulated by the simple theory of Section 2.2. The variation in effective ionization energy due mainly to the attractive image forces has already been described. This would not introduce energy broadening if the transition probability had zero width on the s scale, since the ionization potential would be exact for ions undergoing Auger neutralization, i.e. $E_i'(s_o) \approx E_i - 3.6/s_o$ eV.

In reality the transition probability has finite width, such that for an exponential transition rate it is independent of ion velocity. As the incident velocity of the ion is increased, the most probable ion-surface separation for the transition decreases while the form of the transition probability remains invariant. One consequence is that the effective ionization potential is decreased, shifting the N_i distribution to lower energies, reducing the total electron yield for increasing ion velocity. The second consequence is that the N_i distribution is broadened, due to finite transition probability width, by an amount that is proportional to the gradient of $E_i(s)$. This broadening thus increases with incident ion energy since the transitions occur closer to the metal. The effect on the N_i distribution is symmetric at the low and high energy limits due to the manner in which broadening effects the Auger transform (Fig.47). The ends of the distribution are populated at the expense of the centre. The change in γ_i from this cause depends upon where the distribution is located with respect to the energy barrier E_o. For the ions studied here, only a portion near the high-energy tail lies beyond E_o so that kinetic broadening of the distribution <u>increases</u> γ_i because there are more electrons at energies capable of escape. In contrast, for He^+ the distribution lies entirely <u>above</u> E_o, so that kinetic broadening leads to a decrease in electron yield. Thus the observed variation in γ_i is a combination of competing effects due to energy level variation and distribution broadening.

There is an additional source of energy broadening due to the finite lifetimes of the initial and final states of the process, (Heisenberg broadening) which also increases with increasing ion velocity. The initial state has a lifetime determined by the transition rate for the process, and contributes to broadening of both the high and low energy regions of the N_i distribution. The final state has a finite lifetime because electrons removed by the Auger process leave "holes" in the filled portion of the conduction band which must be filled by electrons higher in the band by means of some secondary process. It is believed that only the low energy limit of the excited distribution is populated from the latter source. It is the explanation of the high energy tailing of the $N_o(E_k)$ distribution that is sought, so that Hagstrum incorporates only Heinsenberg broadening due to finite <u>initial</u> state lifetimes into his theory. It is an interesting consequence of Heisenberg broadening that in order to satisfy energy conservation there must be a corresponding spread in ion translational energy.

We are now in a position to discuss the behaviour of the experimental distribution functions and yields. Depending on the relative importance of energy level shifts or distribution broadening we may qualitatively obtain γ_i curves that either increase or decrease with ion energy, or even possess a minimum. The energy dependence appears stronger for the molybdenum surface, and this is also observed in the work of Hagstrum, summarized by Kaminsky (7) pg. 269. We argued earlier that both H_2^+ and N_2^+ at a Mo surface possess a minimum in γ_i with increasing ion energy, an effect observed for all inert gases with the exception of Ne^+. Furthermore, the decrease for Kr^+ up to energies of 100 eV or more is especially rapid, and is comparable to the N^+ result in a similar velocity range obtained here. The variation in γ_i with ion energy for the <u>tungsten</u> surface is more gentle and must indicate that the interaction potentials and transition rates are such as to produce a larger mean transition distance. The strongest dependence is again observed for the lighter ions, and once again the behaviour of N^+ is comparable to that of Kr^+ in the 100 eV range. It is interesting to consider the approach of extremely low energy (thermal) ions. The acceleration of such particles due to the attractive image force can be expected to increase their energies to perhaps 1.5 eV at the point of neutralization. Since this represents only a factor of three in velocity below the present results, we would expect the yields and distributions to differ little from those for 15 eV ions.

The comparison of the total yields with the work of Propst and Luscher (Fig.36) deserves comment. The present yields are considerably larger and in addition the distributions are narrower (Fig.51), even though the theoretical energy limit $(E_i-2\phi)$ appears valid in both cases. This is surprising, since in the present work, we find that at 30 eV the distributions have broadened considerably and further broadening would be expected at the 50 eV level used by Propst and Lüscher. The difficulty arises primarily because the surface used by the latter is poorly specified, at least in the open literature. It is suggested that the polycrystalline surface employed is either predominantly (110) in structure (ϕ = 5.2 eV), or if consisting of lower work function planes, is carbon contaminated such that the effective work function is approximately 0.75 volts above the present value for (100) tungsten (ϕ = 4.5 volts). This implies that the valid value of $(E_i-2\phi)$ for their work is perhaps 1.5 volts lower than in the present case (reducing γ_i) and that broadening of the distributions is also of this magnitude.

It is true that prior to obtaining the nitrogen ion data, Propst and Lüscher had obtained results for He^+ to compare with the earlier data of Hagstrum (11). However, as previously stated, the N_o distribution for the He^+-W system lies entirely above E_o that is, the lower limit of E_k is finite so that changes in surface work function of the above magnitude result in small changes in γ_i. Furthermore, the shift of the distribution function on the energy scale would go un-noticed since the zero-field point was located by the apparent origin of the function itself. In the measurement of the present data, inadequate surface cleaning or non-idealities in electron-collector geometry tend to <u>reduce</u> the total yields so that these factors are not relevant. It is natural to propose extra energy sources such as metastable ions, although recent work by Vance (22) indicates that extremely few survive the time-of-flight from source to target. In addition, the energy maximum of the $N_o(E_k)$ distributions strongly supports the value $(E_i-2\phi)$ expected for a ground-state ion within the amount reasonably explained by kinetic broadening effects.

In the case of N_2^+, the absence of variation in γ_i with changes in electron impact suggests the beam is entirely in the ground state, although a small population in the low-lying state $(^2\Pi_u)$ may go undetected. Significant populations in the higher states (Table 2) would result in larger increases in γ_i which are not observed (22). The lifetimes of these excited states for N_2^+ have all been measured and are all at least one order shorter than the minimum possible transit time through the apparatus (~40μs) obtained from a knowledge of lens potentials and assuming that the source residence time is zero. The latter is probably untrue, since it is determined by the complex potential structure in the source. The time spent in the ion source may thus be an order of magnitude greater than the transit time through the instrument. We thus conclude that the beam is in the ground electronic state upon arrival at the target. There remains the possibility of vibrational excitation in the incoming ion beam and Moran and Friedman (47) have considered this problem. Since for homonuclear diatomic ions vibrational transitions are not permitted, the electronic transitions from the short-lived A state will retain their former vibrational quanta. The calculation of the vibrational populations formed in the electron impact process indicated that 90% of all incident ions are in the ground state electronically and vibrationally, and of the remaining 10% a large majority possess only a single vibrational quanta (v = 1).

The situation for H_2^+ is considerably simpler. There are no known bound electronic states, so that experimentally the electron yield γ_i is highly insensitive to electron impact energy as expected. This result is reported by both Vance (22) and Mahadevan et al (24).

The excitation level of the N^+ ion beam is in some doubt. Vance reports that the value of γ_i is independent of the electron impact energy, although the published results (22) do not extend to ionization threshold. The metastable states $^1D_2$ and $^1S_0$ have lifetimes of 4.13 min. and 0.9 sec. respectively so that the apparent absence of these states from the beam suggests that the selection rules are obeyed even in low-energy electron impact ionization. This is surprising, and represents a discrepancy with recent measurements of charge transfer cross-sections. Both in the present case and in the work of Vance, there is no possibility of appreciable N_2^{++} concentrations which would result in very large electron yields because of the large value of E_i (~ 43 eV).

It is important to realize that small concentrations of N^+ in the low-lying $^1D_2$ state would be undetected by measurement of γ_i alone. The measurement of the energy distribution of secondary electrons can, however, indicate the presence of excited ion states, by observation of the energy maxima. In Fig.39 it may be seen that the distribution for N^+-Mo extends perhaps 1 eV beyond that for (N_2^+ -Mo) a situation that is unexpected since the ionization potential for N_2^+ exceeds that of N^+ by about 1 eV. Regardless of the state of carbon contamination in the surface the value of ϕ is equal for both distributions, so that the apparent recombination energy for N^+ exceeds the ionization potential by about 2 volts. This is precisely the height of the metastable level $^1D_2$ above the $^3P_0$ ground state, so that there may be a small number of excited N^+ ions that are insufficient to alter the total yield appreciably, but sufficient to shift the energy maximum. This proposal would perhaps resolve the earlier conflict in Vance's work.

Measurements of the dissociation energy of N_2 by Burns (50) show that at threshold both the N^+ ion and the N atom are in the ground state, but that the first break in the ionization efficiency curve occurs at 1.9 volts above onset, corresponding to the products

$$N\left({}^4S_0\right) + N^+\left({}^1D_2\right)$$

The above discussion has thus eliminated initial ion excitation as a possible alternative to a difference in work function in order to account for the higher yields in the present work compared to that of Propst and Lüscher.

Another explanation that is not easily refuted is that a significant fraction of incident ions undergo resonance neutralization and Auger de-excitation (transition B, Fig.44) at low incident ion energies. This process requires that an unoccupied excited level is adjacent to the filled portion of the conduction band, i.e. $\phi < (E_i - E_x) < E_0$. For nitrogen on (100) tungsten this limits the excited level to $4.6\ \text{eV} < E_x < 11.0$ eV if energy shifts are neglected. A most likely level is $^3\Sigma_u^+$ which gives rise to the forbidden Vegard-Kaplan Bands (~6 eV). The maximum energy of external electrons resulting from the Auger de-excitation of this level is $(E_x - \phi) \sim 1.5$ eV so that we could not support this hypothesis by observation of the high energy tail as in the case of Ne^+. The narrowness of the observed distribution does, however, add credence to this process, since its effect will be to populate the low energy portion of the distribution beyond that expected on the grounds of pure Auger neutralization (see Fig.51). Finite instrumentation time response will broaden the experimental distributions, so that the narrowness of the data is considered significant. The theory could be reworked to include this possibility, assuming vibrational excitation both at the molecular ground state and at $^3\Sigma_u^+$, and superimposing the resultant distributions in a manner reflecting the relative probabilities of the two mechanisms. (i.e. a fitting parameter). A procedure similar to this was adopted by Hagstrum (10) to explain the behaviour of Ne^+ at a tungsten surface, though in this case there was a considerable violation of the simple energy maximum (E_i-2ϕ).

The success of the pure Auger neutralization theory in matching Propst and Lüscher's distribution at 50 eV using Hagstrum's value of the escape parameter (Fig.51) is very encouraging. It is even better than shown, since the energy scales used are not identical. Propst and Lüscher used the distribution itself to locate the zero field point, whereas in reality the zero point lies to the left, so that the distribution appears to extend to negative energies. This anomaly is attributed to stray magnetic fields in the vicinity of the energy analyzer. In the present simple theory, our only fit to experiment is through the escape function parameter f. It must be increased in order to match the results at 15 eV (by equal areas or yields). By increasing this parameter we are in essence postulating an increased focussing of excited metal electrons towards the surface normal, before they surmount the surfac potential barrier. It could be argued that this is reasonable in a material possessing less disorder and preferred directions for electron motion, one of which is the normal itself. Hagstrum (13) finds that a value of f = 4.8 is necessary to fit data for He^+ on Ge (111) assuming the required large escape probability is entirely due to the anisotropy of P_Ω. The escape probability is also increased by the fact that the surface barrier is not planar, as well as the anisotropy effect. The bulge in the equi-potential surfaces outside the solid leads to a greater critical angle θ_c than that predicted for a planar boundary. It is possible that a better fit could be obtained by fixing f = 2.2. and including the effect of Auger de-excitation mentioned earlier, since the high-energy tail of both experimental distributions (Fig.51) is well-described by the simple theory of section 2.2.

The broadening of the $N_o(E_k)$ distributions is obtained by Hagstrum (10) by convoluting the T(E) distributions with a pair of Gaussian broadening functions of half-widths 2.37 ξ_1 and 2.37 ξ_2 where ξ_1 and ξ_2 are the standard deviations attributed to finite width of the transition probability and lifetimes of initial states respectively. This procedure is acceptable at low velocities, and in general $\xi_1 > \xi_2$ for this case. Values of $\xi = \sqrt{\xi_1^2 + \xi_2^2}$ appropriate for the present case are of the order of 0.25 eV so that the width at half-maximum of the Gaussian broadening function is about 0.6 eV. This is sufficient to account for the high energy tail beyond E_a at higher incident ion energies. The magnitude of ξ_2 is insignificant in altering ξ so that to a good approximation

$$\xi = \frac{0.53}{a} \left[\frac{dE_i'}{ds} \right]_{s_o}$$

where "a" is a constant specifying the dependence of the matrix element on s. (taken as 2 x 10^8 cm^{-1}). If s_o is sufficiently large that $E_i' \approx E_i - 3.6/s$ (i.e. image forces dominate the interaction), then

$$\xi \simeq \frac{0.53}{a}\left(\frac{3.6}{s_o^2}\right)$$

for which $s_o \sim 2.5$ Å. This means that the effective ionization potential is on the average 1.5 eV below the free space value, but that kinetic broadening is active to compensate for the apparent decrease in maximum electron kinetic energy ($E_i' - 2\phi$). The effects of image forces on ion kinetic energy and trajectory (if other than normal incidence) must therefore be taken into account in order to use the equivalence of ionized and neutral molecules as a gasdynamic tool. The finite width of the transition distance (~ 0.5 A) about the most probable value s_o will consequently introduce an angular spread about the most probable perturbed angle of incidence (steepened towards normal).

It is worthwhile to discuss the areas of immediate application of the present results. Of direct interest is the electron-sheath formation mechanism in the vicinity of a satellite at altitudes of 90 to 250 km for which secondary electron emission by incident ions and metastable neutrals determines the net charged-particle flux and hence equilibrium potential of the surface. Hagstrum (10) has shown that the secondary electron yields and energy distribution functions for metastable neutral atoms are identical to those for ground-state ions. This is because it is believed that a two-stage process exists for the de-excitation of incident metastable species, namely resonance ionization followed on closer approach by Auger neutralization. At the lower altitude limit above, the natural ionization level is low and the vehicle charges positive as a result of electron ejection by incident neutral particles. A significant fraction of the latter must be electronically excited, since the magnitude of the effect cannot be explained on the basis of kinetic ejection alone. At higher altitudes, the equilibrium potential is reduced by increasing accretion from the ionosphere and eventually changes polarity. A second polarity reversal may occur at extreme altitudes (>1000 km) due to the eventual dominance of photoelectric emission (daylight only). The question of sheath density and thickness in the low altitude region has been open to some speculation due to the lack of experimental knowledge on the relevant particle-surface interactions. In particular, the populations of excited states of neutral particles in the ambient and the energy distribution function of ejected electrons are required in order to formulate the space-charge equations governing sheath formation and structure. The present results concerning the energy distribution function are readily applicable to this problem, although the equilibrium adsorption state of satellite surfaces is as yet undetermined. In the altitude region presently considered, the ion flux at the vehicle surface is predominantly molecular nitrogen and typically 10^{11} ions/cm^2-sec, which is of the same order as the present experimental values. In the present work we have an estimate of the effectiveness of the normal momentum of incident molecules in desorbing surface gases D (σ), that exceeds unity probability. Whether the adsorption rate is positive or negative will thus depend on the relative number of incident particles trapped at the surface S (σ), which is a function of angle of incidence. The equilibrium surface state might then be expected to vary over the surface between the two extremes of a relatively clean surface at normal incidence (high D (σ), low S (σ)) to saturation coverage at tangential incidence (low D (σ), high S (σ)).

A second area of application is in regard to the non-idealities in the behaviour of electrostatic (Langmuir) probes. The ejection of secondary electrons by thermal energy ions from a plasma occurs as a result of potential emission processes, although as discussed earlier the ion energy at the point of neutralization will be several electron-volts due to the predominantly attractive ion-metal interaction potential. This surface effect results in an over-estimation of the ion current (and hence ion number density) of up to 30 per cent depending on the energy excess E_a and the surface adsorption state. In common with the satellite surface, the probe surface condition is rarely well-specified and the secondary emission effect is seldom considered, since the quantitative information from the technique is not yet of such precision.

7. CONCLUSIONS

An ion beam facility has been constructed that is capable of laboratory simulation of the ionospheric flight regime in the energy range 10 to 30 eV or greater. With minor reservations, this facility may also be used for the simulation of neutral molecule-surface interactions with the advantages of extremely narrow energy spread and ease of energy variation. In fact, it offers at present the only practical method by which gas particle velocities of this magnitude can be attained. Experiments have been performed under stringent conditions of high vacuum, to obtain new data concerning the Auger neutralization of atmospheric ion species at a well-characterized (single crystal) surface. For the cases where comparison with other work is possible (Mo), this data represents an extension to lower ion energies but provides excellent agreement with the quantitative and qualitative predictions of previous high ion-energy data. The effects of surface adsorption on the electron energy distributions, which represent the means by which we have gained information about the neutralization process, have been observed transiently by the incorporation of modern instrumentation techniques. The data-reduction system employed is believed a new approach to the problem, and represents an alternative to existing methods, generally more complex.

A theory revision to account for the failure of the inert-gas formulation to adequately describe the neutralization of diatomic ions has provided encouraging quantitative agreement with experimental data. The hypothesis of vibrational excitation during the Auger neutralization process has been shown to be a plausible explanation of the experimental results using reasonable assumptions concerning the physical parameters pertinent to the mechanism. The effect of ion kinetic energy although not included in the theory, has been qualitatively explained. It has been suggested that the two-stage process is more probable than formerly believed for the low ion energies used. Although this mechanism or the simple formulation of the revised theory prohibits agreement with the present data, in both overall yield and energy distribution, the salient features are quantitatively represented in a fashion not at all possible using the inert gas theory.

It is felt that the ultimate solution to the theoretical problem lies not in detailed modifications of an already overtaxed existing theory but in an entirely fresh approach, based firmly on first principles, such as that presently considered for the simpler He^+ and Ar^+ cases by Howsmon and Wenaas (18). The difficulties to be experienced in applying a rigorous quantum mechanical treatment to complex diatomic ion interactions cannot be overstressed, however.

A natural extension of this work that would provide additional insight into the process is the measurement of the spatial distribution of secondary electrons. The low signal levels, however, represent a formidable challenge especially for the case of reactive ion species for which the experimental time constants are short. A measurement of this type would provide information concerning the preferred spatial distribution prior to escape, as well as the surface properties. There are diagnostic possibilities in this respect.

In addition, the small reflected ion currents observed ($R < 1\%$) may contain significant information concerning the surface structure and composition, having undergone close-range interactions. Work of this nature has been performed by Smith (49) at higher energies of the order of 2 eV, although the perturbation of the surface gaseous state prevents correlation between inelastically scattered ions and the chemical state of the surface. Smith exploits this desorption to obtain clean-surface data in an active-gas environment, and in the present work we have evidence of such effects even at 15 eV incident ion energy.

REFERENCES

1.	French, J. B.	"Molecular Beams for Rarefied Gasdynamic Research", AGARDograph 112, April 1966.
2.	Prince, R. H.	" A Low Energy Nitrogen Ion Beam" University of Toronto, Institute for Aerospace Studies TN.80, May, 1965.
3.	Amdur, I. Mason, E. A.	J. Chem, Phys. 25 632 (1956)
4.	Utterback, N. G. Miller, G. H.	"Fast Molecular Nitrogen Beam" Rev. Sci. Instr. 32, 1101 (1961)
5.	French, J. B. O'Keefe, D. R.	"High Energy Scattering of Inert Gases from Well-Characterized Surfaces." I. Experimental.Proc. 6th Int. Symp. on Rarefied Gasdynamics (1968) (to be published)
6.	Massey, H.S.W. Burhop, E.H.S.	"Electronic and Ionic Impact Phenomena" Oxford University Press, London, (1956)
7.	Kaminsky, M.	"Atomic and Ionic Impact Phenomena on Metal Surfaces" Academic Press (1965)
8.	Hagstrum, H. D.	"Instrumentation and Experimental Procedure for Studies of Electron Ejection by Ions and Ionization by Electron Impact" Rev.Sci.Instr.24, 1122 (1953)
9.	"	"Auger Ejection of Electrons from Tungsten by Noble Gas Ions", Phys. Rev. 96, 325 (1954)
10.	"	"Theory of Auger Ejection of Electrons from Metals by Ions" Phys. Rev. 96, 336 (1954)
11.	"	"Auger Ejection of Electrons from Tungsten by Noble Gas Ions" Phys. Rev. 104, 317 (1956)
12.	"	"Auger Ejection of Electrons from Molybdenum by Noble Gas Ions" Phys. Rev. 104, 672 (1956)
13.	"	"Theory of Auger Neutralization of Ions at the Surface of a Diamond-Type Semiconductor" Phys. Rev.122, 83 (1961)
14.	Hagstrum, H. D. Takeishi, Y.	"Effect of Electron-Electron Interaction on the Kinetic-Energy Distribution of Electrons Ejected from Solids by Slow Ions" Phys. Rev. 137, A304 (1965)
15.	Shekhter, S. S.	"Neutralization of Positive Ions and Ejection of Secondary Electrons", Zh.Eksper, Teoret. Fiziki 7, 750 (1937)

16.	Cobas, A. Lamb, W.E. Jr.	"On the Extraction of Electrons from a Metal Surface by Ions and Metastable Atoms" Phys. Rev. 65, 327 (1944)
17.	Propst, F.M.	"Energy Distribution of Electrons Ejected from Tungsten by He$^+$" Phys. Rev. 129, 7, (1963)
18.	Howsmon, A.J. Wenaas, E.P.	"Theory of Auger Ejection of Electrons from Metals by Ions" Proc. 4th Int. Materials Symposium (1968), Berkeley, California. (to be published)
19.	Propst, F.M. Lüscher, E.	"Auger Electron Ejection from Tungsten Surfaces by Low-Energy Ions" Phys. Rev. 132, 1037 (1963)
20.	Vance, D. W.	"Auger Electron Emission from Clean and Carbon-Contaminated Mo" Phys. Rev. 164, 372, (1967)
21.	Vance, D. W.	"Auger Electron Emission from Clean Mo Bombarded by Positive Ions. II. Effect of Angle of Incidence" Phys. Rev. 169 , No.2, 252 (1968)
22.	Vance, D. W.	"Auger Electron Emission from Clean Mo Bombarded by Positive Ions. III. Effect of Electronically Excited Ions" Phys. Rev. 169, No.2, 263 (1968)
23.	Mahadevan, P. Layton, J. K. Medved, D. B.	"Potential and Kinetic Electron Ejection from Molybdenum by Argon Ions and Neutral Atoms" Phys. Rev. 129, 2086 (1963)
24.	Mahadevan, P. Magnuson, G.D. Layton, J. K.	"Secondary-Electron Emission from Molybdenum Due to Positive and Negative Ions of Atmospheric Gases". Phys. Rev. 140, A1407 (1965)
25.	Francis, G.	"Ionization Phenomena in Gases" Butterworths (1960)
26.	Spangenberg, K. R.	"Vacuum Tubes" McGraw-Hill (1948)
27.	Pierce, J. R.	"Theory and Design of Electron Beams" Van Nostrand (1954)
28.	Stephens, W.E.	"Magnetic Refocussing of Electron Paths" Phys. Rev. 45, 513 (1934)
29.	Nier, A. O.	" A Mass Spectrometer for Routine Isotope Abundance Measurements" Rev. Sci. Instr. 11, 212 (1940)
30.	Goodyear, C.C. von Engel, A.	"Atomic Ion Production in Radio-Frequency Ion Sources" Proc. 5th Int. Conf. on Ionization Phenomena in Gases Ed. H. Maecker, North Holland (1962) Vol. 1. Pg. 203.
31.	Varney, R. N.	"The Formation and Stability of Molecular Ions" Loc. Cit. Pg. 42.

32.	Giordmaine, J.A. Wang, T. C.	"Theory of Molecular Flow in Long Parallel Tubes" J. Appl. Phys. 31, 463 (1960)
33.	Hagstrum, H. D. Pretzer, D. D. Takeishi, Y.	"Focussed Slow Ion Beam for Study of Electron Ejection from Solids" Rev.Sci Instr. 36, 1183 (1965)
34.	Hanley, T. E.	"Spectral Emmissivity and Electron Emission Constants of Thoria Cathodes" Journ.Appl. Phys. 19, 583 (1948)
35.	Estrup, P. J. Anderson, J. Danforth, W. E.	"LEED, Studies of Thorium Adsorption on Tungsten" Surface Science 4, 286 (1966) North-Holland Publ. Co. Amsterdam.
36.	Simpson, J. Arol.	"Retarding Field Energy Analyzers" Rev. Sci. Inst. 32, 1283, (1961)
37.	Propst, F. M. Lüscher, E.	"Apparatus for the Study of Ejection of Auger Electrons from Solid Surfaces" Rev. Sci. Inst. 34, 574 (1963)
38.		"Applications Manual for Computing Amplifiers" Philbrick Researches Inc. (1966)
39.	Schmid, H.	"Digital Meters for Under $100" Electronics, No.28, (1966) Pg. 88
40.	Redhead, P. A.	"Chemisorption on Metals under Ultra-High Vacuum Conditions" Paper presented at Symposium on Electron and Vacuum Physics, Balatonfoldvar, Hungary, Sept, 1962
41.	Estrup, P. J. Anderson, J.	"Chemisorption of Hydrogen on Tungsten (100)", J. Chem. Phys. 45, 2254 (1966)
42.	Madey, T. E. Yates, J.T. Jr.	"Kinetics of Desorption of the β-Nitrogen States Chemisorbed on Tungsten", J. Chem. Phys 44, 1675 (1966)
43.	O'Keefe, D. R.	"The Scattering of High Energy Argon Atoms from A Well Characterized (100) Tungsten Surface" UTIAS Report. No.132 (July, 1968)
44.	Cullity, B. D.	"Elements of X-Ray Diffraction" Addison-Wesley Pub. Co. Inc. (1959)
45.	Barrett, C.S.	"Structure of Metals" McGraw-Hill Book Co. Inc. (1952)
46.	Anderson, J. Danforth, W.E.	"Low Energy Electron Diffraction Study of the Adsorption of Oxygen on a (100) Tungsten Surface" J. Franklin Inst. 279, 160 (1965)
47.	Herzberg, G.	"Molecular Spectra and Molecular Structure I. Spectra Of Diatomic Molecules" D.Van Nostrand Co.Inc. (1950)

48. Moran, T. F.; Friedman, L. "Cross Sections and Intramolecular Isotope Effects in AB-HD Ion-Molecule Reactions" J. Chem. Phys. 42, 2391, (1965)

49. Smith, D. P. "Scattering of Low-Energy Noble Gas Ions from Metal Surfaces" J. Applied Phys. 38, 340 (1967)

50. Burns, J. F. "On the Heat of Dissociation of N_2" J. Chem. Phys. 23, 1347 (1955)

APPENDIX A: THEORETICAL DESCRIPTION OF THE AUGER NEUTRALIZATION OF N_2^+ AT A CLEAN TUNGSTEN SURFACE

The derivation of the electron energy distribution function $N_o(E_k)$ will be summarized for the N_2^+ - W system, assuming the following values of $E_i = 15.5$ eV, $E_d = 7.37$ eV, $E_o = 10.8$ eV and $E_F = 6.4$ eV. The vibrational energy levels are numerically given by

$$E_v = 0.304(v + \frac{1}{2}) - 0.00186\,(v + \frac{1}{2})^2 \text{ eV}$$

where v is the vibrational quantum number. The inclusion of anharmonicity is required to provide a better estimation of the degeneracy factor at high values of v. The vibrational distribution function $N_v(E_v)$ is obtained by fixing E_v and calculating the number of final states permissible according to the limits imposed on the excited electron energy E:

$$E_F \leq E \leq (E_i - 2\phi + E_o - E_v)$$

where E_v is further restrained to values below the dissociation limit. Assuming a density of final electron states $N(E) \alpha \sqrt{E}$, the resulting $N_v(E_v)$ distribution is given by

$$\begin{aligned} N_v(E_v) &= K\left\{(2E_F - E_v)^{3/2} - 4.37\right\} & 0 \leq E_v < 7.37 \text{ eV} \\ &= 0 & E_v > 7.37 \text{ eV} \end{aligned}$$

where K is a constant. This function is shown plotted in Fig. 46 normalized to the value at v = 0.

The Auger transform will next be calculated assuming $N_c(E) = K_1$, a constant, permitting calculation of $N_i(E_o + E_k)$ in simpler, closed form. The transform is then given by

$$\begin{aligned} T(E) &= \tfrac{1}{2} K_1^2 E & 0 \leq E \leq E_F/2 \\ &= \tfrac{1}{2} K_1^2 (E_F - E) & E_F/2 \leq E \leq E_F \end{aligned}$$

This function is shown in Fig. 47 as well as that for $N_c(E) \alpha E^{\frac{1}{2}}$. Also shown is the broadened transform (dotted) assuming a calculated Gaussian broadening factor $\xi = 0.123$ eV for a 10 eV N_2^+ ion, to justify the exclusion of broadening effects in the calculation. The $N_i(E_o + E_k)$ distribution was previously written as (section 2.2)

$$N_i(E_o + E_k) = G.\,(v_k + 1).\,N(E_o + E_k) \int_{\text{available } E_v} N_v(E_v)\, T\left[\tfrac{1}{2}(E_k + E_v + 2E_o - E_i')\right] dE_k$$

The integration may be performed using E, the mean energy of participating electrons, as the variable of integration, while fixing $(E_o + E_k)$. The function is thus evaluated over the conduction band $0 \leq E \leq E_F$ in two half-range integrations corresponding to the split transform regions $0 \leq E \leq E_F/2$ and

$E_F/2 \leq E \leq E_F$. The integration limits may not coincide with the latter limits since there are energy constraints on the variable of integration. <u>Firstly</u>, E_v is always positive, which implies from the energy relation that $E \geq (E_o + E_k - E_i + E_o)$. Since $(E_o + E_k)$ is the excited electron energy, it must exceed the Fermi energy E_F since all levels below this energy are filled. Thus the lower limit of integration is given by the above inequality and not by $E = 0$. Furthermore, we find numerically that for $(E_o + E_k) > 11.0$ eV this lower limit exceeds $E_F/2$ so that only the second range of $T(E)$ is required. Secondly, it has been assumed that $E_v < E_d$, placing an upper bound on E when $(E_o + E_k)$ is low enough $(< E_i - 2\phi + E_o - E_d)$ to permit dissociation. That is, for $(E_o + E_k) < 10.03$ eV, the upper bound on E is no longer E_F but $\frac{1}{2}(E_o + E_k + E_d - E_i + E_o)$. Thus there are three distinct ranges of integration depending on the excited electron energy, two requiring integration over the entire conduction band, and one over only the upper half. The vibrational distribution function $N_v(E_v)$ may be rewritten in terms of the variables E, E_k so that the entire integration over initial states is performed using E as variable with E_k fixed. The expression for the energy distribution of excited metal electrons is thus

$$N_i(E_k + E_o) \; \alpha \; (v_k+1) . \; N(E_o + E_k) \left\{ \int_b^{E_F/2} N_v(E, E_k)(E) \, dE + \int_{E_F/2}^{b+E_d} N_v(E, E_k)(E_F - E) \, dE \right\}$$

$$E_F < (E_o + E_k) < (E_i - 2\phi + E_o - E_d)$$

$$\alpha \; (v_k+1) . \; N(E_o + E_k) \left\{ \int_b^{E_F/2} N_v(E, E_k)(E) \, dE + \int_{E_F/2}^{E_F} N_v(E, E_k)(E_F - E) \, dE \right\}$$

$$(E_i - 2\phi + E_o - E_d) < (E_o + E_k) < (E_F/2 + E_i - E_o)$$

$$\alpha \; (v_k+1) . \; N(E_o + E_k) \left\{ \int_{E_F/2}^{E_F} N_v(E, E_k) \, (E_F - E) \, dE \right\}$$

$$(E_F/2 + E_i - E_o) < (E_o + E_k) < (E_i - 2\phi + E_o)$$

where "b" is the bound given by $b = E_o + E_k - E_i + E_o$. By assuming the density of final states as $N(E_o + E_k) \; \alpha \; (E_o + E_k)^{\frac{1}{2}}$, the resulting energy distribution of excited metal electrons prior to escape is shown in Fig. 48 normalized to one excited electron per incident ion. The distribution neglecting vibrational excitation is shown for comparison. Since only those electrons of energy greater than E_o have any probability of escape, we can see that the yield of free electrons will be drastically lowered from the inert-gas value.

The energy distribution of free electrons $N_o(E_k)$ is obtained by means of the parametric escape function shown in Fig. 49 for three values of the parameter f. The curve for f=1 is that for an isotropic distribution of excited electrons over all angles θ_1. The curve for f = 2.2 is that used by Hagstrum to fit his data for He^+ ions incident on a polycrystalline tungsten surface. The parameter f = 3.0 provides the best fit of the theory to the present results. The corresponding $N_o(E_k)$ functions are shown in Fig. 50 and a comparison with both the present data and that of Propst and Lúscher is given in Fig.51.

The procedure used to estimate the spatial angular flux $J_\Omega(\theta_2)$ was outlined in section 2.2, and some details of the calculation will be given at this time. For the N_2^+ - W system, $(E_o + E_k)$ is limited to a value $(E_i - 2\phi + E_o)$ which is numerically approximately 1.6 times E_o. This means that the critical angle for escape θ_c has a maximum of $\cos^{-1}(1/1.6)^{\frac{1}{2}} \simeq 38$ degrees for this ion-surface combination. This defines the range of θ_1 values to be sampled uniformly in $\sin\theta_1$ - space. Having selected a particular value of θ_1 we calculate the minimum value of E_k that will escape in order to define the limits for sampling uniformly over all E_k. For example, only those electrons having energy (with respect to the bottom of the conduction band) between 1.46 E_o and 1.6 E_o need be considered for θ_1= 20 degrees.

By sampling E_k in uniform increments at a given θ_1, we perform the calculation of how many electrons are refracted to the angle θ_2 given by the refraction relation. A summation at each θ_2 is performed when the sampling of θ_1 and E_k is complete. The resulting distribution is shown in Fig. 52 assuming Hagstrum's value of the escape function parameter f = 2.2. The chosen increments of E_k and $\sin\theta_1$ were 0.2 eV and 0.0349 respectively.

APPENDIX B: OPERATIONAL DESCRIPTION OF THE DVM/RATIOMETER.

A brief description of the detailed operation may now be given, with reference to Fig. 15. The left-hand side of the diagram represents the pulse-width modulator, and the right the counter section. We indicate the two voltage inputs by A and B, and have shown the operation for A as numerator, although provision is made in the instrument for either A or B to act as numerator without disconnecting input leads. Voltage ranges are manually selected (Fig.16) by inserting feed-back resistors by means of a three-pole switch which also provides the required input compensations and a logic signal to be used in determining decimal point location, while maintaining constant input impedance. The input voltage is amplified so that the range amplifiers' output (A', B') is always about 6.4 volts full scale. A front-panel indication (OVERLOAD) is provided when this level is exceeded, since the particular values of A or B are not always known when in ratio mode. During the time interval denoted T_1, the scaled numerator voltage is applied to the integrator input by analog switch S_1, which is controlled by IC logic. At the end of this period, the capacitor is charged to an undetermined value, but the direction of integration (or numerator polarity P_N) is observed.

During the time interval denoted t_x, the analog switch S_2 or S_3 applies a voltage proportional to the denominator of appropriate polarity to discharge the integrator capacitor, determined by comparing P_N and P_D. The scaled denominator voltage B' may require polarity inversion, so that both B' and its polarity-inverted form B" are available at the logic-controlled switches S_2 and S_3. If RC is the integrator time constant, then

at the end of T_1, $$V_{int} = \frac{1}{RC}\int_0^{T_1} A'dt = A'\frac{T_1}{RC}$$

during t_x, $$V_{int} = A'\frac{T_1}{RC} - \frac{1}{RC}\int_0^{t_x} B'dt = A'\frac{T_1}{RC} - B'\frac{t_x}{RC}$$

at the end of t_x, $V_{int} = 0$, so that

$$\frac{t_x}{T_1} = \frac{A'}{B'} = \frac{V_N}{V_D}$$

The above relationship is thus completely independent of the integrator time constant RC. The time interval T_1 is generated by the master counter in the digital section, and may be held constant to the order of parts per million, so that t_x is a function of the ratio V_N/V_D only. Since the same digital counter is used to generate T_1 and measure t_x, constancy of time interval T_1 is not required, however, provided the change in counter frequency is negligible within a given up-down integration cycle. In the present instrument, provision is made for time-interval measurement so that a precise reference frequency is required. If the absolute value of input A is required, the denominator is replaced by a reference voltage $\pm V_R$ (nominally 4 volts) supplied by a high-quality zener-diode circuit (Fig.16). The integrator is supplied with input-offset compensation and a provision is made so that the capacitor is automatically discharged by a field-effect transistor should t_x exceed the full-scale value of 16 ms. A front panel lamp (OFLO) indicates this condition and requires a change of input range in order to provide a correct measurement. A comparator at the integrator output detects both the output polarity required by the switch logic, storing it in a flip-flop during T_2, as well as the instant at which the capacitor is completely discharged. The comparator output V_c' then changes state. A definite "snap-action" is provided by an IC Schmitt trigger (Fig. 17), whose output V_c is gated primarily with T_1, P_N and provides the <u>trailing</u> edge of the t_x pulse. The <u>leading</u> edge of the pulse is provided by the end of the T_1 period. The integration will normally not proceed again until a delay permitting digital operations has elapsed (4 µs). In the case of the OFLO condition being invoked, approximately 2 ms. is provided to discharge the capacitor to a negligible value. Thus T_2, which is the logic complement of T_1, does not have a standard duration and consequent dead-time as in Ref. 36, for example. This allows a maximum sampling rate since T_2 is never longer than necessary.

The digital portion of the instrument (Figs. 18, 19) generates T_1 and measures and displays the duration of the t_x pulse. The interval T_1 has been chosen such that the displayed value of the duration of the t_x pulse is numerically equal to the ratio of input voltages, A/B, in the ratio mode, or the absolute value of A or B in the digital voltmeter mode. The digital section may be operated entirely independently from the pulse-width modulator, however, and be used to measure the time intervals of externally-generated signals. For this purpose, a time-interval pulse-shaper is provided (Fig.18) consisting of a Schmitt trigger for measuring TIME INTERVAL and an R-S flip-flop configuration for measuring elapsed time between START and STOP pulses. An accurate clock is provided by a crystal-controlled multivibrator (Fig.18) whose frequency may be trimmed to 1MHz ± 1 Hz, with a temperature coefficient of one part per million per degree Centigrade. In addition, a 10 Hz oscillator derived from line frequency is provided for time interval measurements up to 1600.0 seconds. The master binary-coded decimal counter (weighted 1-2-4-8) first generates the T_1 interval by toggling the T_1- T_2 flip-flop in the upper right of Figs. 15, 19, after registering <u>exactly</u> 10,000 clock pulses. The master counter then registers the number of clock pulses occuring during t_x. This number is transferred into the storage register in BCD form and converted to a decimal representation as required by the readout lamps. These digital operations are controlled by the sequencer (Fig.18). After generating the T_1 interval, the master counter is reset to zero by the leading edge of the t_x pulse. In normal operation, other than OFLO, the trailing edge of the t_x pulse triggers simultaneously two monostables.

The first is a 4 µs monostable (INHIBIT) whose purpose is to prevent further clock pulses from entering the master counter while the total number of counts accumulated in t_x is being transferred to storage. The second is a 2 µs monostable (LOAD) at the end of whose period the contents of the master counter are transferred to storage. When the INHIBIT monostable resets, the master counter is again reset to zero (RESET), the T_1- T_2 flip-flop is set to the T_1 state (SET T_1) and the CLOCK signal is reapplied to the master counter. If the OFLO condition occurs (t_x > 16000 clock pulses), the INHIBIT monostable width is increased from 4 µs to nominally 2 ms. During this time the OFLO signal discharges the integrator capacitor by means of a field-effect transistor to speed the recovery of the instrument from overloads. The number displayed on the readout lamps will be exactly 16000 when OFLO occurs. The digital readout is provided by four Nixie tubes (type 6844A) each driven by a bank of ten high-voltage switching transistors (2N4410) and actuated by IC's used to decode the 17-bit binary number. In normal operation the readout indicates every sample taken, (40 to 100 per second). Jitter in the least-significant digit at this rate can make interpretation of the display difficult. The LOAD monostable is therefore gated optionally with a 1 Hz square wave derived from line frequency, so that although the storage and D to A conversion sampling rates are unchanged, the numerical display is changed only once a second.

The Digital-to-Analog converter is shown in Fig.20. Each of the 17 bits from the storage register is used to steer current of appropriate weighted value into or away from the summing point of a current-to-voltage converter, using the double-diode MSD6100. Adjustment is provided for both the current-determining resistances and for input voltage offset of the MC1433 operational amplifier to provide conversion accuracy to at least 0.1% of full scale (8 volts). The full-scale current necessary for this performance is beyond the output capability of the operational amplifier, so that a simple emitter-follower output buffer is required (2N3903).

The power supplies required for the instrument are mounted below the bank of circuit boards and make use of active filtering in the 0.1% (line and load) regulated ± 15 and -50 volt zener supplies, to conserve weight and space. The logic power (3.6 volts, 2.5 amperes) does not require critical regulation, and is derived by a zener-controlled series-regulated supply, as is the 220 volt Nixie voltage. The total power consumption for the entire instrument is approximately 25 watts.

TABLE 1

σ mol/cm^2 x 10^{14}	Sticking Probability			Desorption Coefficient		
	S	S'_{15}	S'_{30}	D_{15}	D_{30}	D_{30}/D_{15}
2.5	0.66(7)	0.583	0.552	4.62	6.48	1.40
5.0	0.218	0.205	0.198	0.84	1.25	1.49
7.5	0.0807	0.0729	0.0703	2.76	3.72	1.35

TABLE 2

ION BEAM EXCITED-STATE POPULATION DATA

	State	Electron Energy (eV)	Lifetime	Population after transit
N_2^+	$X\,^2\Sigma_g^+$	15.		100%
	$A\,^2\Pi_u$	16.7	3×10^{-6} s	0
	$B\,^2\Sigma_u^+$	18.7	6.6×10^{-8} s	0
	$^4\Sigma_u^-$	20.9	8×10^{-6} s	
N^+	$^3P_0$	24.32		
	$^1D_2$	26.22	4.13 min.	
	$^1S_0$	28.38	0.9 s	

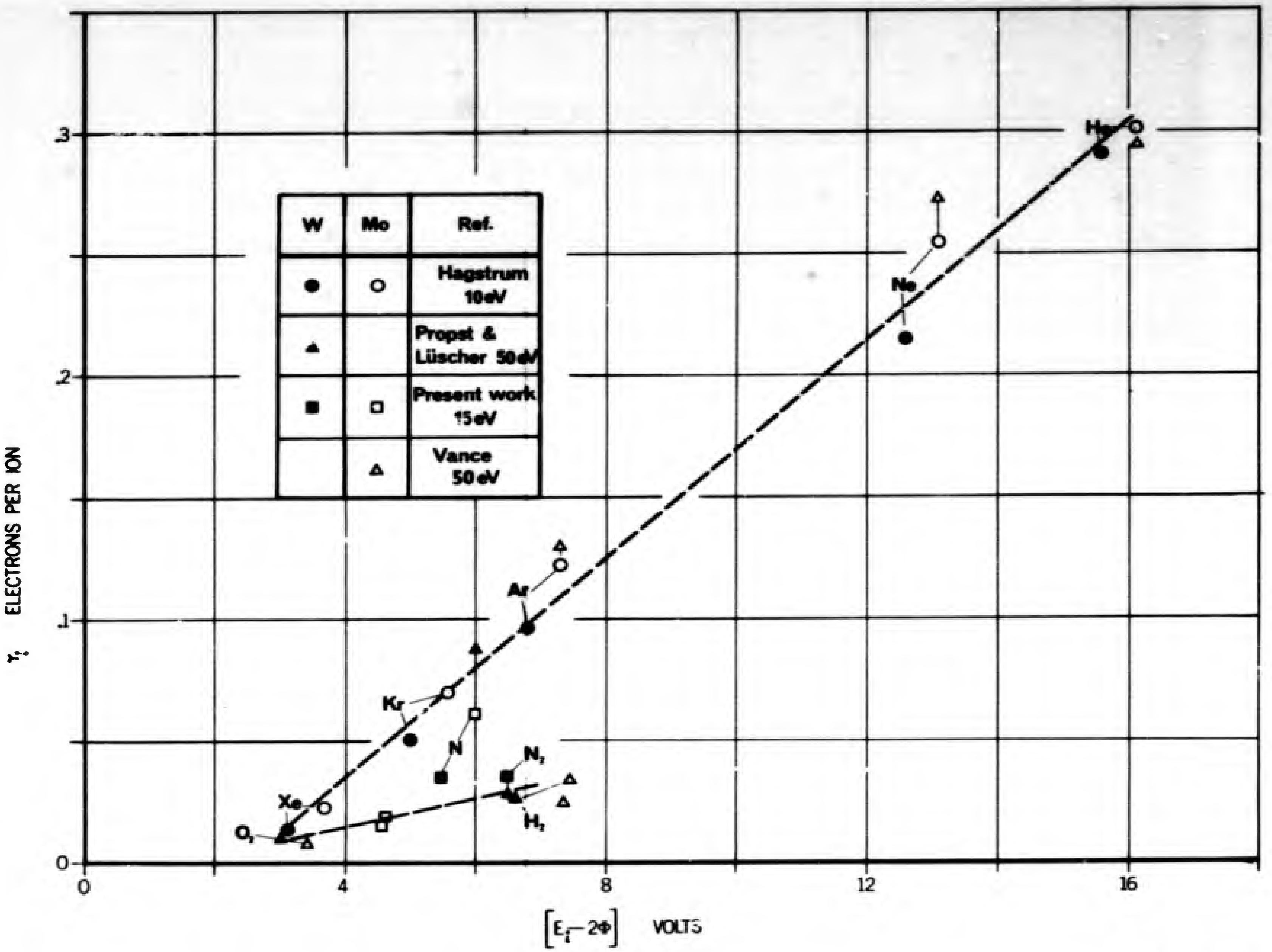

FIG. 1 A SUMMARY OF ELECTRON YIELD DATA PLOTTED AGAINST THE "ENERGY EXCESS" $E_i - 2\Phi$

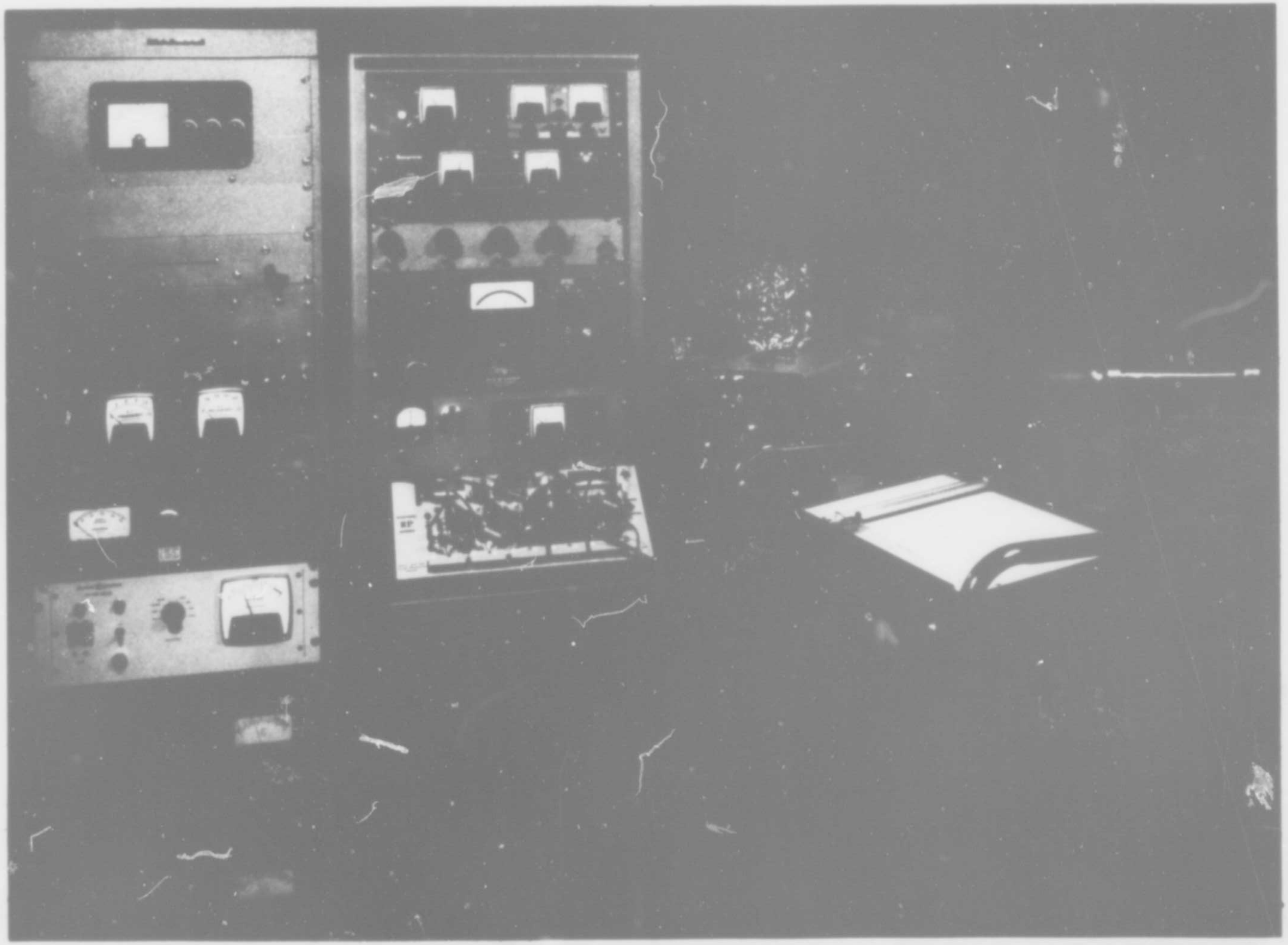

FIG. 2 THE APPARATUS AS SEEN BY THE EXPERIMENTER.

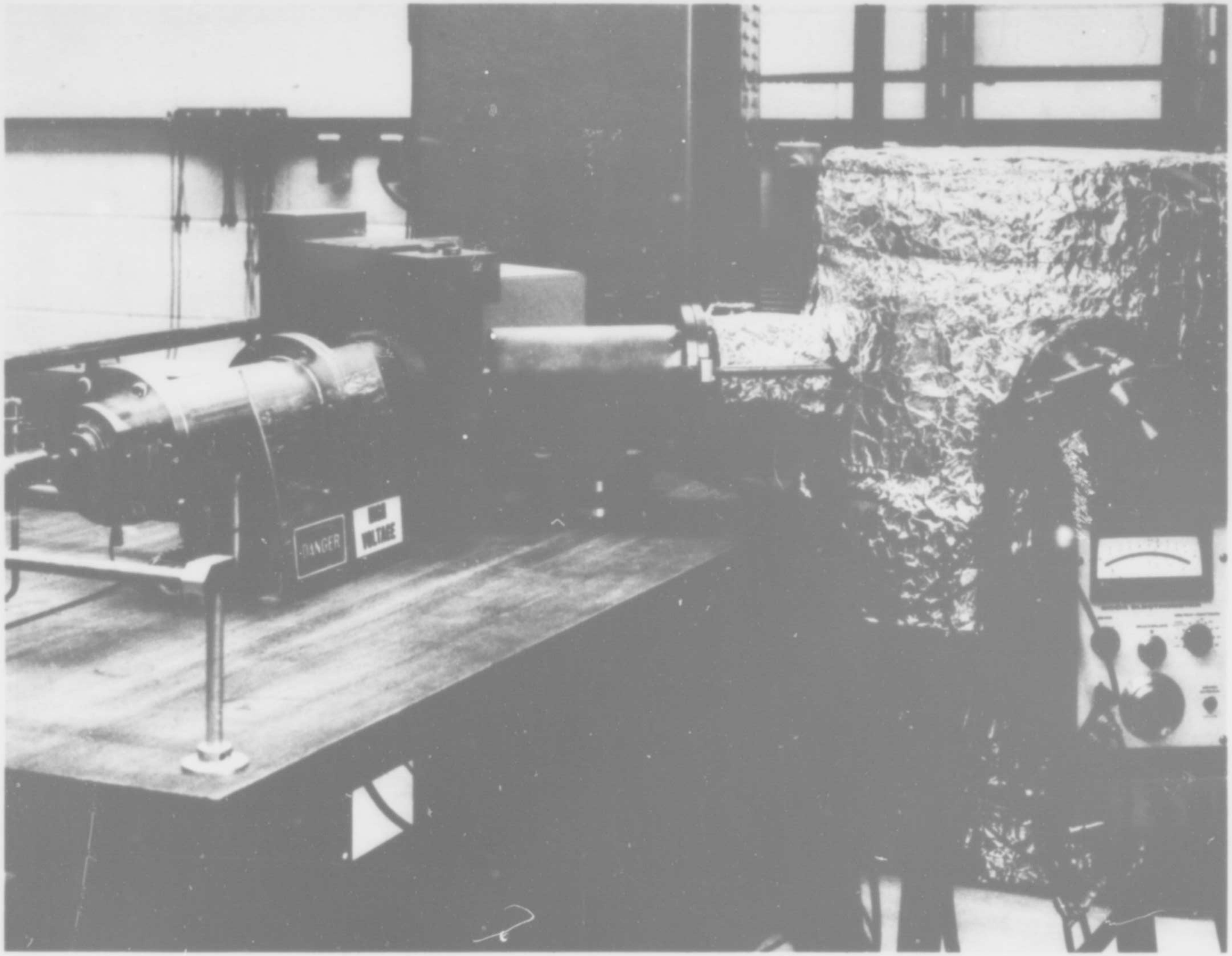

FIG. 3 AN ALTERNATE VIEW OF THE EXPERIMENTAL APPARATUS.

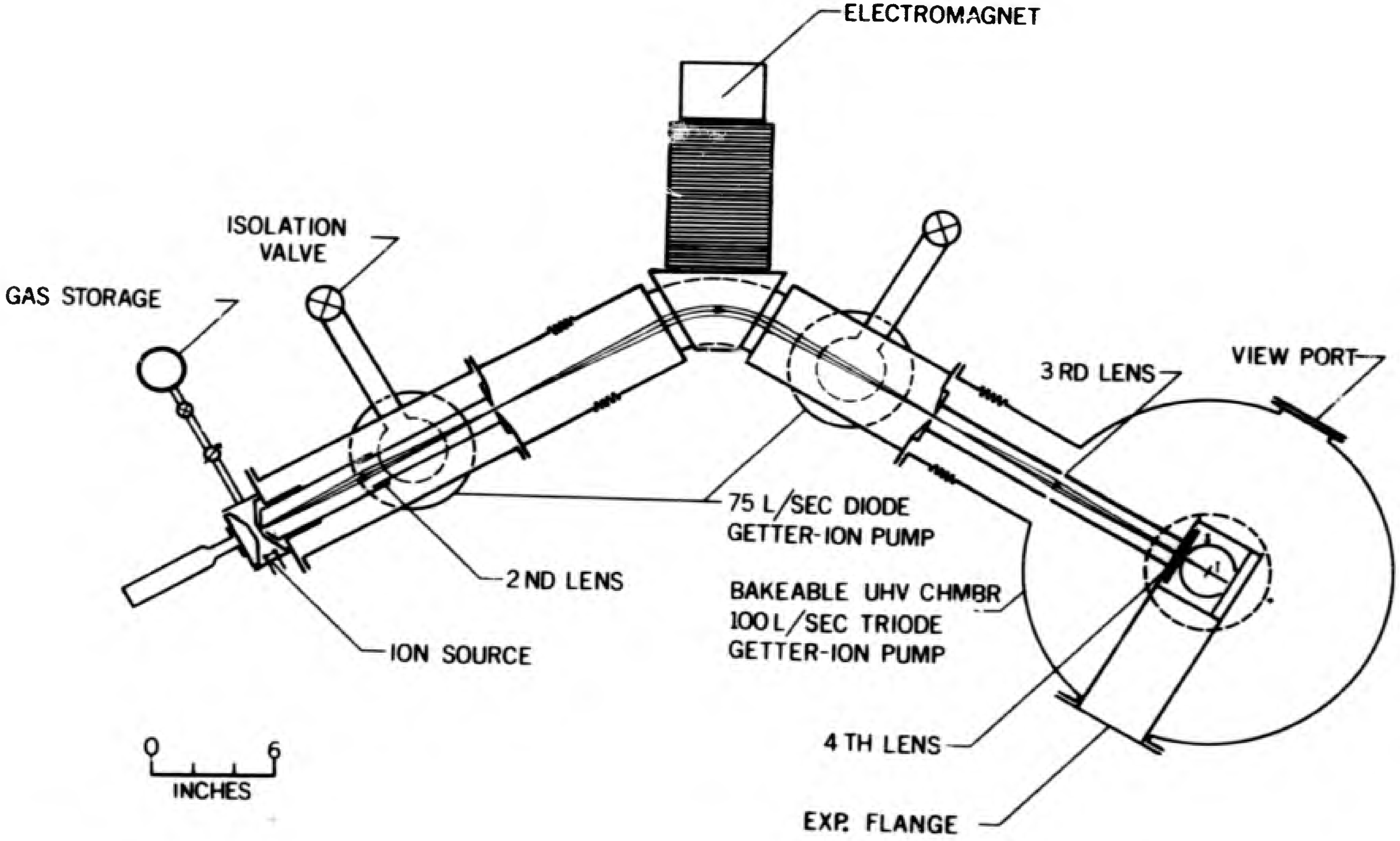

FIG. 4 A SCHEMATIC DIAGRAM OF THE APPARATUS

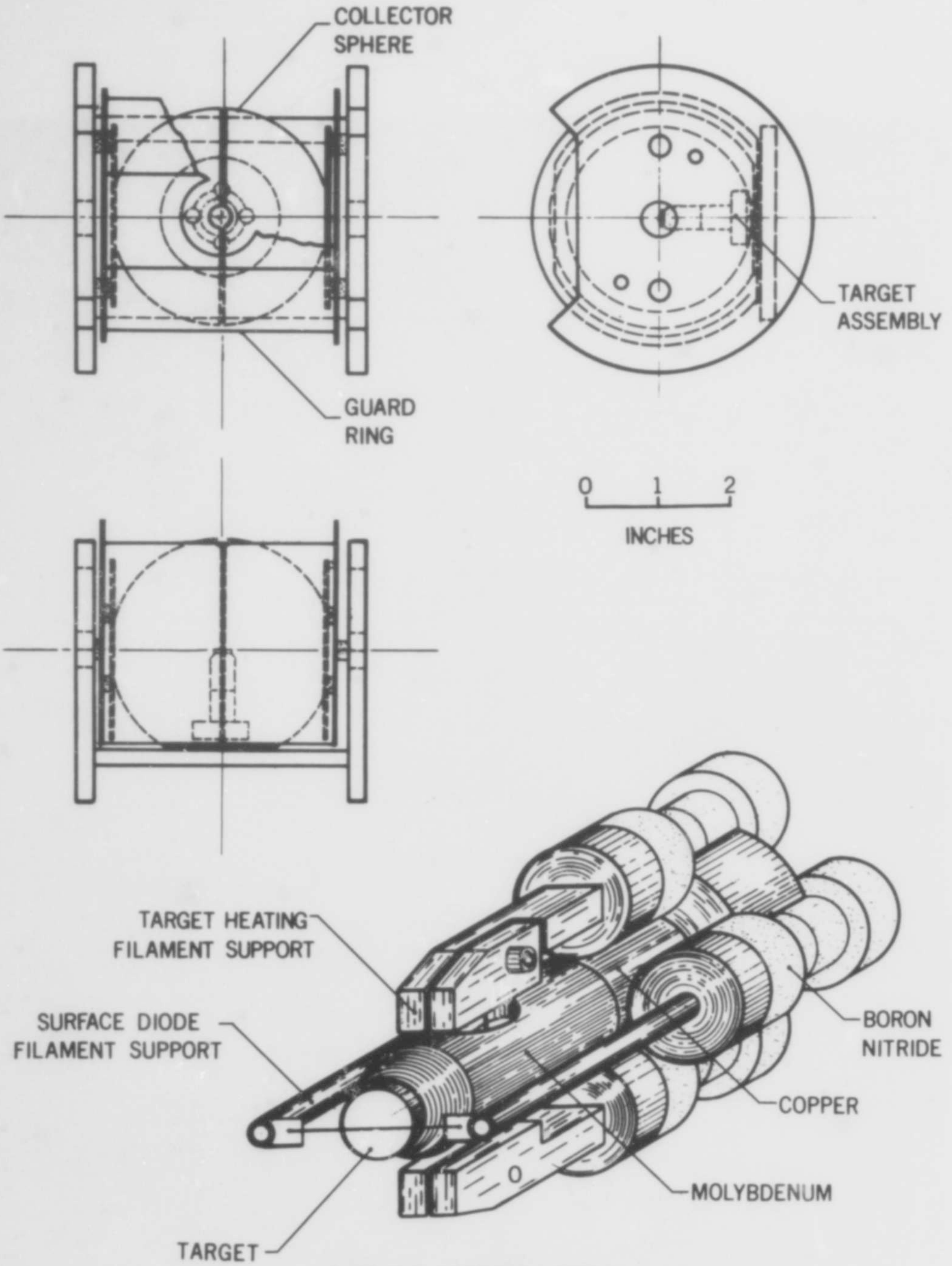

TARGET ASSEMBLY DETAIL

FIG. 5 INTERACTION ASSEMBLY DETAILS

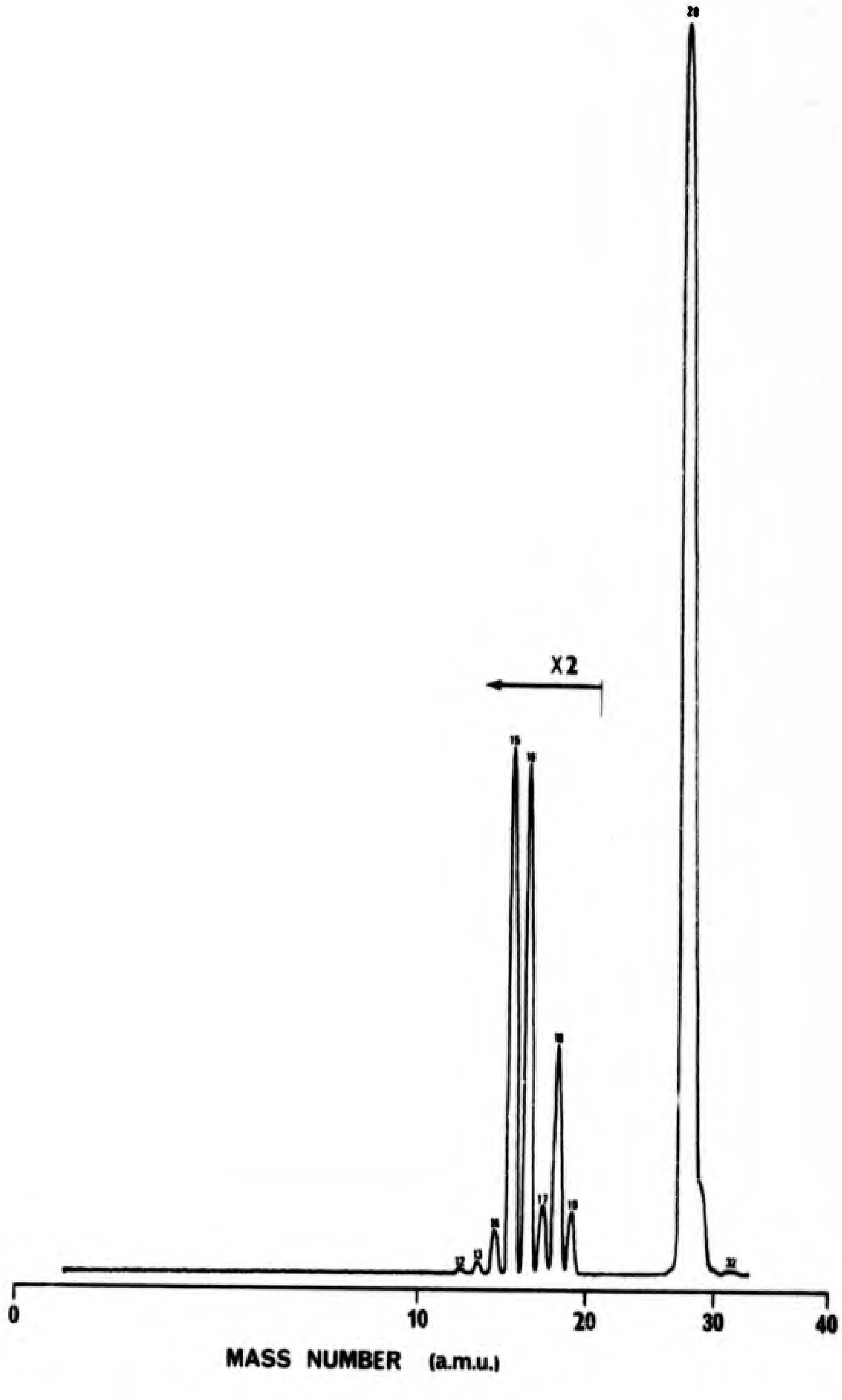

FIG. 6 ION SPECTRUM PRIOR TO MASS ANALYSIS, N_2 SOURCE

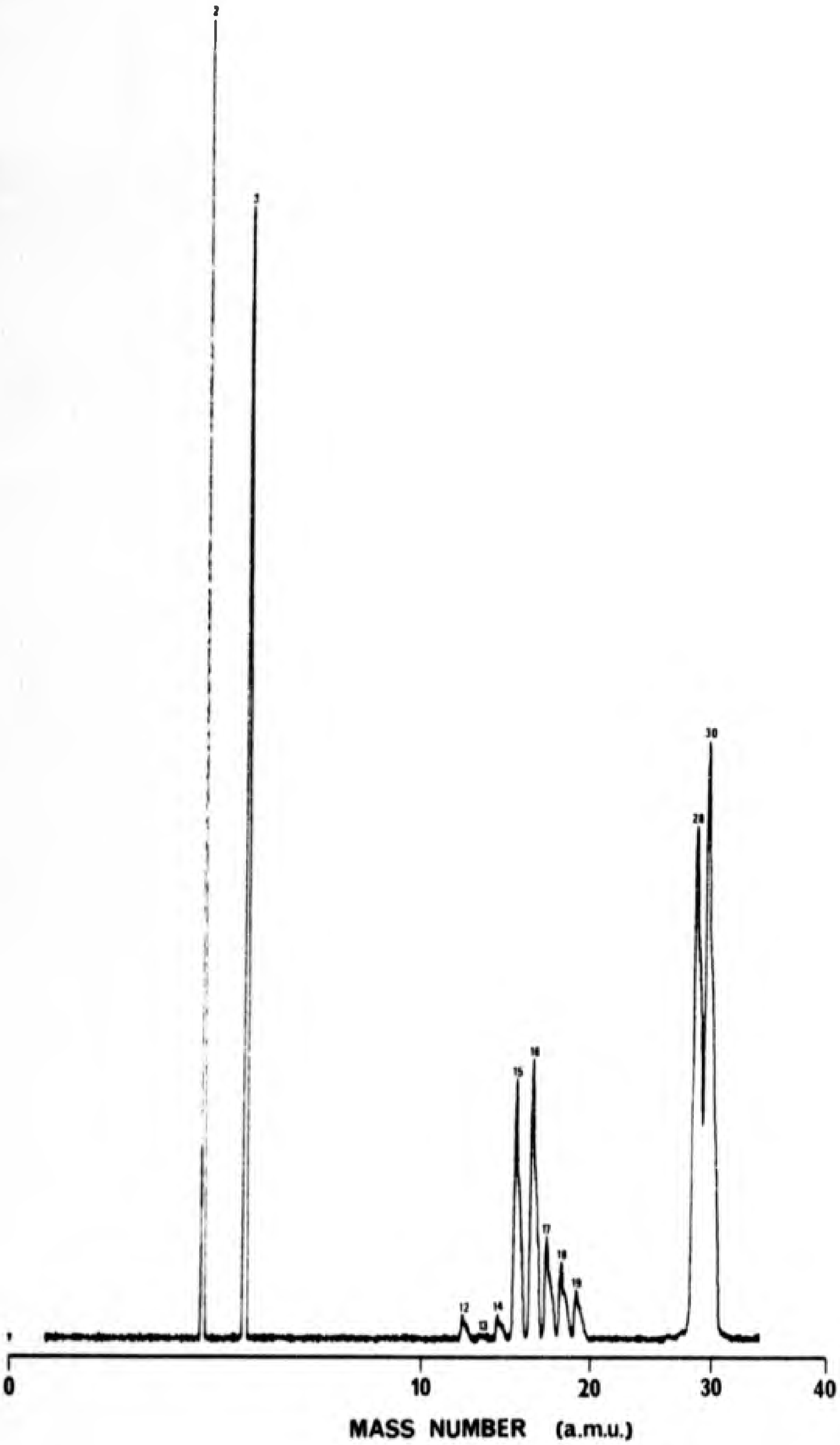

FIG. 7 ION SPECTRUM PRIOR TO MASS ANALYSIS, H_2 SOURCE

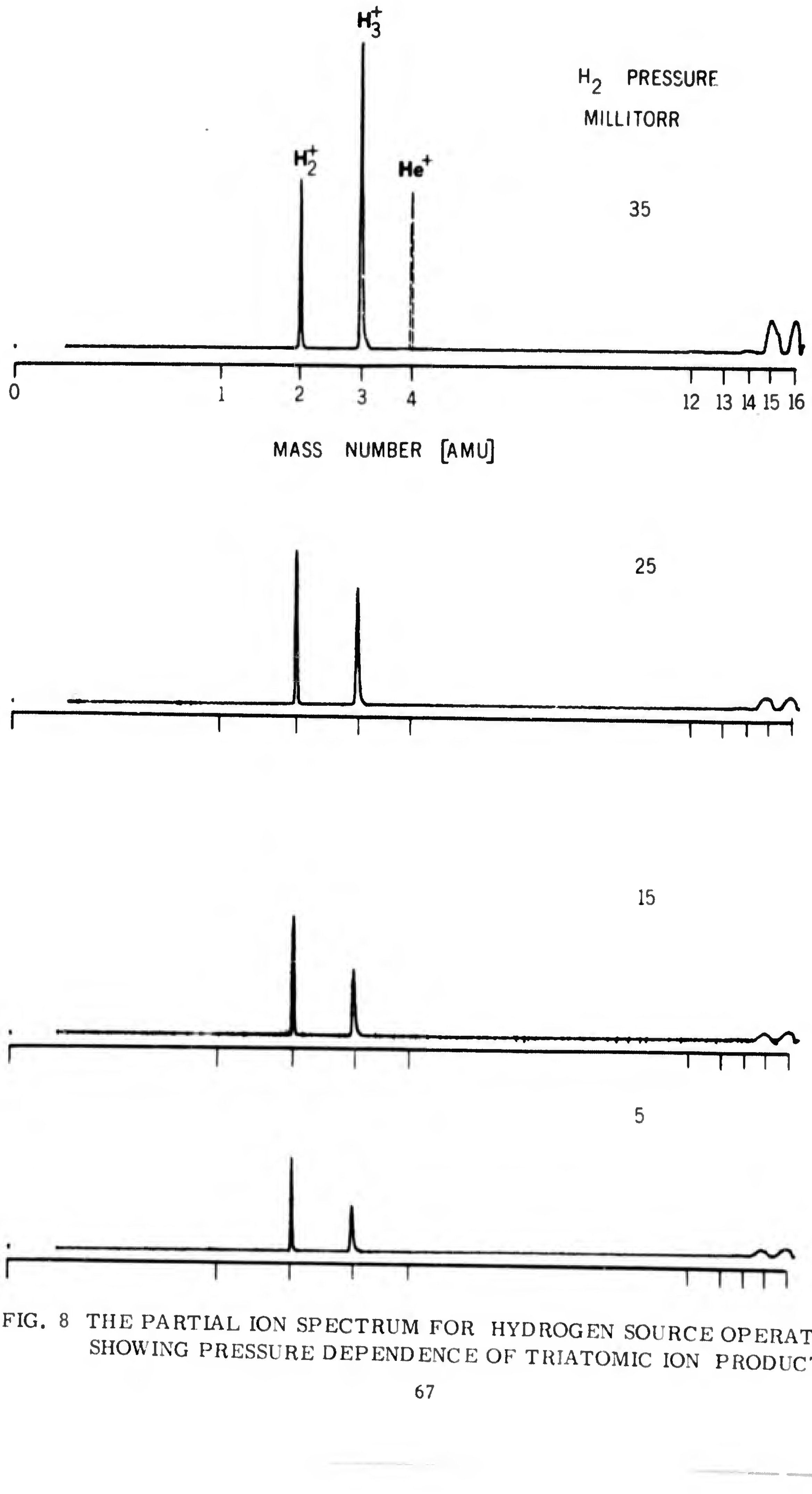

FIG. 8 THE PARTIAL ION SPECTRUM FOR HYDROGEN SOURCE OPERATION SHOWING PRESSURE DEPENDENCE OF TRIATOMIC ION PRODUCTION

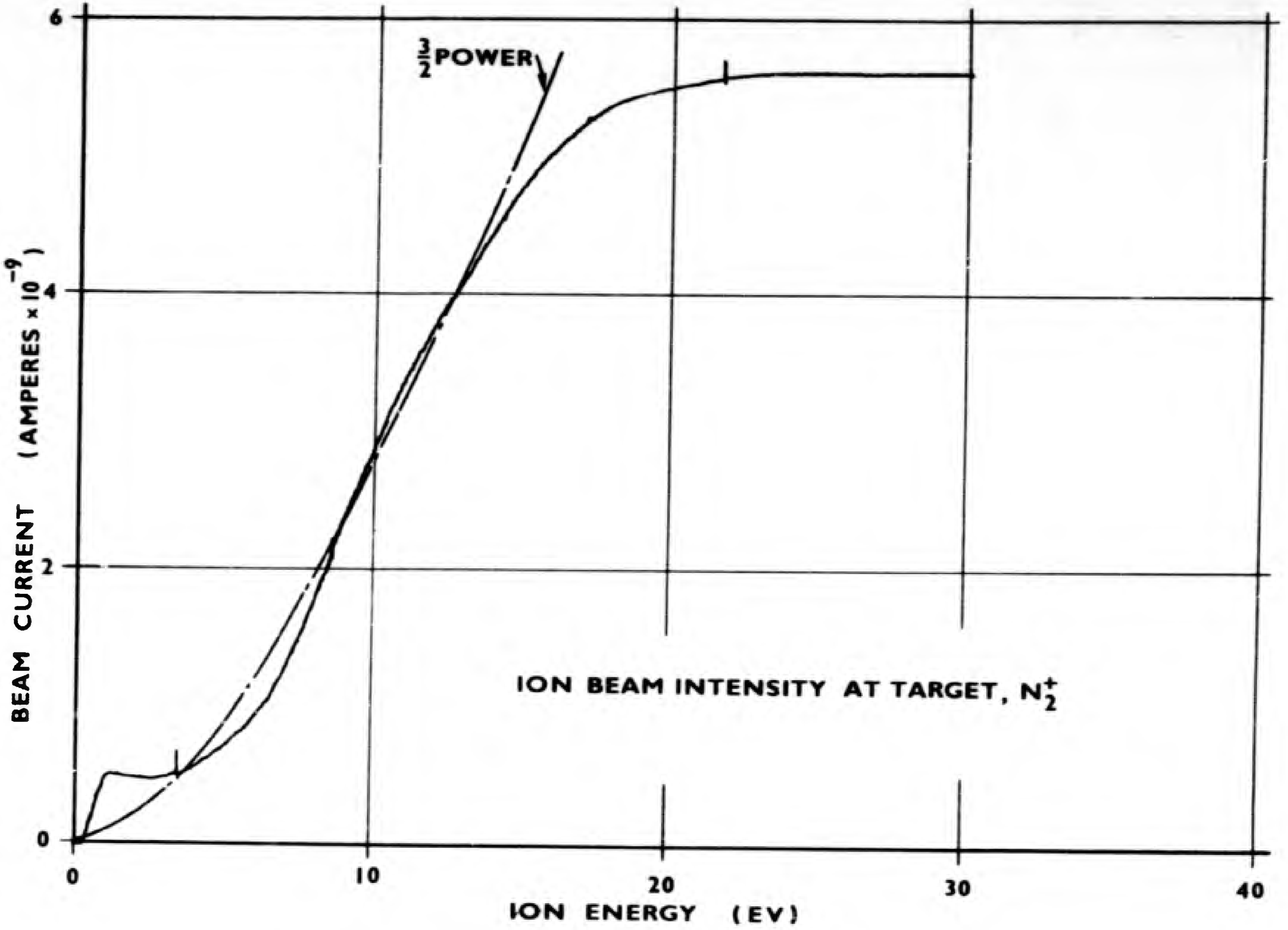

FIG. 9 ENERGY DEPENDENCE OF ION BEAM CURRENT AT FINAL FOCUS

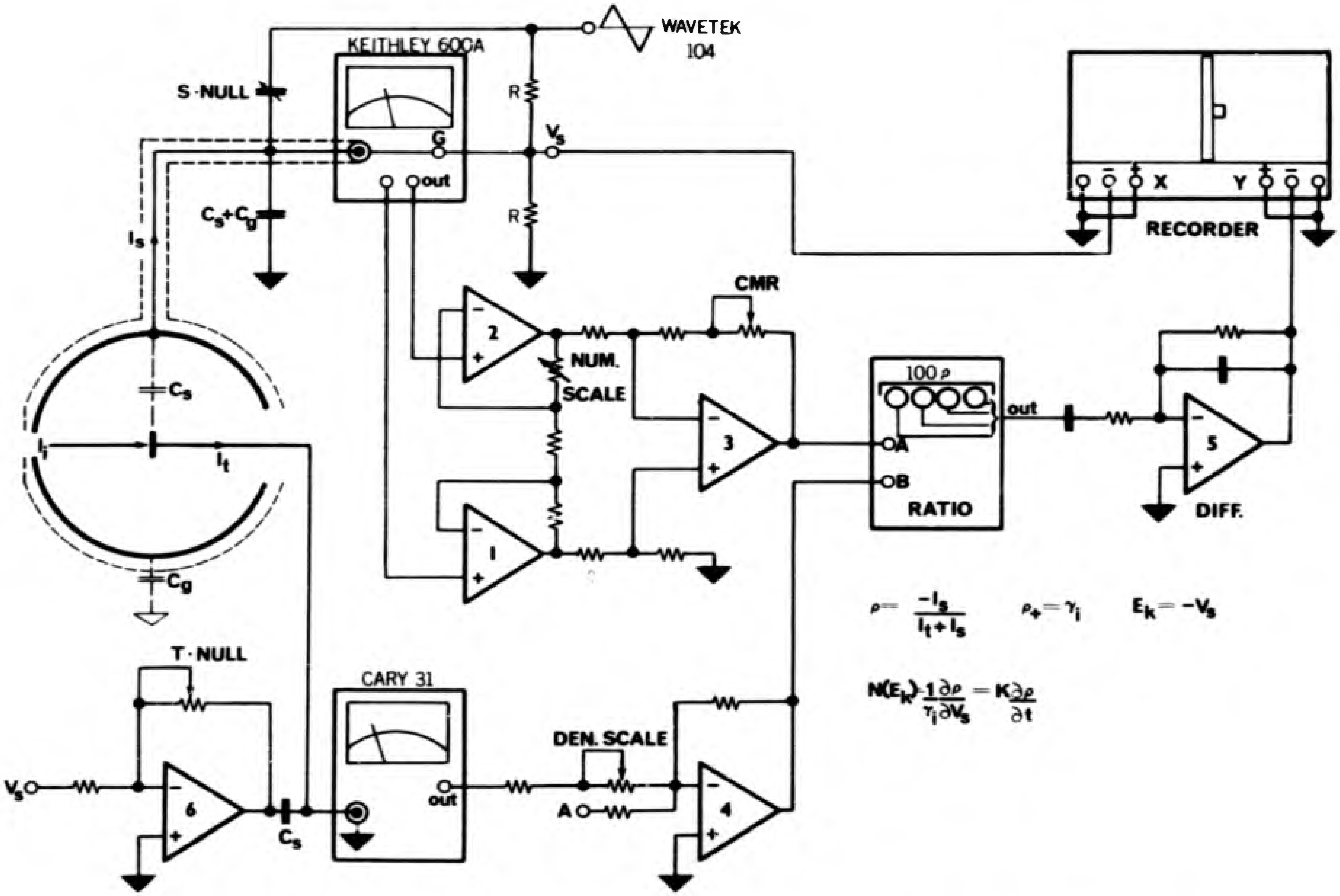

FIG 10 ANALOG CIRCUITRY TO OBTAIN NORMALIZED SECONDARY-ELECTRON ENERGY DISTRIBUTIONS

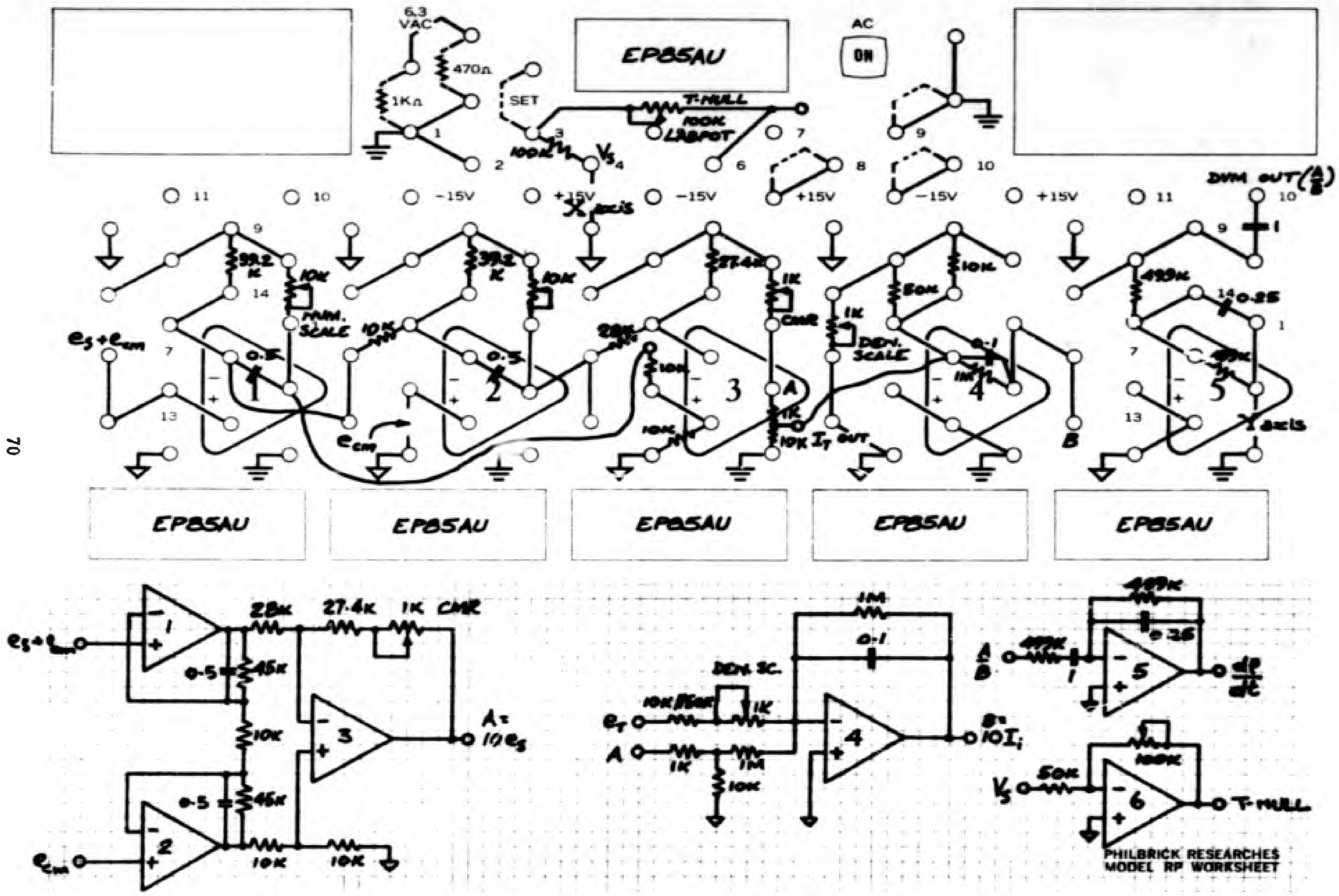

FIG. 11 ANALOG NETWORK SHOWING TYPICAL COMPONENT VALUES.

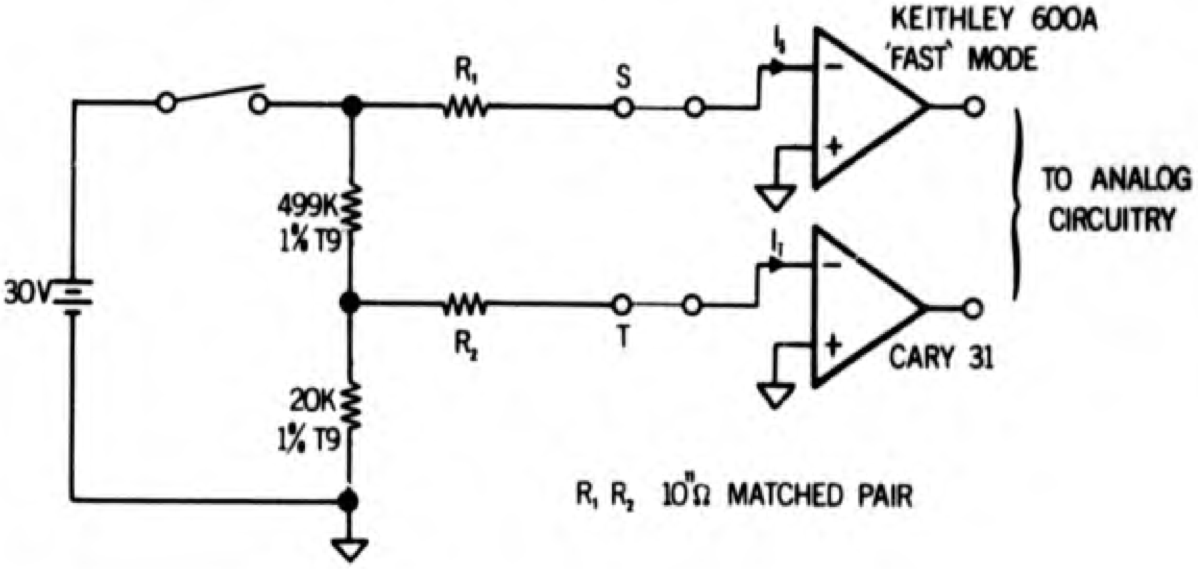

CIRCUIT A

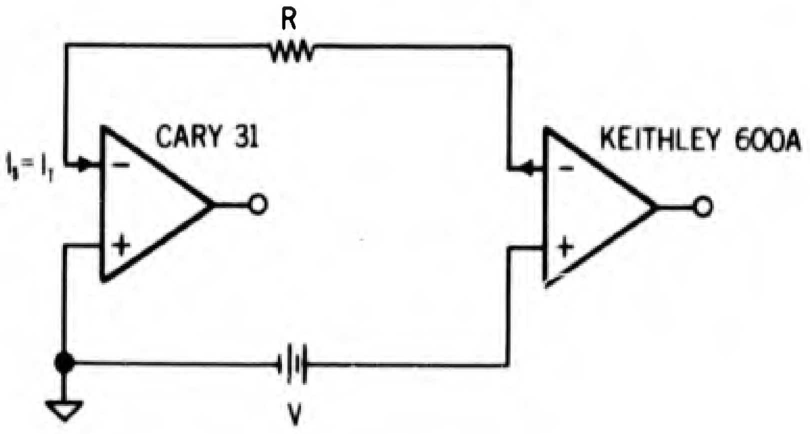

CIRCUIT B

FIG. 12 CALIBRATION CIRCUITS

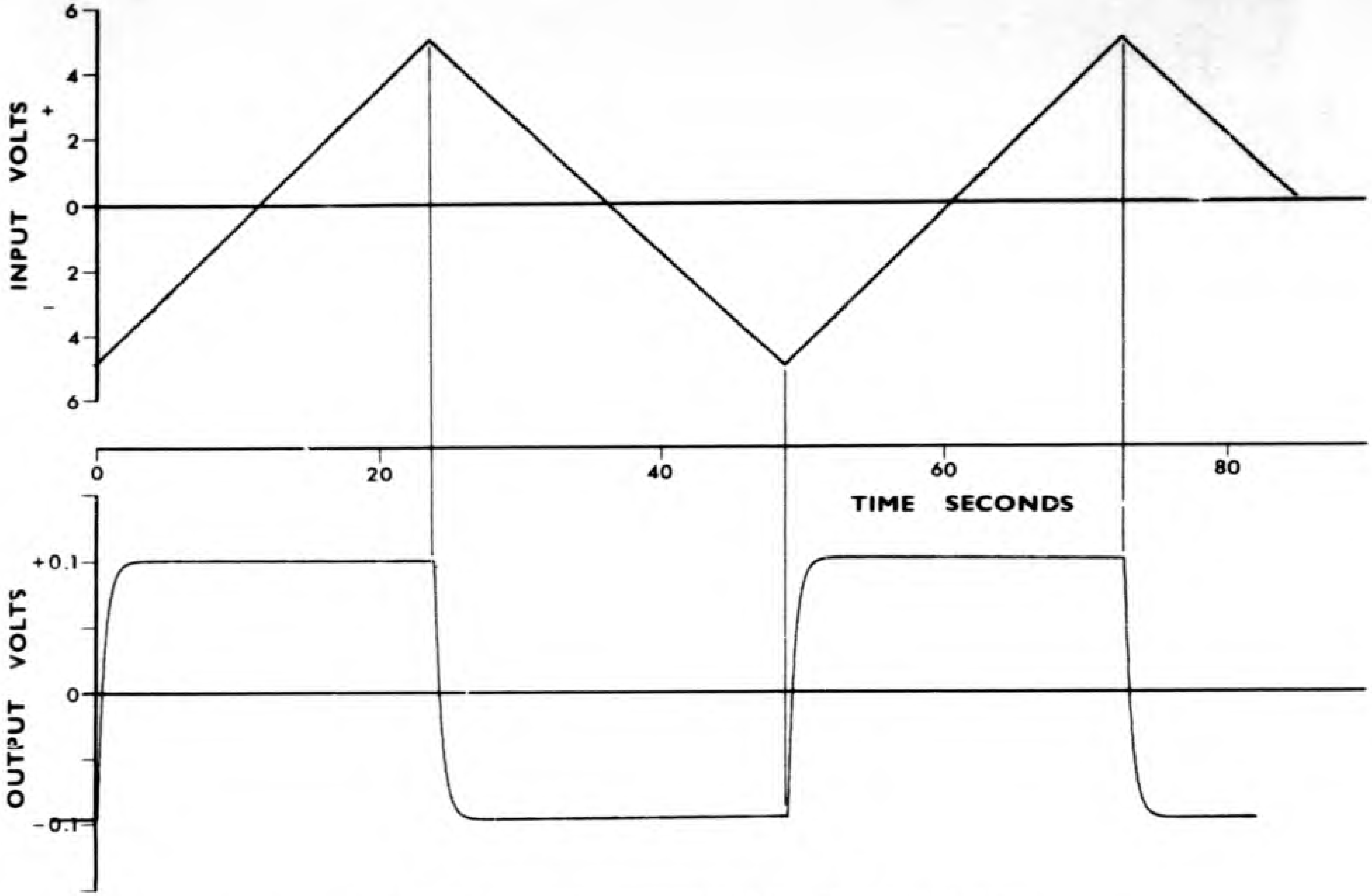

FIG. 13 LINEAR SWEEP AND DIFFERENTIATOR WAVEFORMS

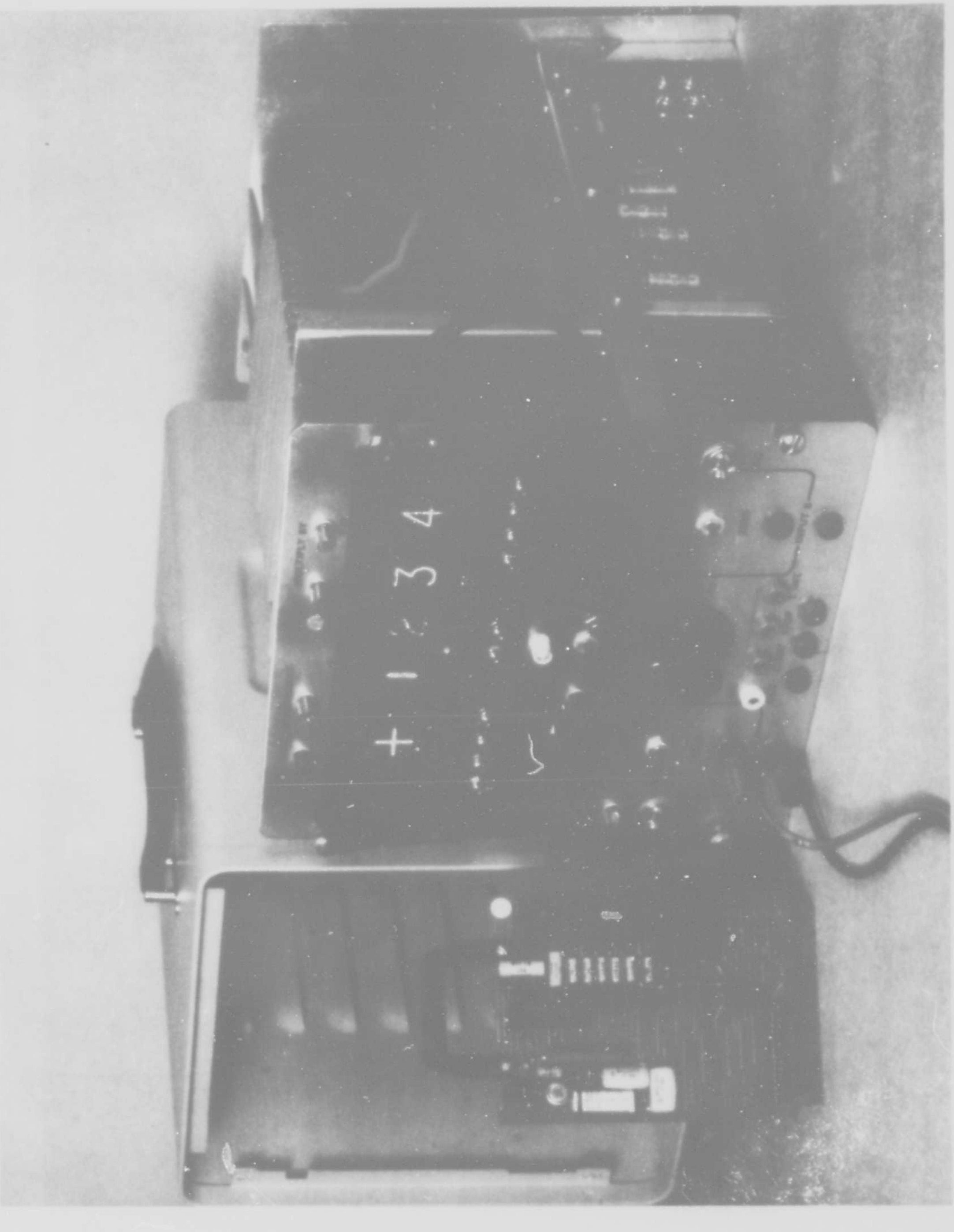

FIG. 14 A VIEW OF THE DVM/RATIOMETER.

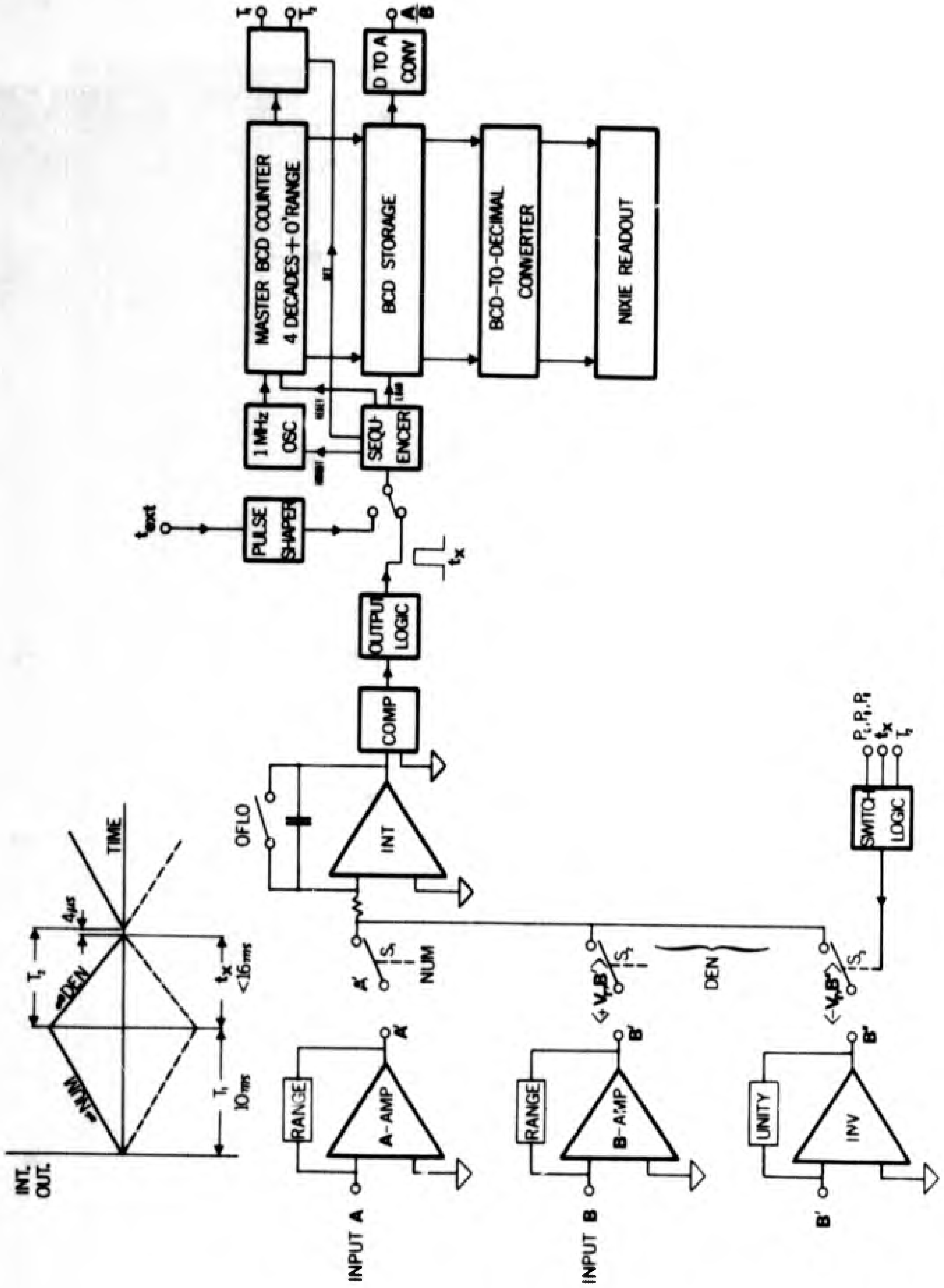

FIG. 15 DVM/RATIOMETER, OPERATIONAL SCHEMATIC

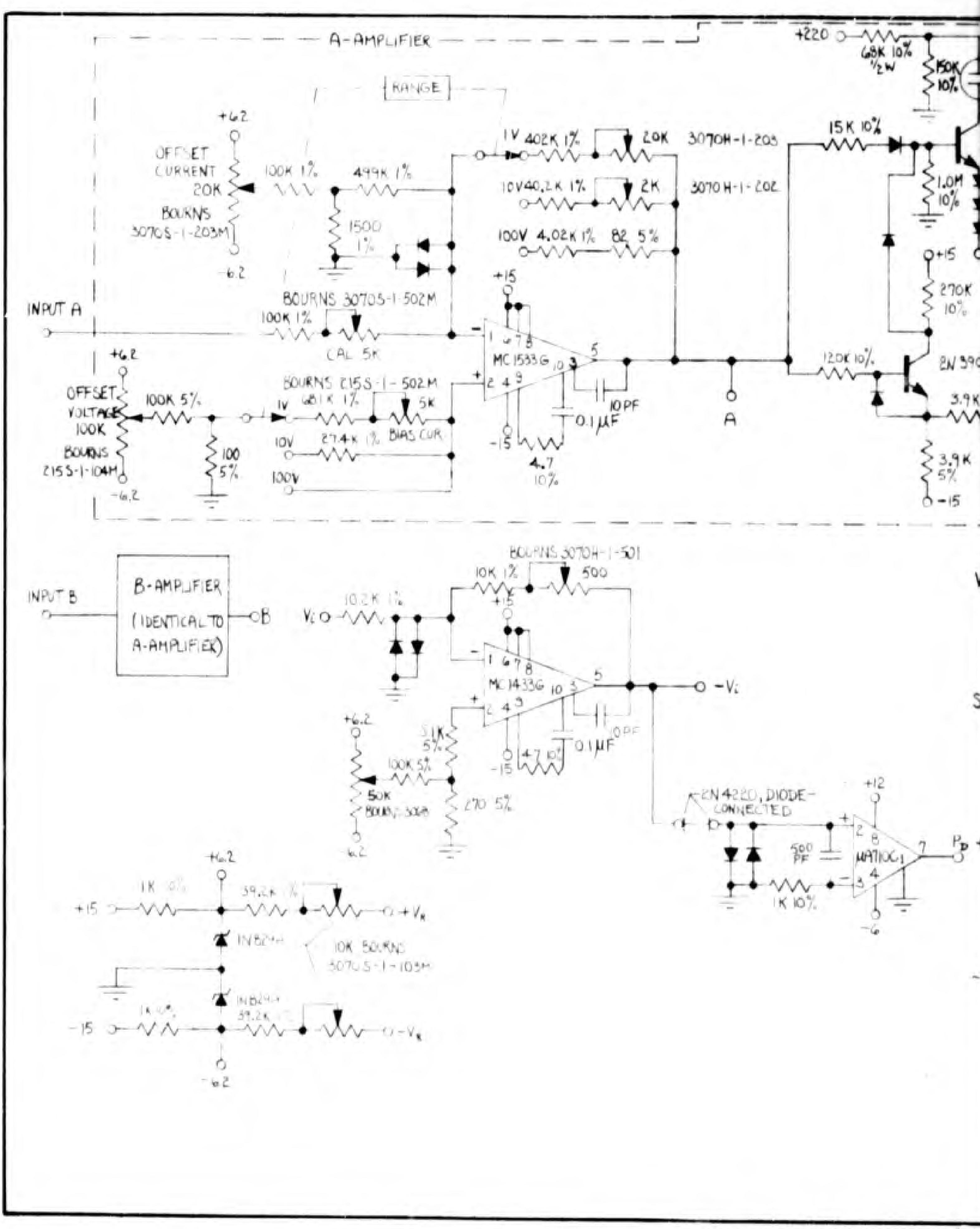

FIG. 16 DIGITAL VOLTMETER/RA

A

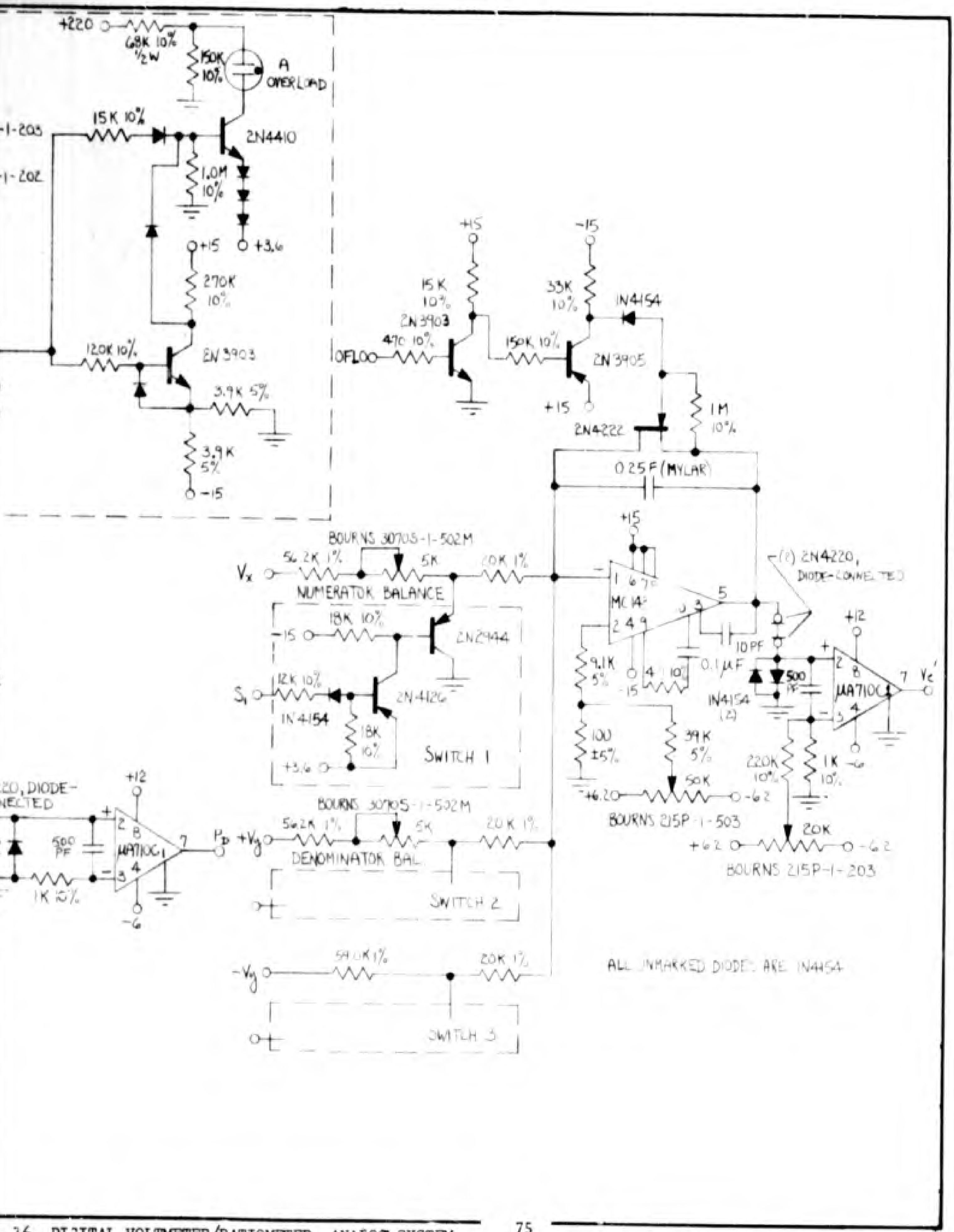

16 DIGITAL VOLTMETER/RATIOMETER, ANALOG SYSTEM

B

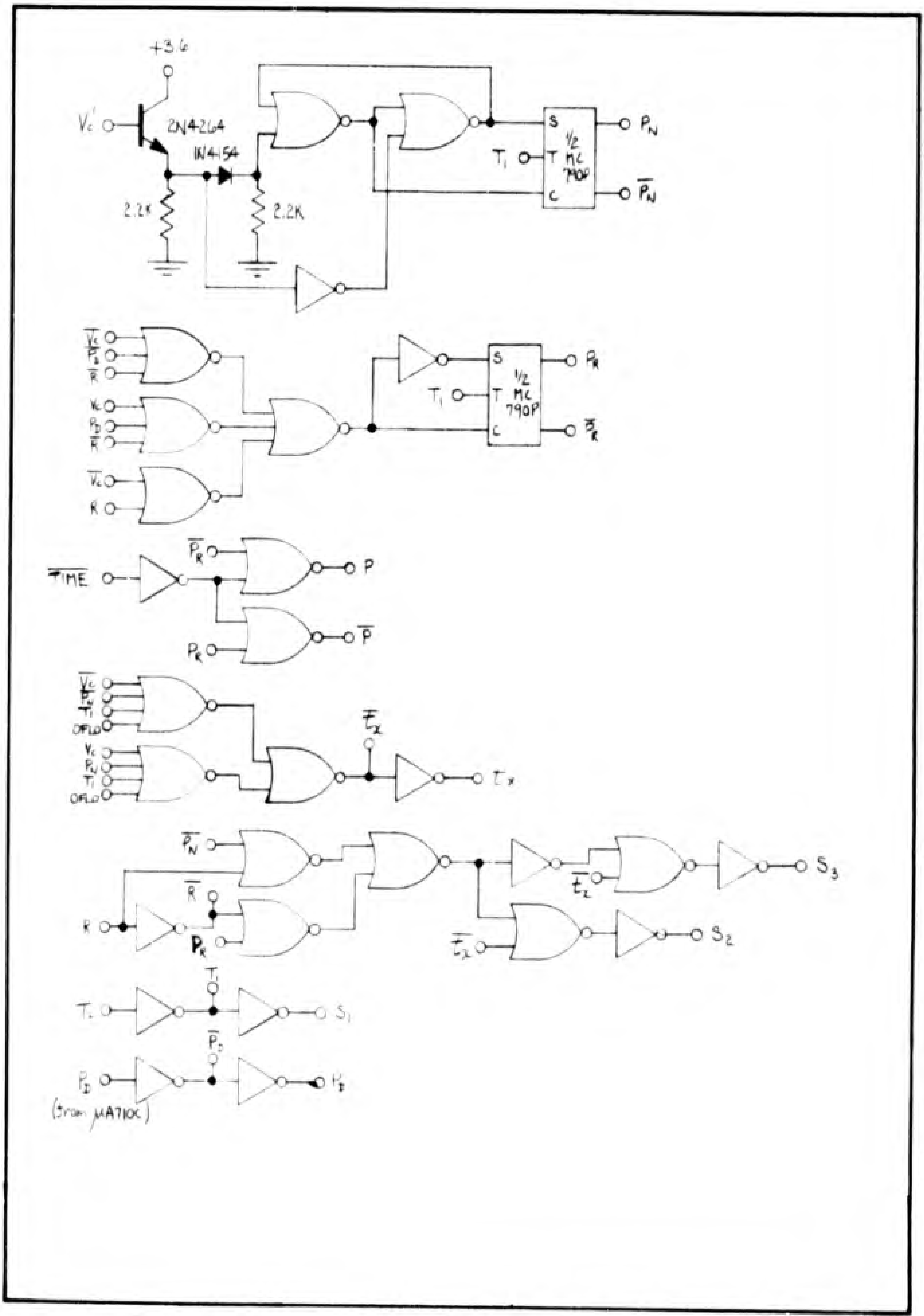

FIG. 17 DIGITAL VOLTMETER/RATIOMETER, ANALOG SYSTEM CONTROL LOGIC

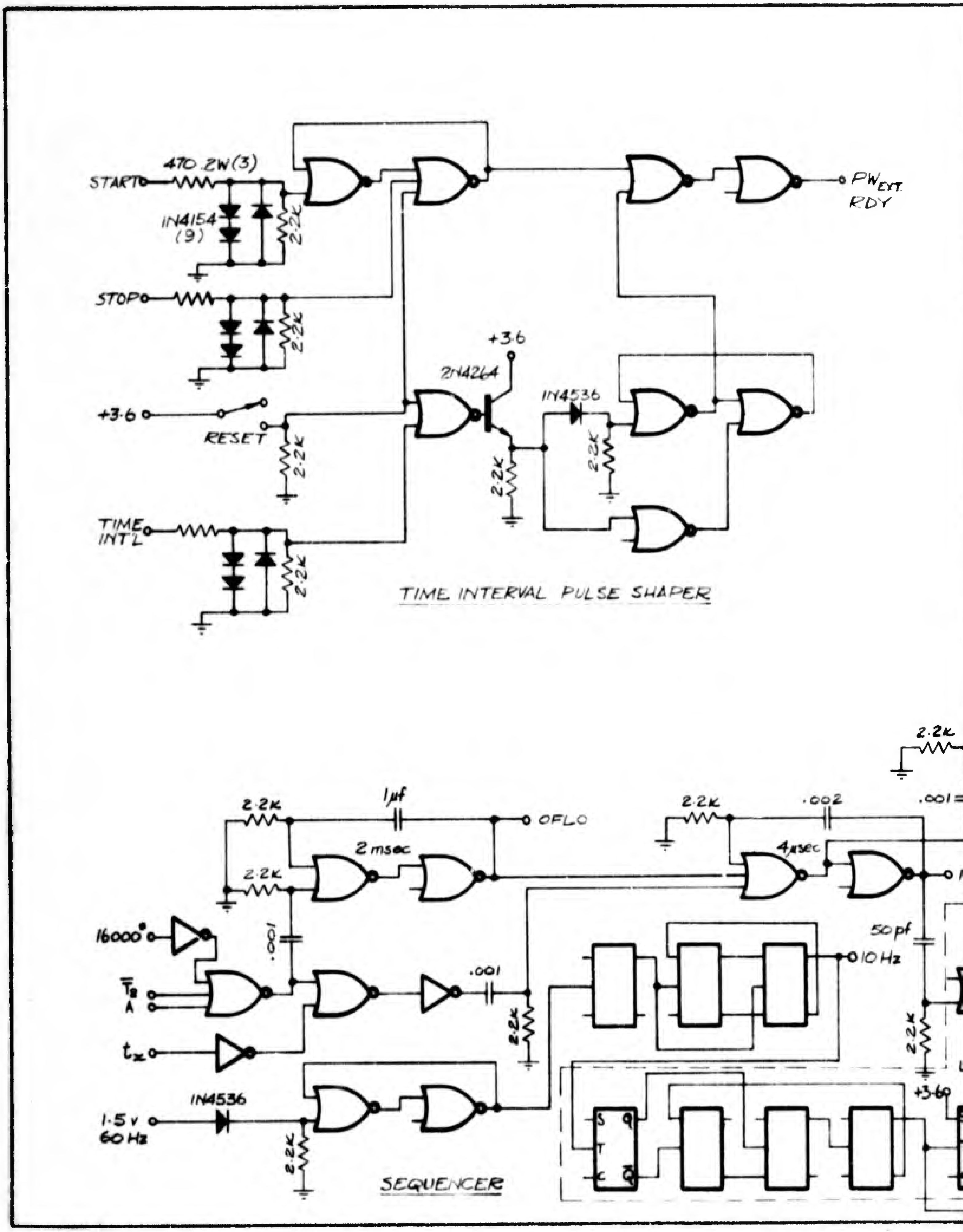

FIG. 18 DIGITAL VOLTMETER/

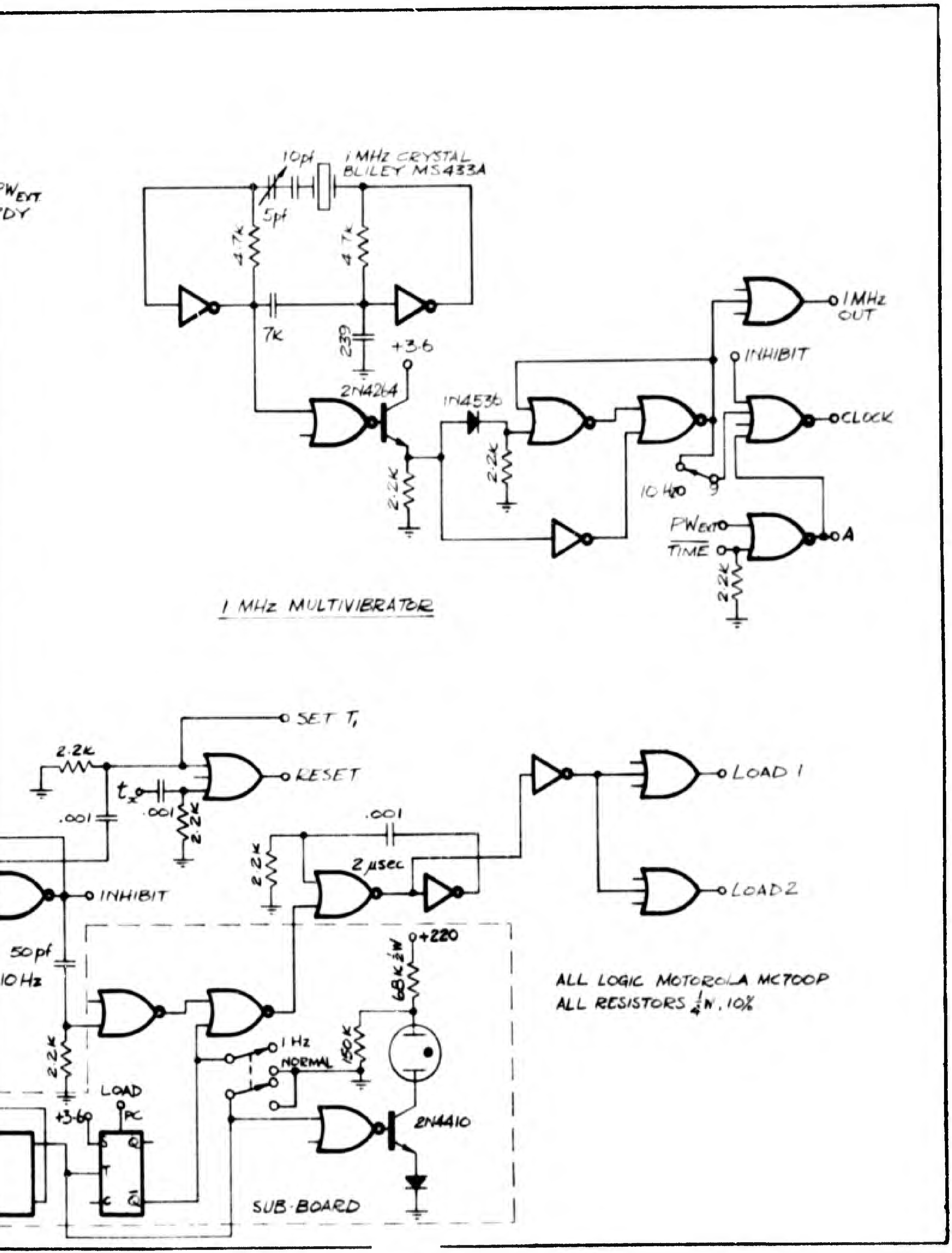

L VOLTMETER/RATIOMETER, DIGITAL LOGIC

B

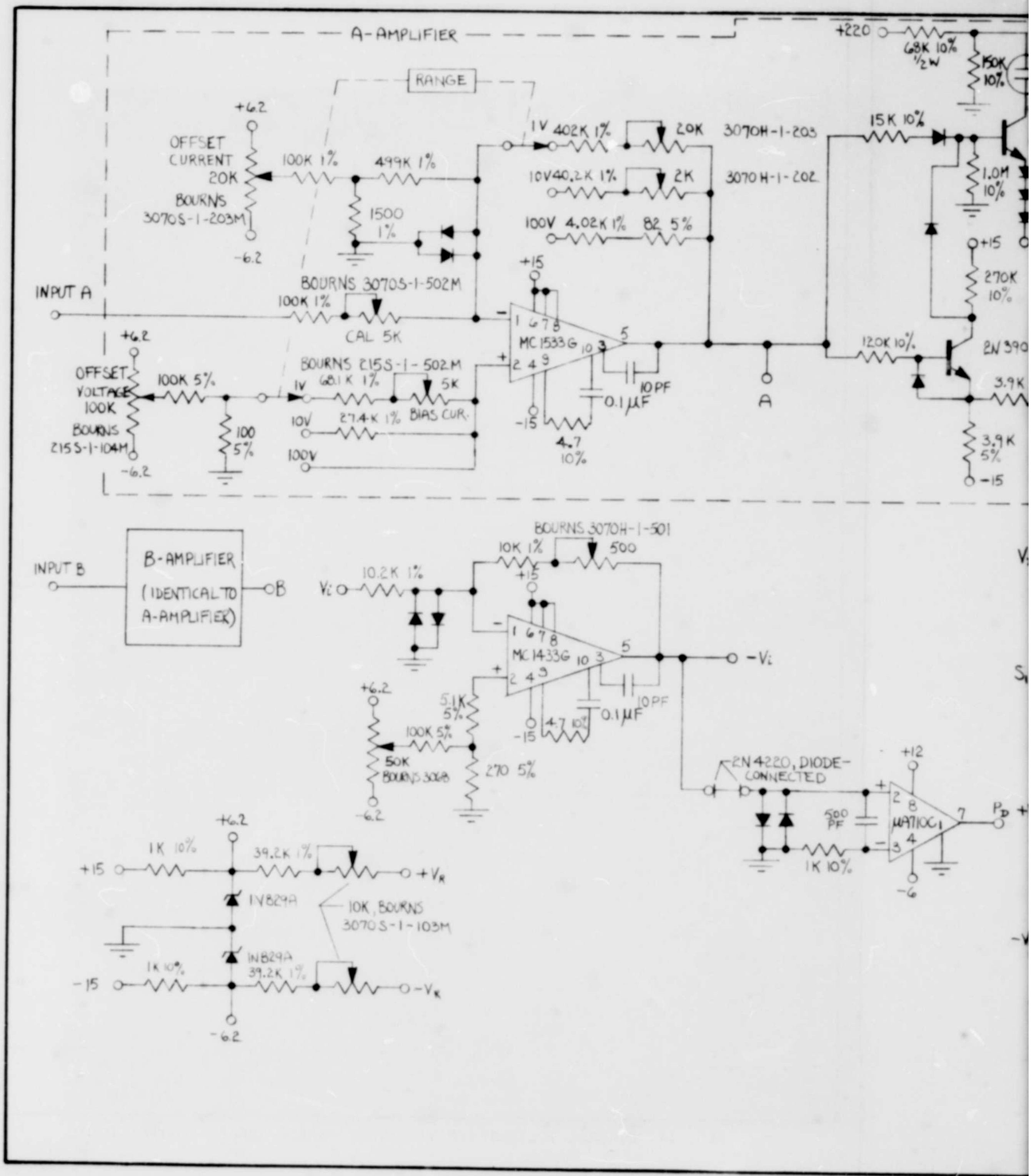

FIG. 16 DIGITAL VOLTMETER/RAT

A

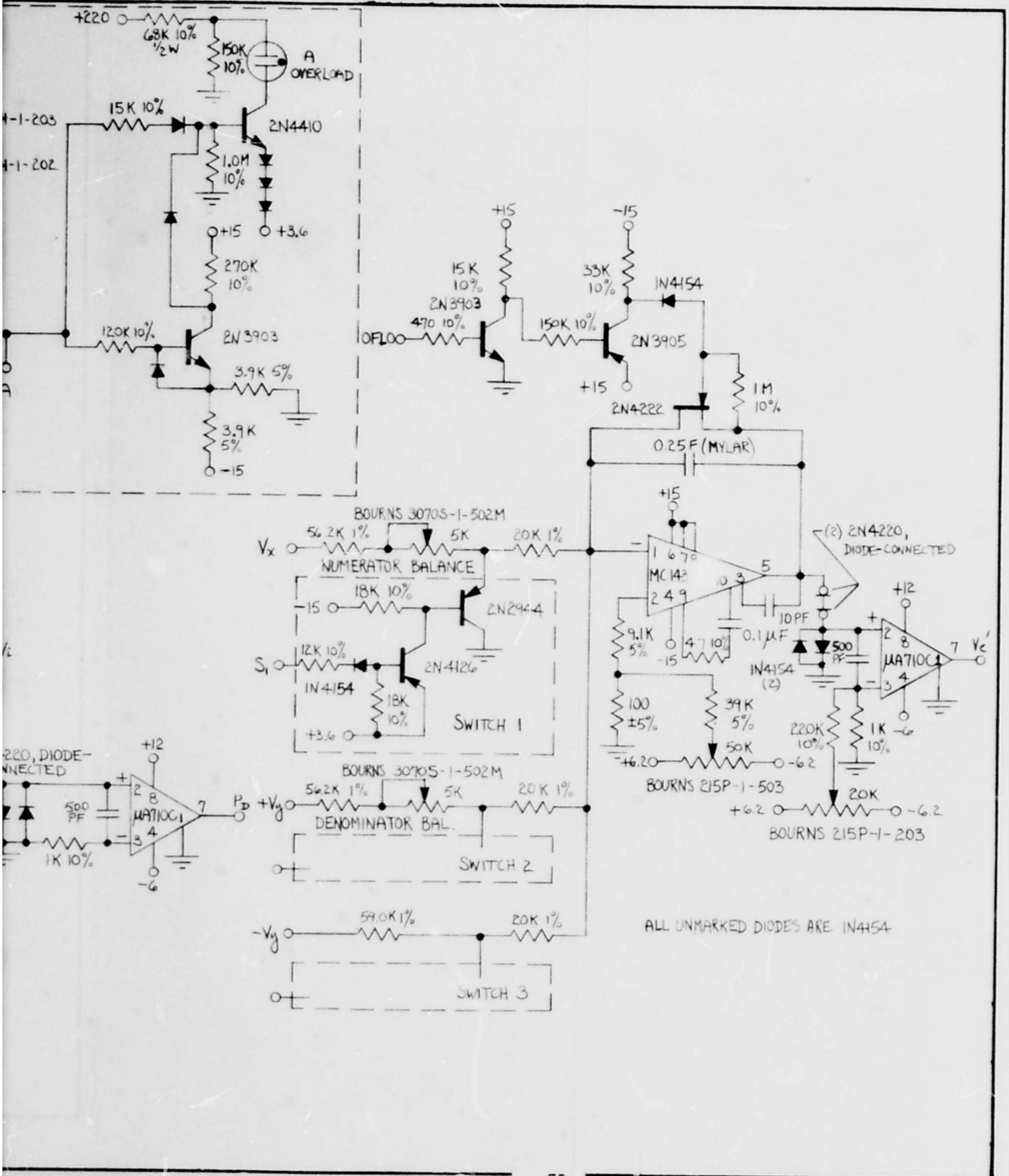

. 16 DIGITAL VOLTMETER/RATIOMETER, ANALOG SYSTEM

B

BLANK PAGE

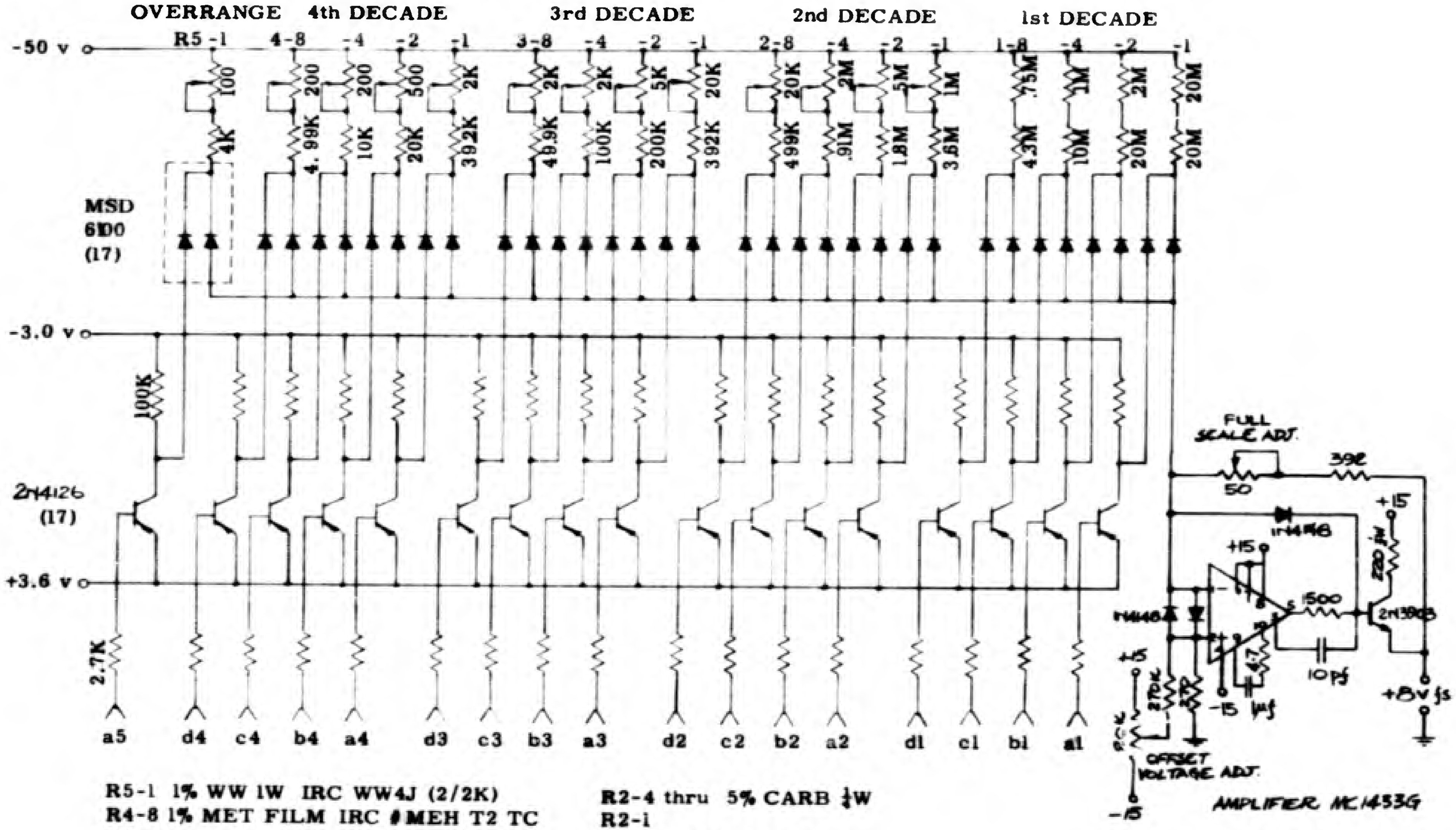

R5-1 1% WW 1W IRC WW4J (2/2K)
R4-8 1% MET FILM IRC #MEH T2 TC
R4-4 MEC
R4-2 MEB
R4-1 thru MEA
R2-8
BOURNS 3007 TRIM

R2-4 thru 5% CARB ¼W
R2-1
BOURNS 3068 TRIM

R1-8 thru 5% CARB ¼W
R1-1

FIG. 20 DIGITAL VOLTMETER/RATIOMETER, DIGITAL-TO-ANALOG CONVERTER

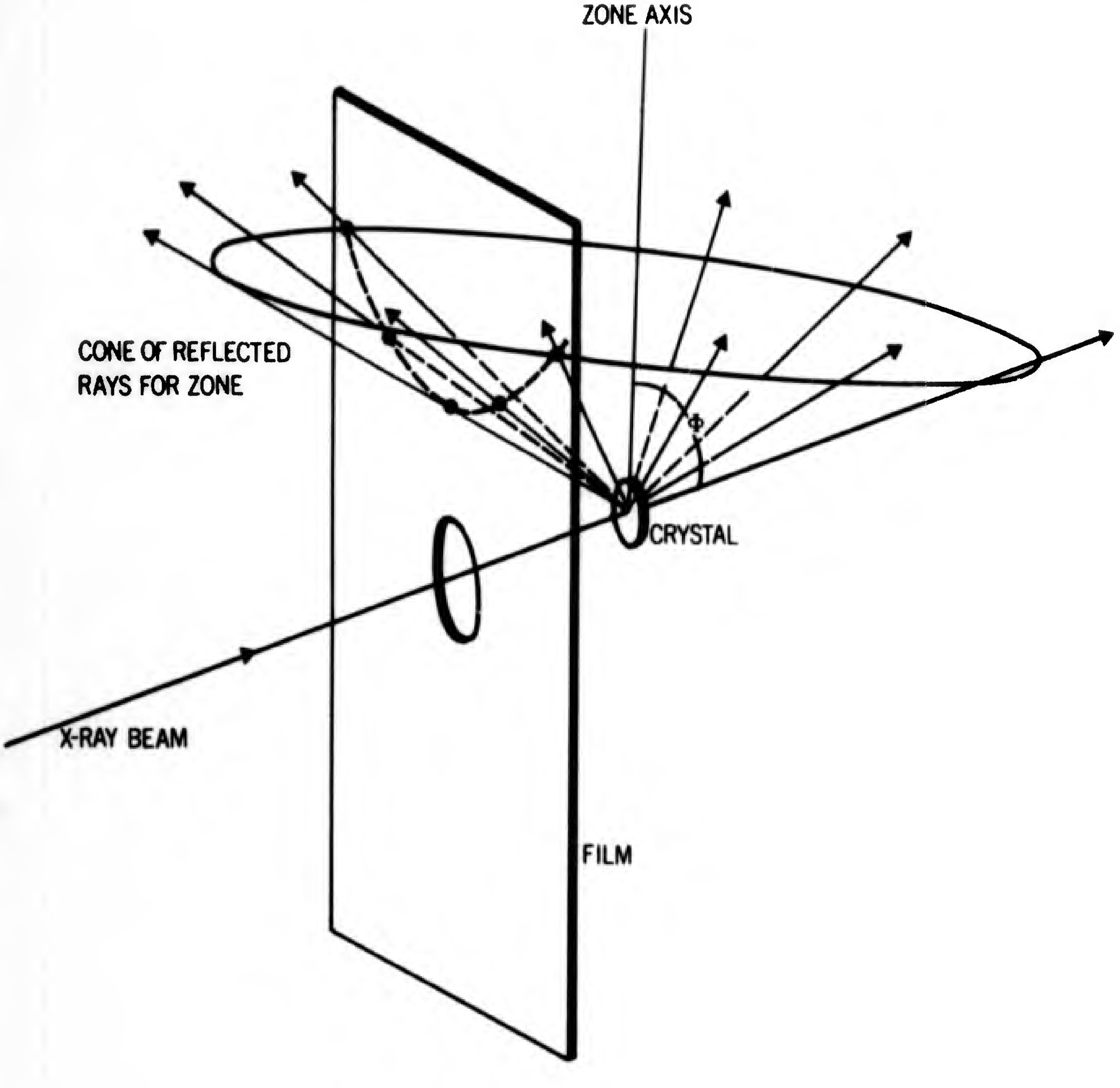

FIG. 21 BACK-REFLECTION LAUE PATTERN OF PLANES OF A ZONE IN A CRYSTAL

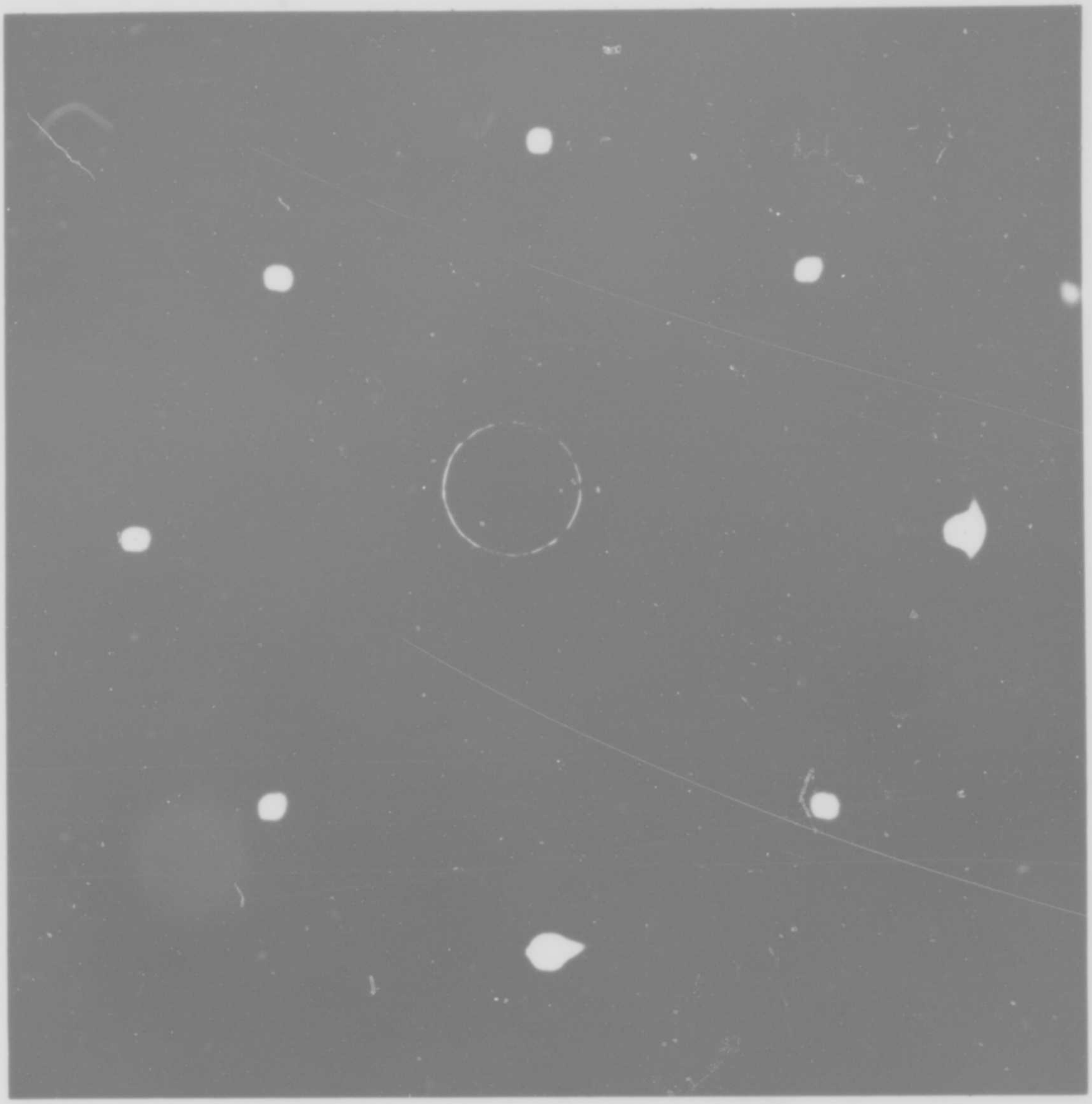

FIG. 22 LAUE BACK-DIFFRACTION PATTERN FOR ANNEALED (100) TUNGSTEN SURFACE.

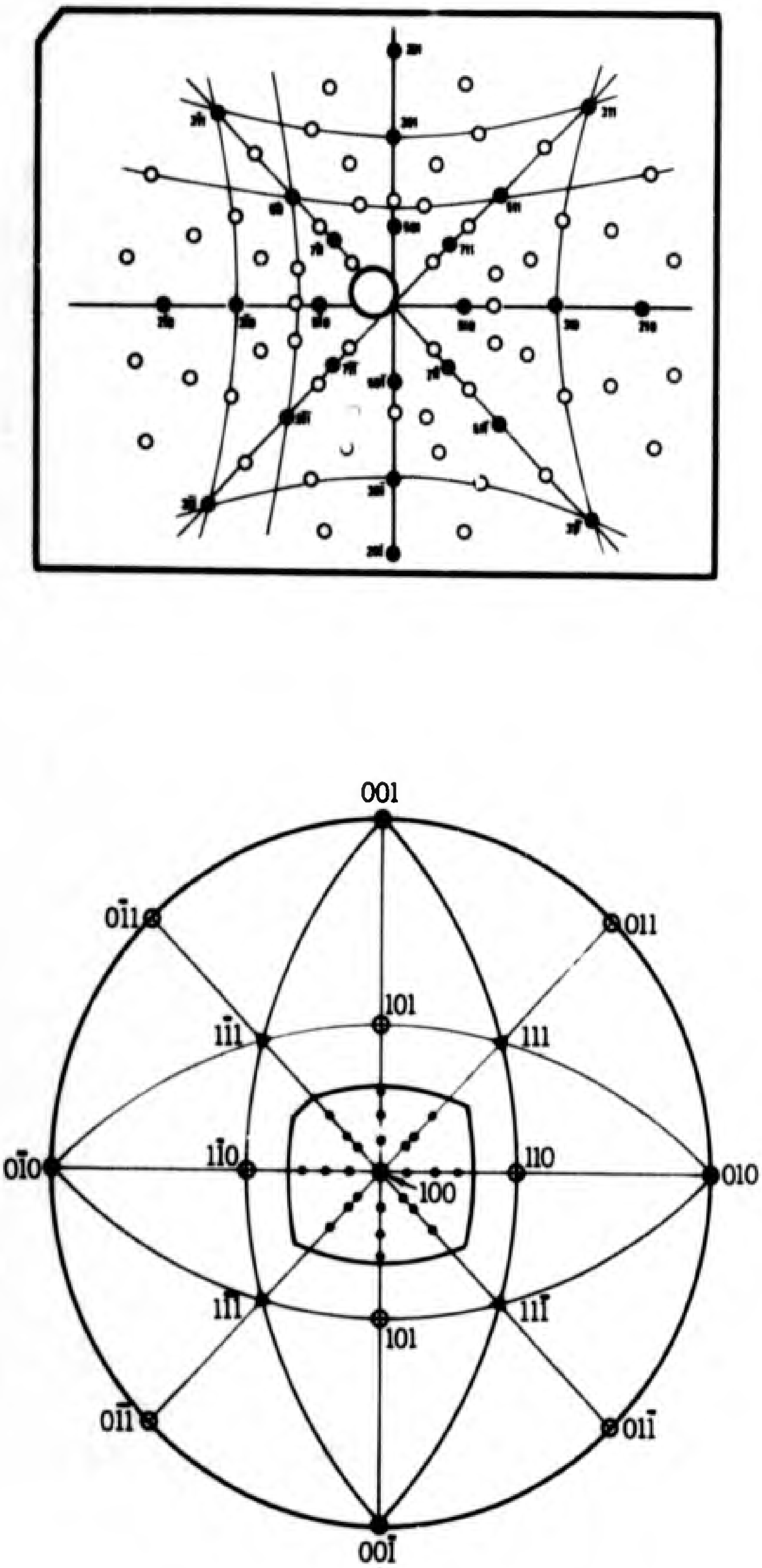

FIG. 23 A REPRODUCTION OF THE (100) TUNGSTEN LAUE PATTERN (UPPER) AND ITS STANDARD STEREOSCOPIC PROJECTION LOWER), IDENTIFYING PRINCIPAL POLES

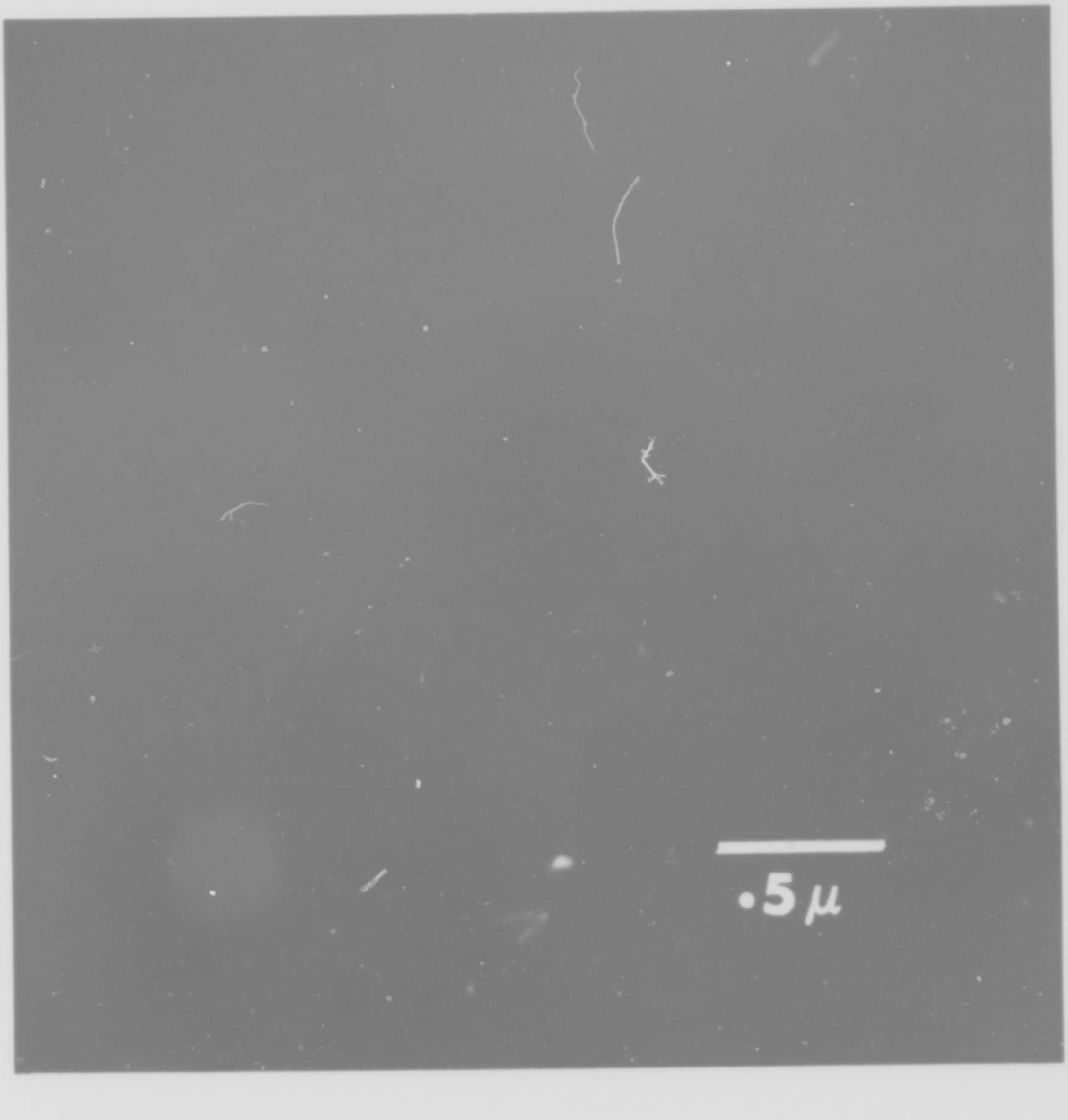

FIG. 24 ELECTRON MICROGRAPH OF THE ANNEALED (100) TUNGSTEN SURFACE.

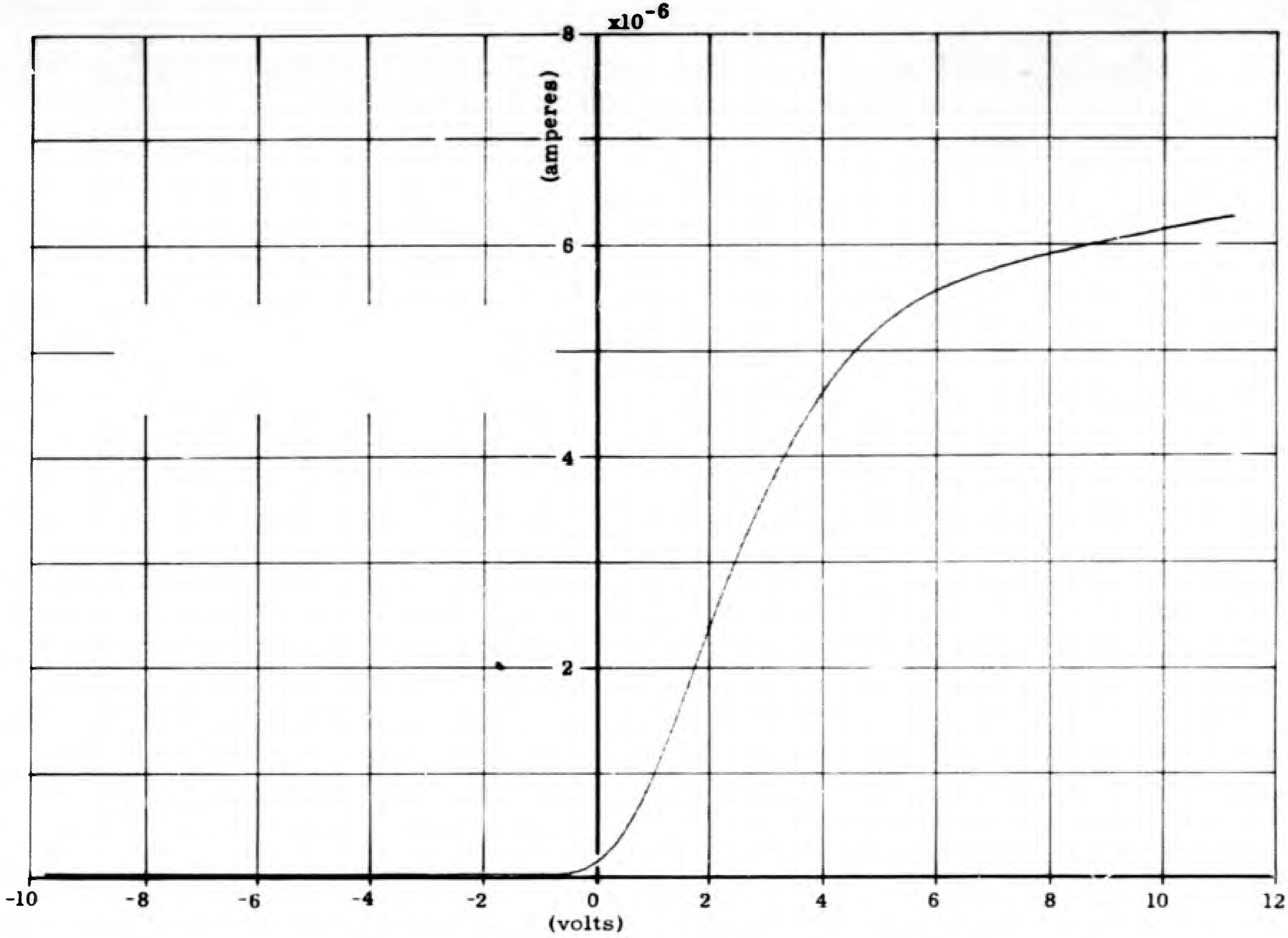

FIG. 25 A TYPICAL RETARDING-FIELD-DIODE CHARACTERISTIC IN ITS ENTIRETY

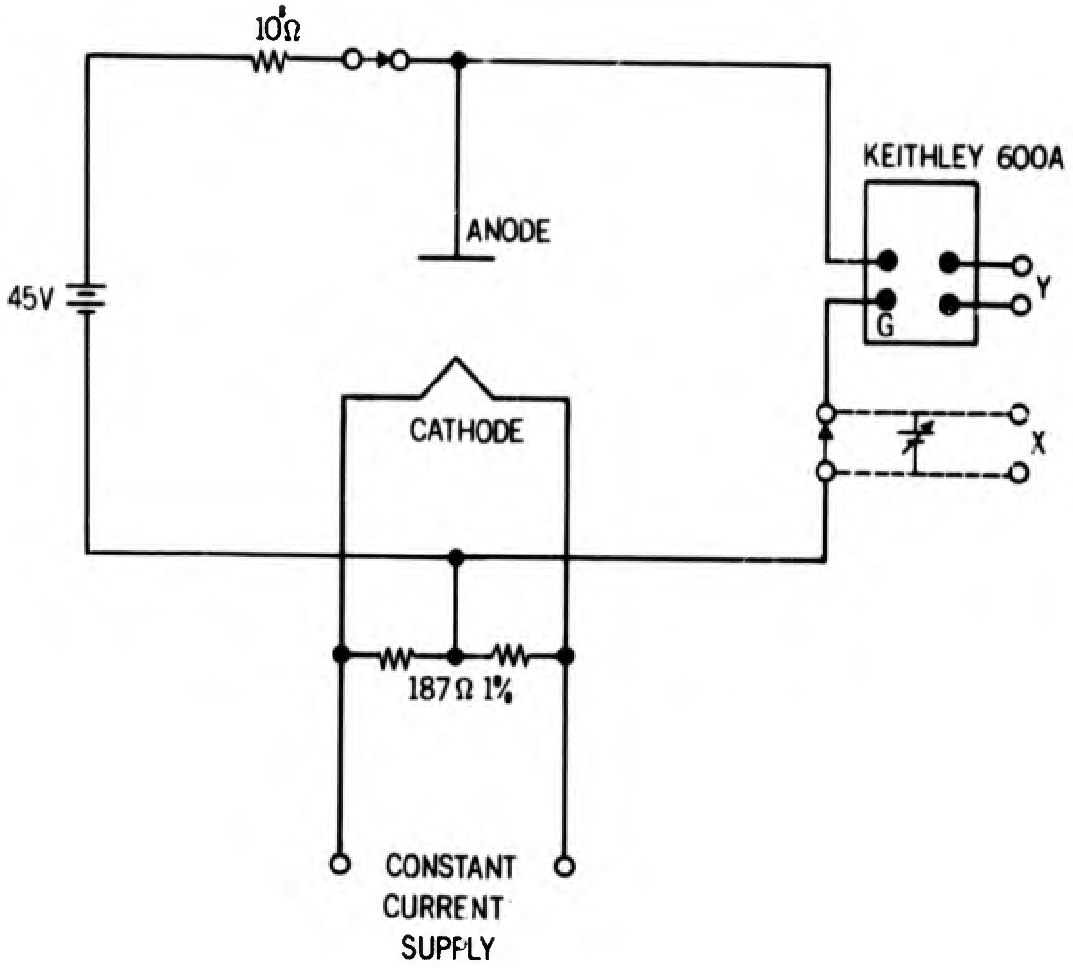

FIG. 26 RETARDING-FIELD DIODE CIRCUIT

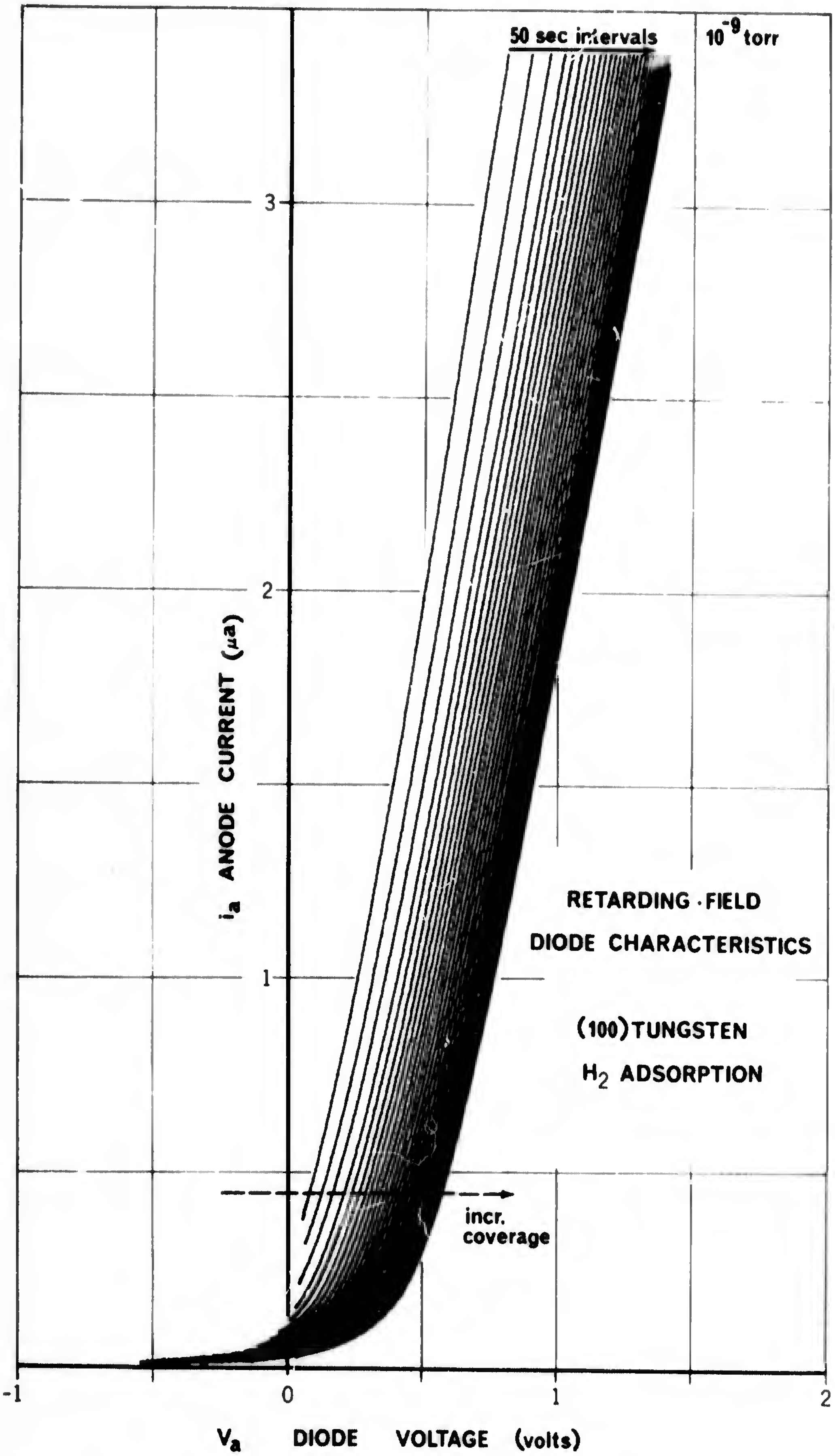

FIG. 27 A FAMILY OF RFD CHARACTERISTICS SHOWING EFFECT OF SURFACE ADSORPTION

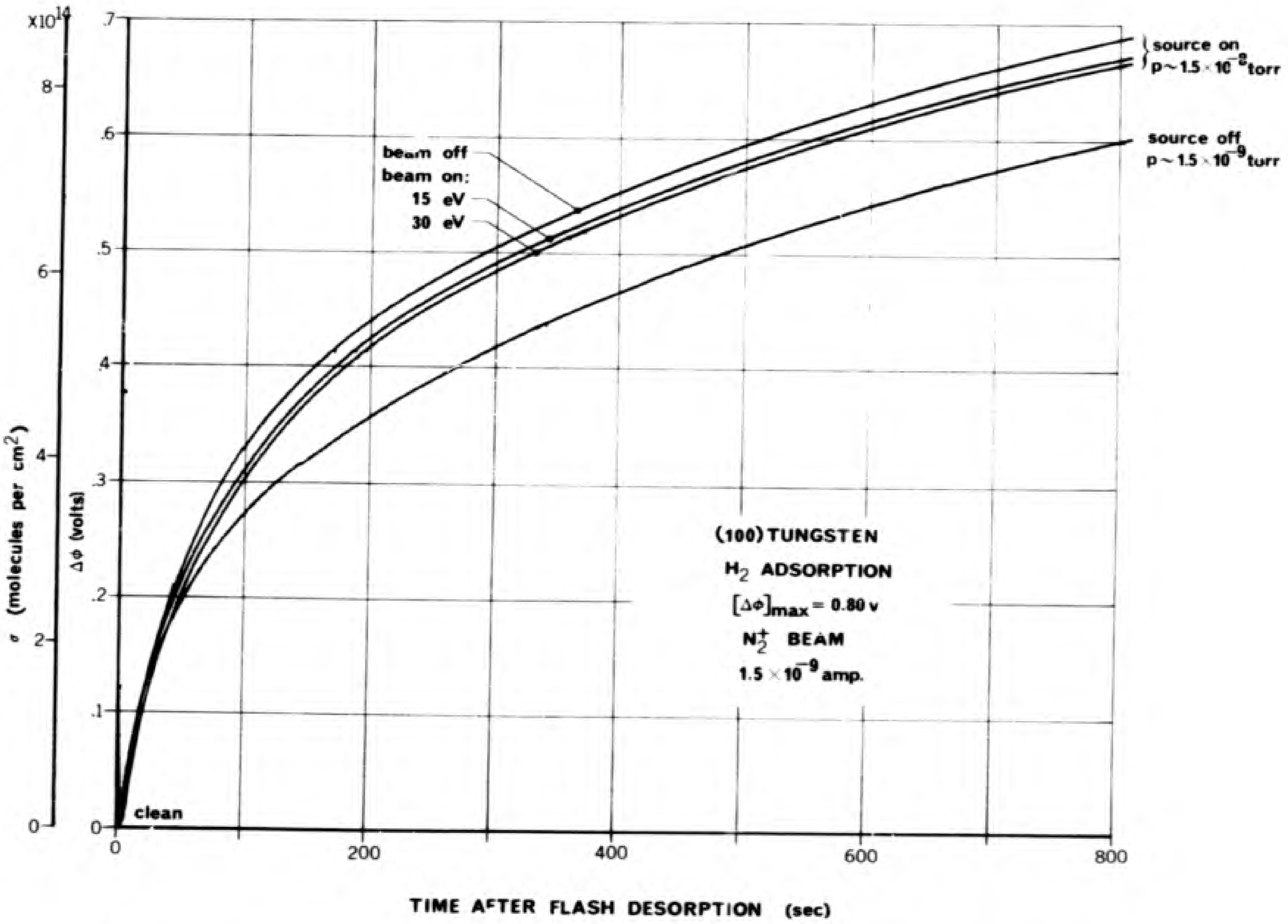

FIG. 28 TRANSIENT BEHAVIOUR OF THE (100) TUNGSTEN TARGET WORK FUNCTION DUE TO HYDROGEN ADSORPTION. (DIATOMIC NITROGEN ION BEAM)

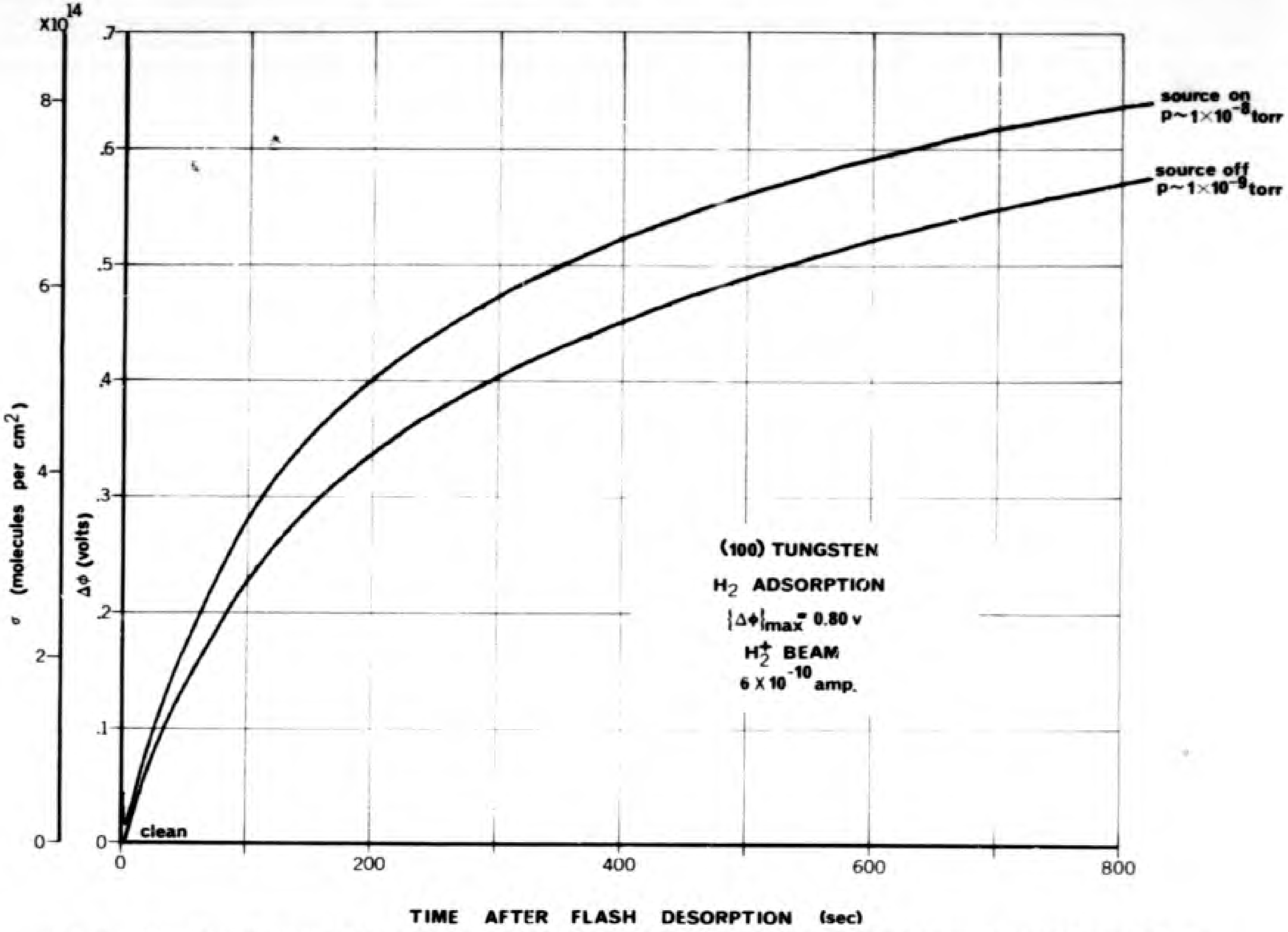

FIG. 29 TRANSIENT BEHAVIOUR OF THE (100) TUNGSTEN TARGET WORK FUNCTION DUE TO HYDROGEN ADSORPTION. (DIATOMIC HYDROGEN ION BEAM)

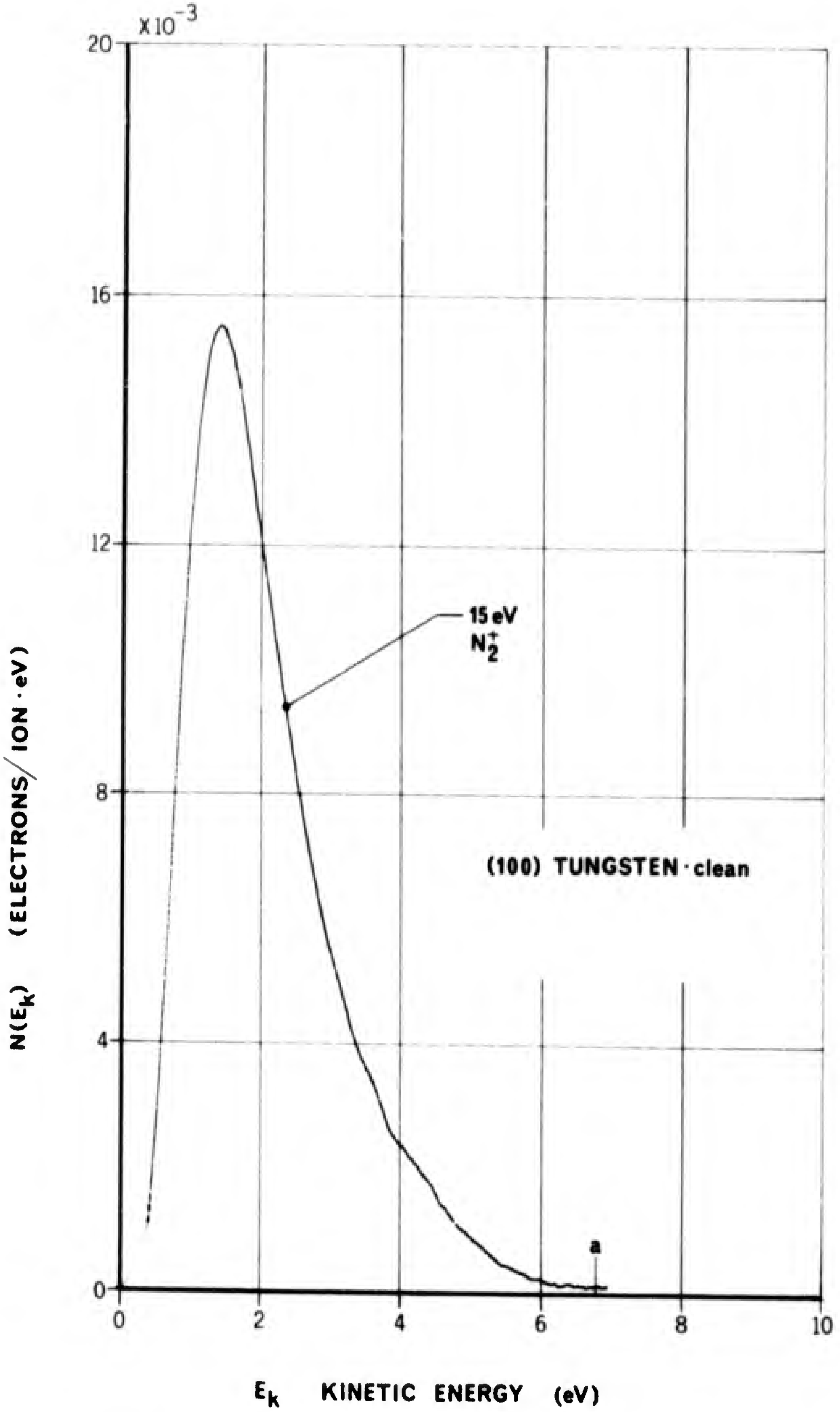

FIG. 30 ENERGY DISTRIBUTION OF SECONDARY ELECTRONS PRODUCED BY AUGER NEUTRALIZATION OF 15 eV N_2^+ IONS AT A CLEAN (100) TUNGSTEN SURFACE

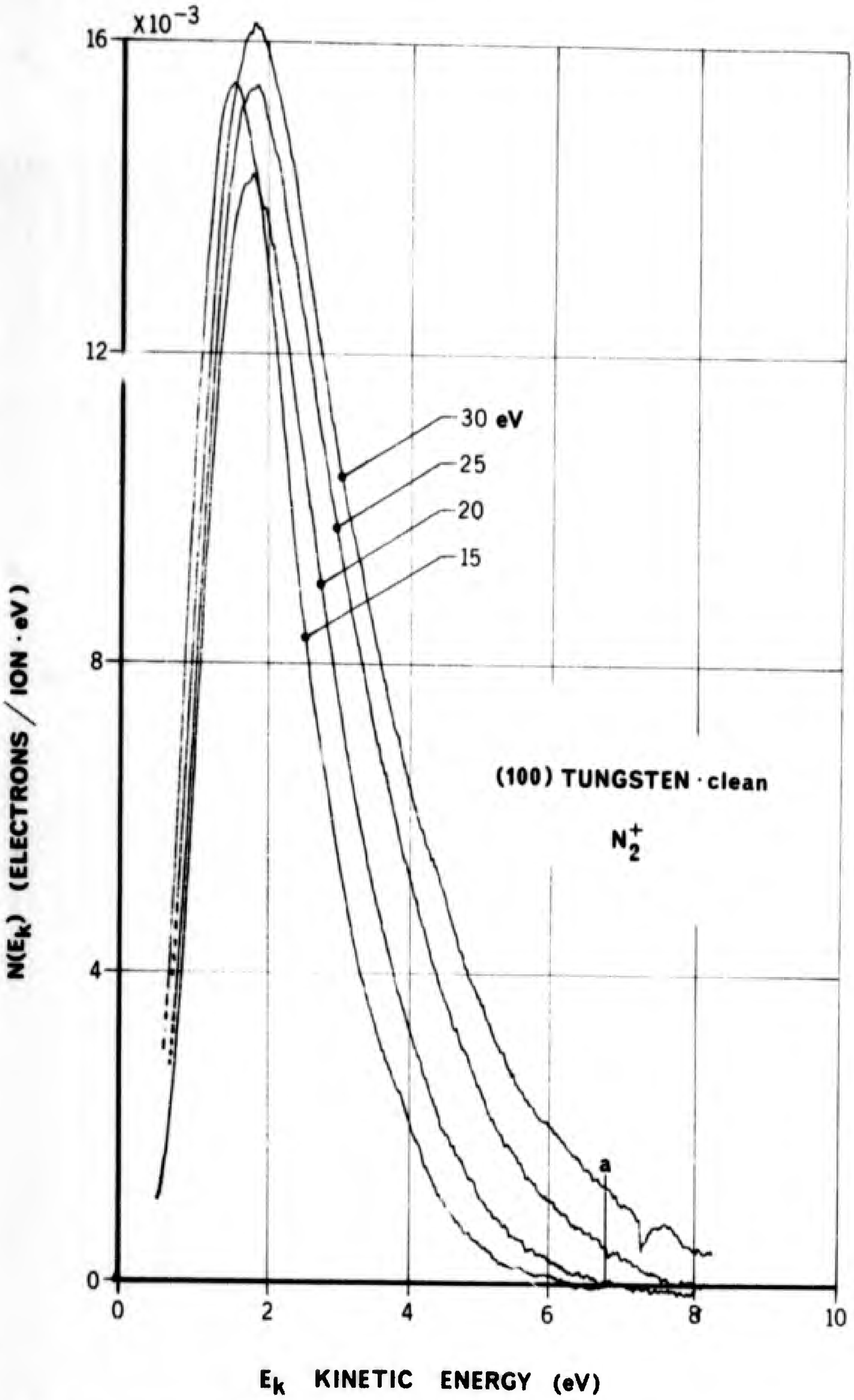

FIG. 31 ENERGY DISTRIBUTION OF SECONDARY ELECTRONS PRODUCED BY AUGER NEUTRALIZATION OF 15, 20, 25, 30 eV N_2^+ IONS AT A CLEAN (100) TUNGSTEN SURFACE

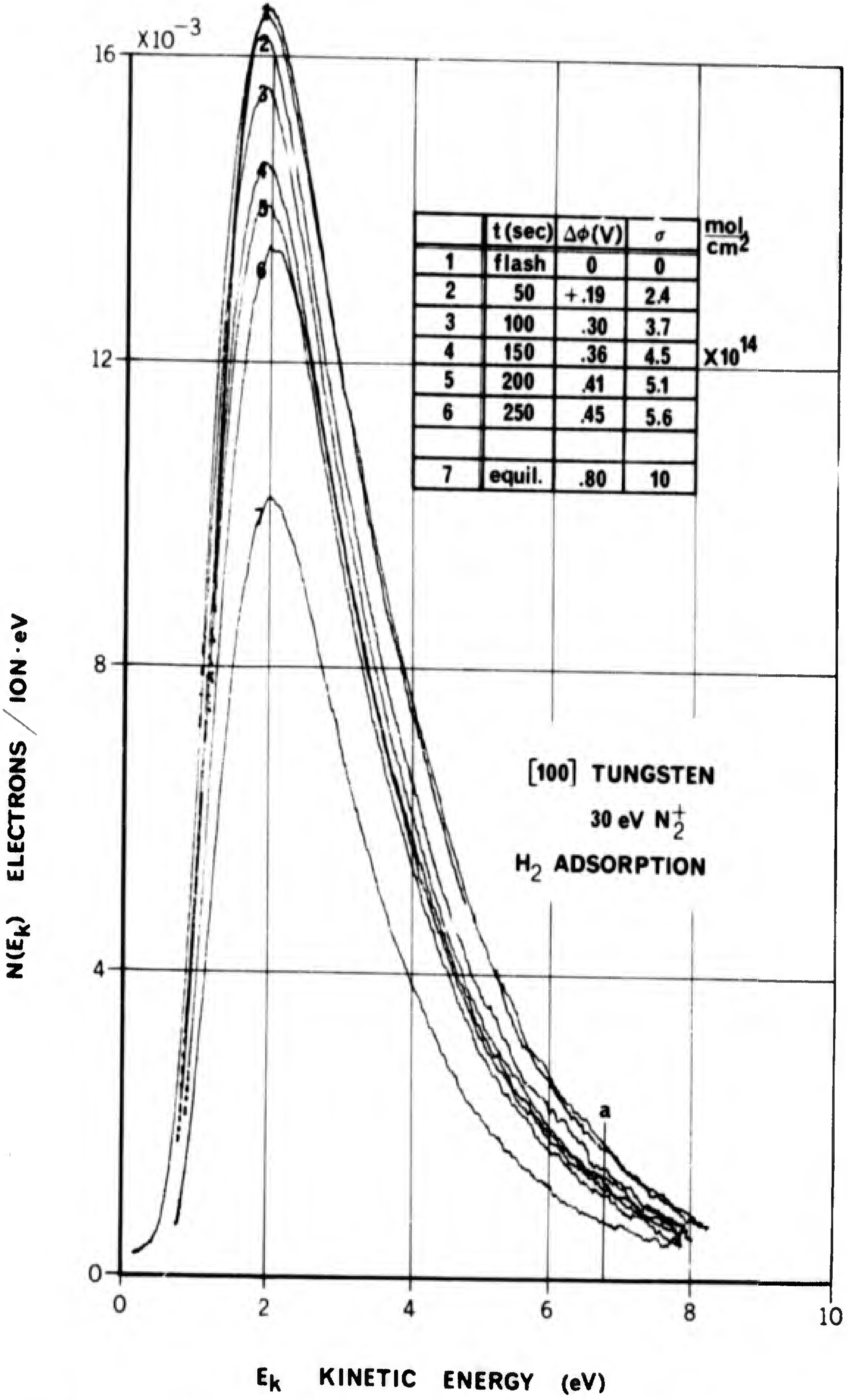

	t(sec)	Δφ(V)	σ mol/cm^2 ×10^{14}
1	flash	0	0
2	50	+.19	2.4
3	100	.30	3.7
4	150	.36	4.5
5	200	.41	5.1
6	250	.45	5.6
7	equil.	.80	10

FIG. 32 ENERGY DISTRIBUTION OF SECONDARY ELECTRONS PRODUCED BY AUGER NEUTRALIZATION OF 30 eV N_2^+ IONS AT A (100) TUNGSTEN SURFACE SHOWING EFFECT OF HYDROGEN ADSORPTION

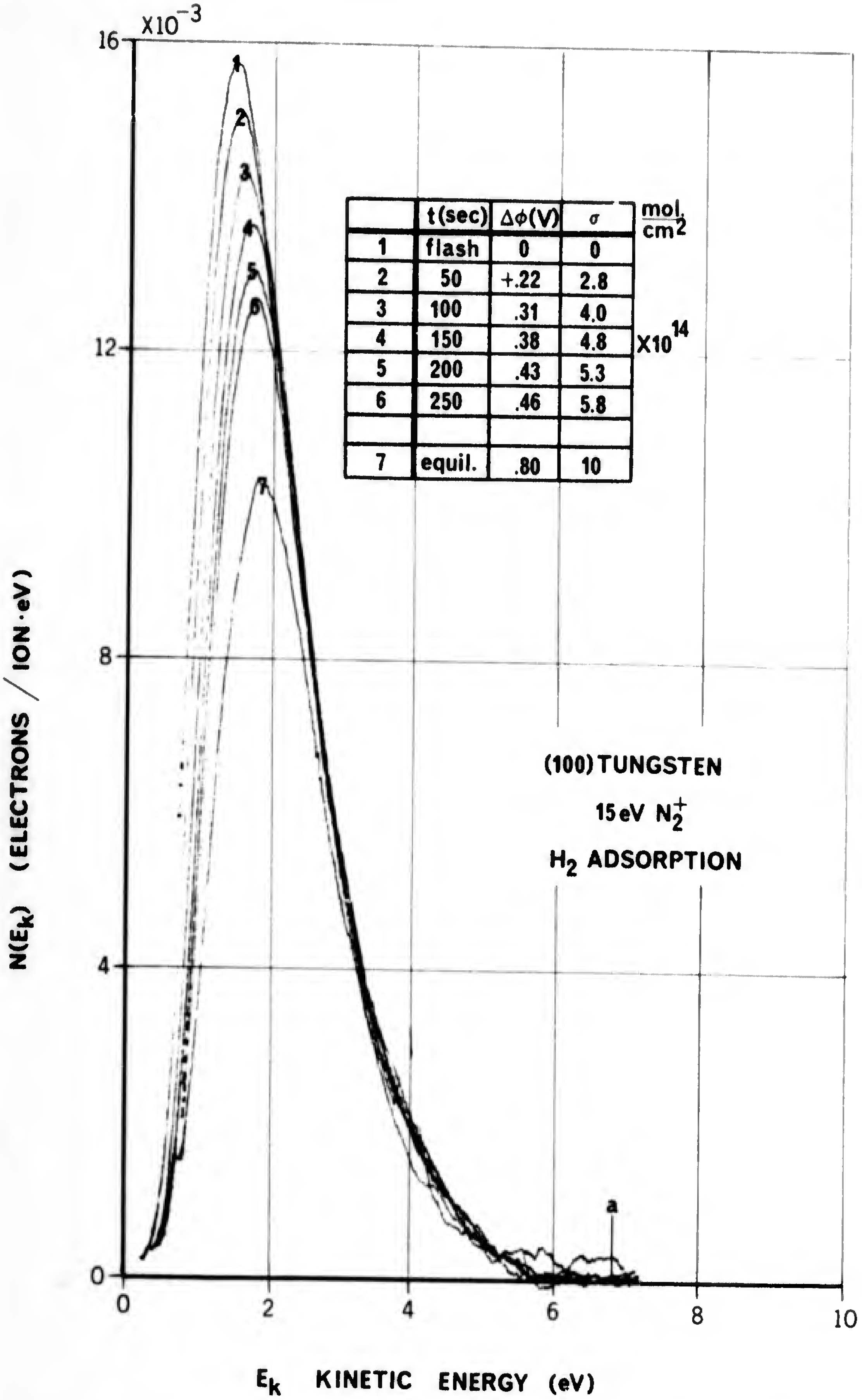

	t(sec)	$\Delta\phi$(V)	σ $\frac{\text{mol.}}{\text{cm}^2}$
1	flash	0	0
2	50	+.22	2.8
3	100	.31	4.0
4	150	.38	4.8
5	200	.43	5.3
6	250	.46	5.8
7	equil.	.80	10

FIG. 33 ENERGY DISTRIBUTION OF SECONDARY ELECTRONS PRODUCED BY AUGER NEUTRALIZATION OF 15 eV N_2^+ IONS AT A (100) TUNGSTEN SURFACE SHOWING EFFECT OF HYDROGEN ADSORPTION

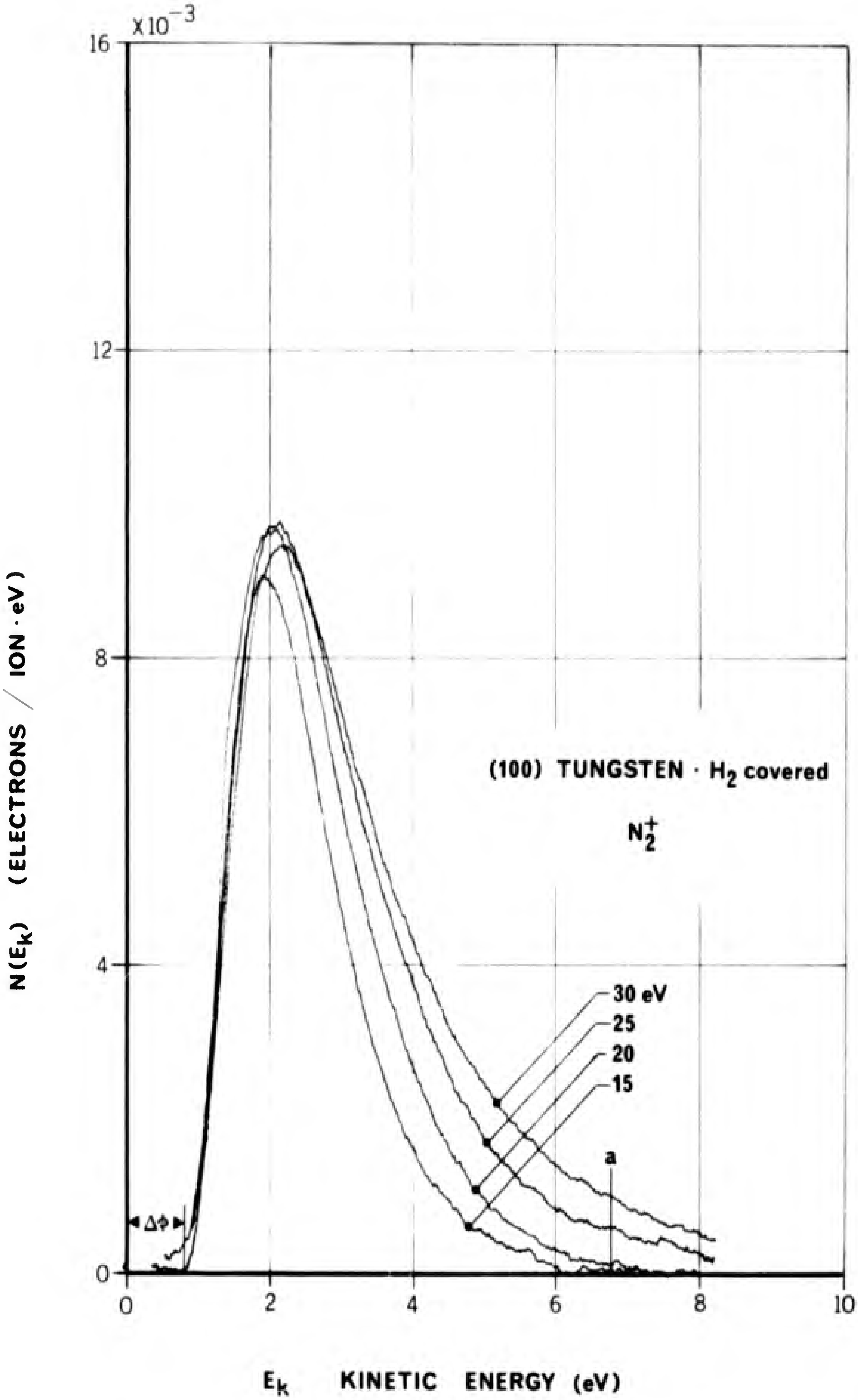

FIG. 34 ENERGY DISTRIBUTION OF SECONDARY ELECTRONS PRODUCED BY AUGER NEUTRALIZATION OF 15, 20, 25, 30 eV N_2^+ IONS AT A HYDROGEN-COVERED (100) TUNGSTEN SURFACE

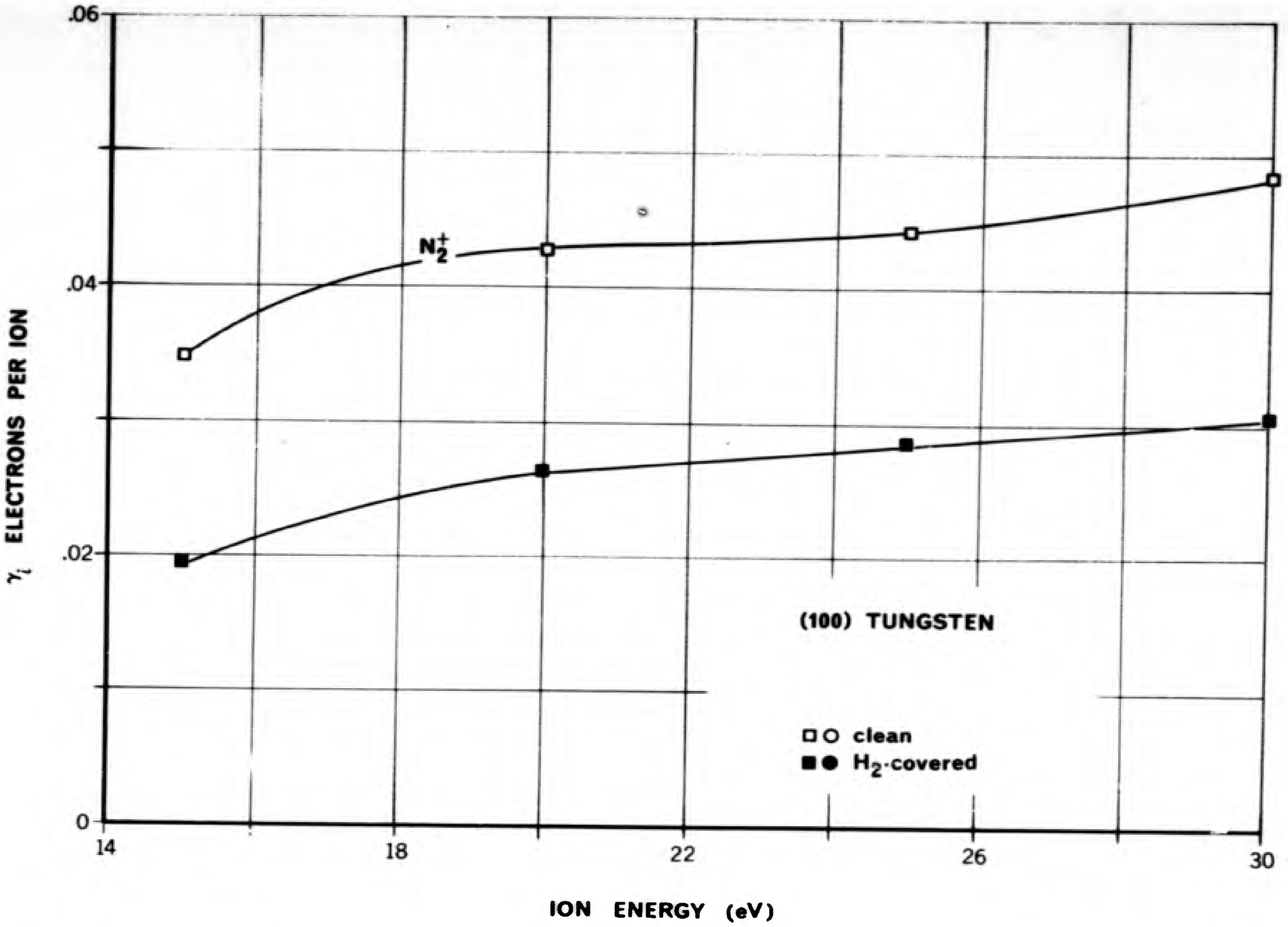

FIG. 35 DEPENDENCE OF ELECTRON YIELD ON INCIDENT ION KINETIC ENERGY FOR DIATOMIC IONS AT A CLEAN AND HYDROGEN-COVERED (100) TUNGSTEN SURFACE

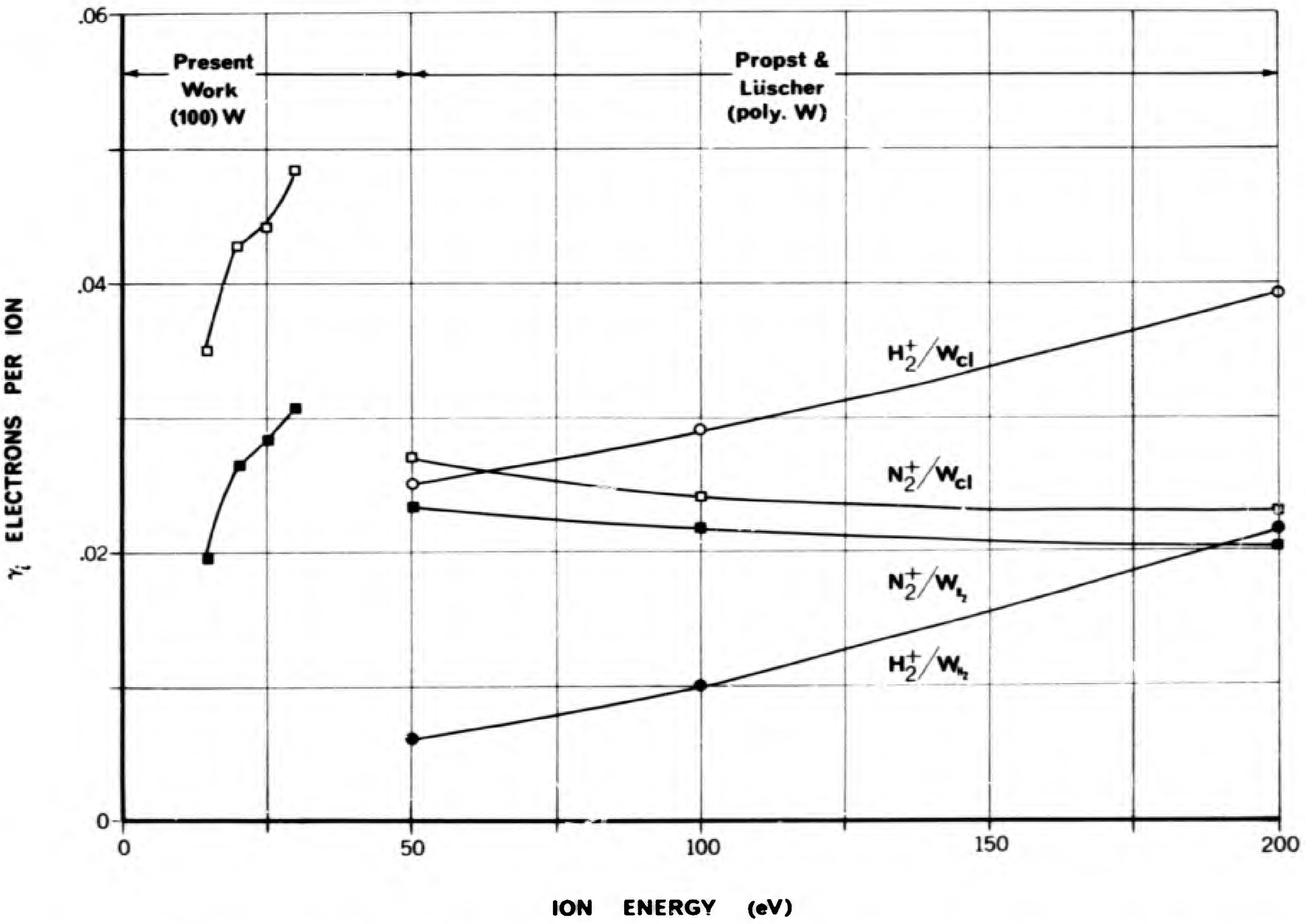

FIG. 36 COMPARISON OF ELECTRON YIELDS FOR DIATOMIC IONS WITH PREVIOUS WORK WITH POLYCRYSTALLINE TUNGSTEN

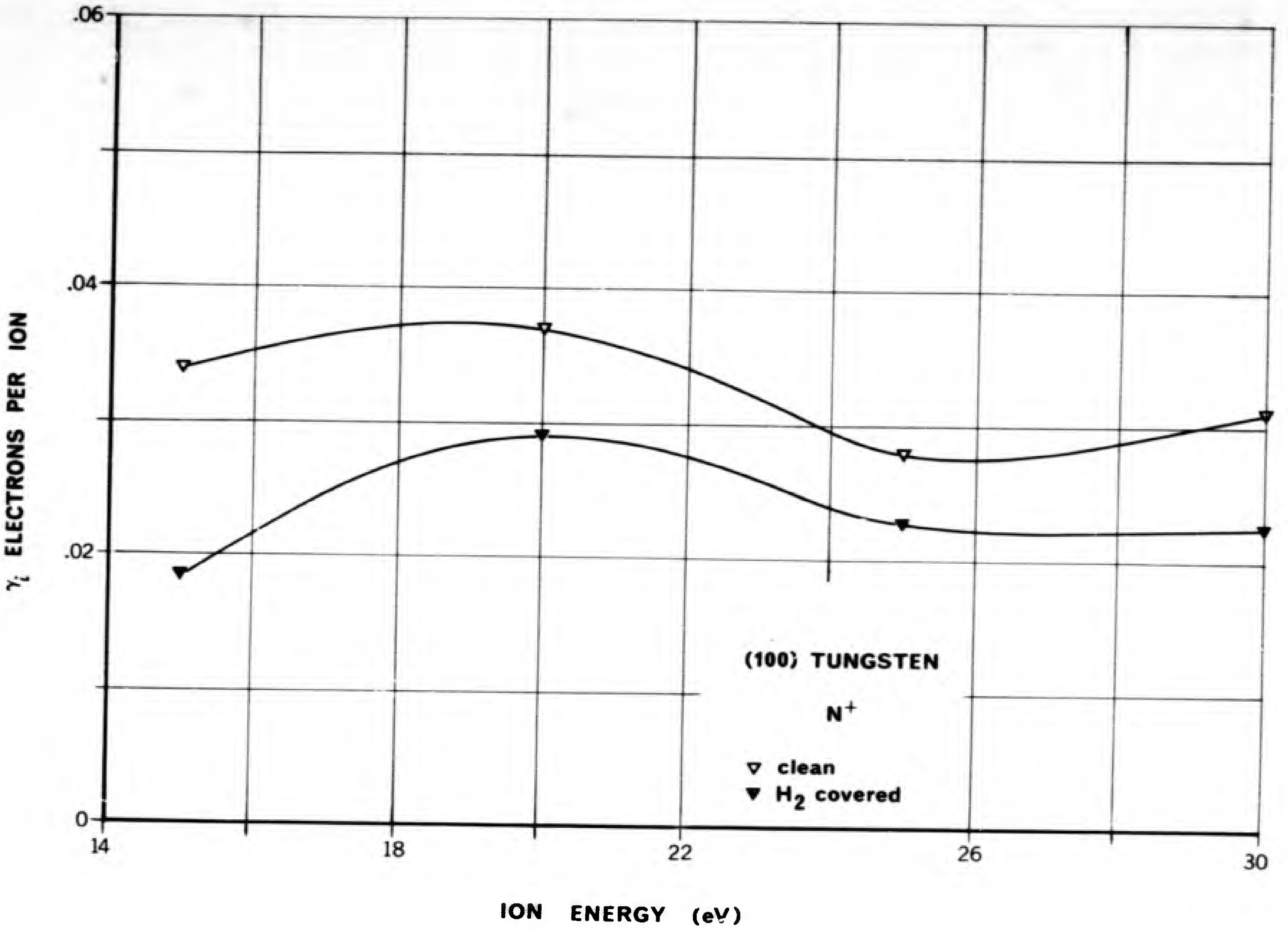

FIG. 37 DEPENDENCE OF ELECTRON YIELD ON INCIDENT ION KINETIC ENERGY FOR N^+ IONS AT A CLEAN AND HYDROGEN-COVERED (100) TUNGSTEN SURFACE

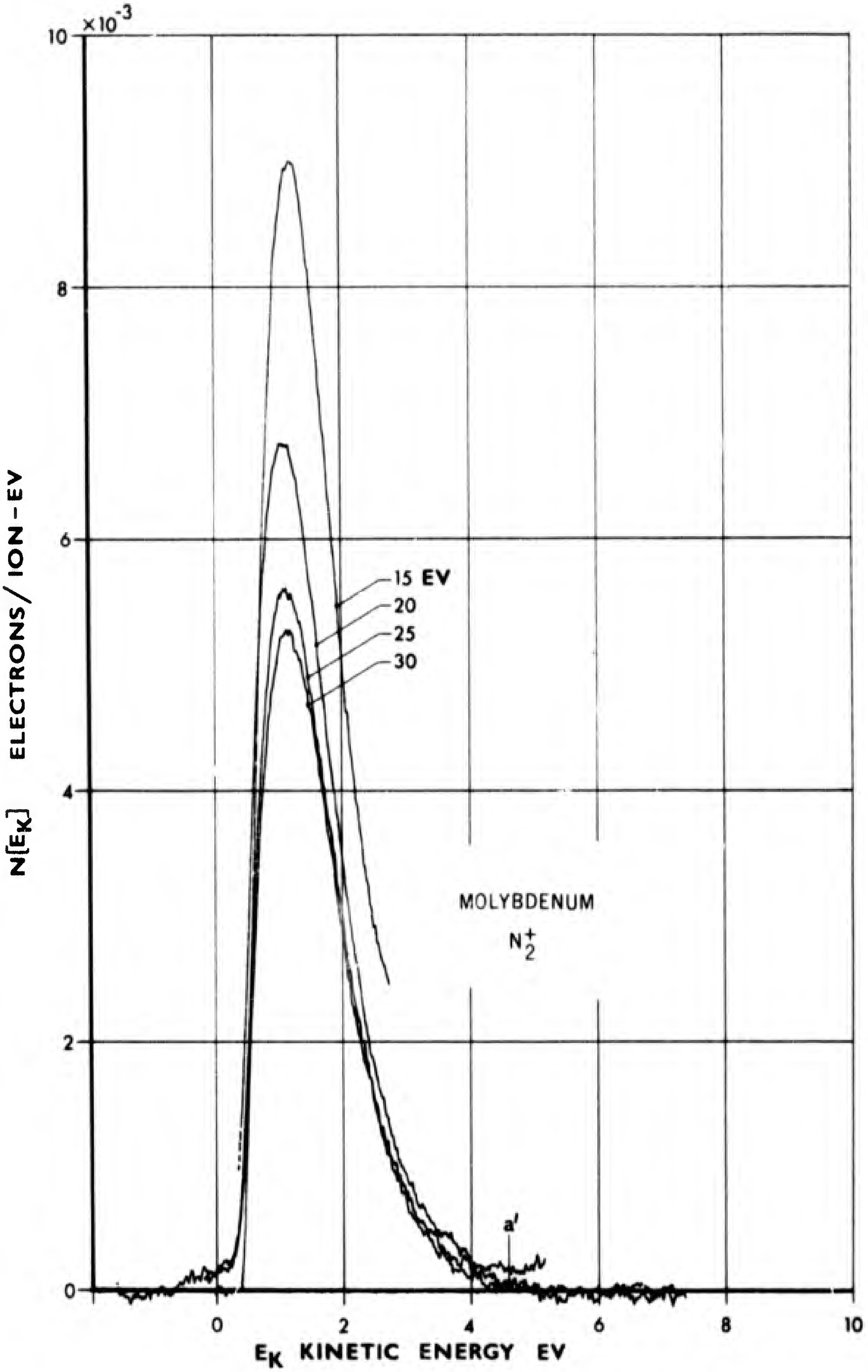

FIG. 38 ENERGY DISTRIBUTION OF SECONDARY ELECTRONS PRODUCED BY AUGER NEUTRALIZATION OF 15, 20, 25, 30 eV N_2^+ IONS AT A CONTAMINATED POLYCRYSTALLINE MOLYBDENUM SURFACE

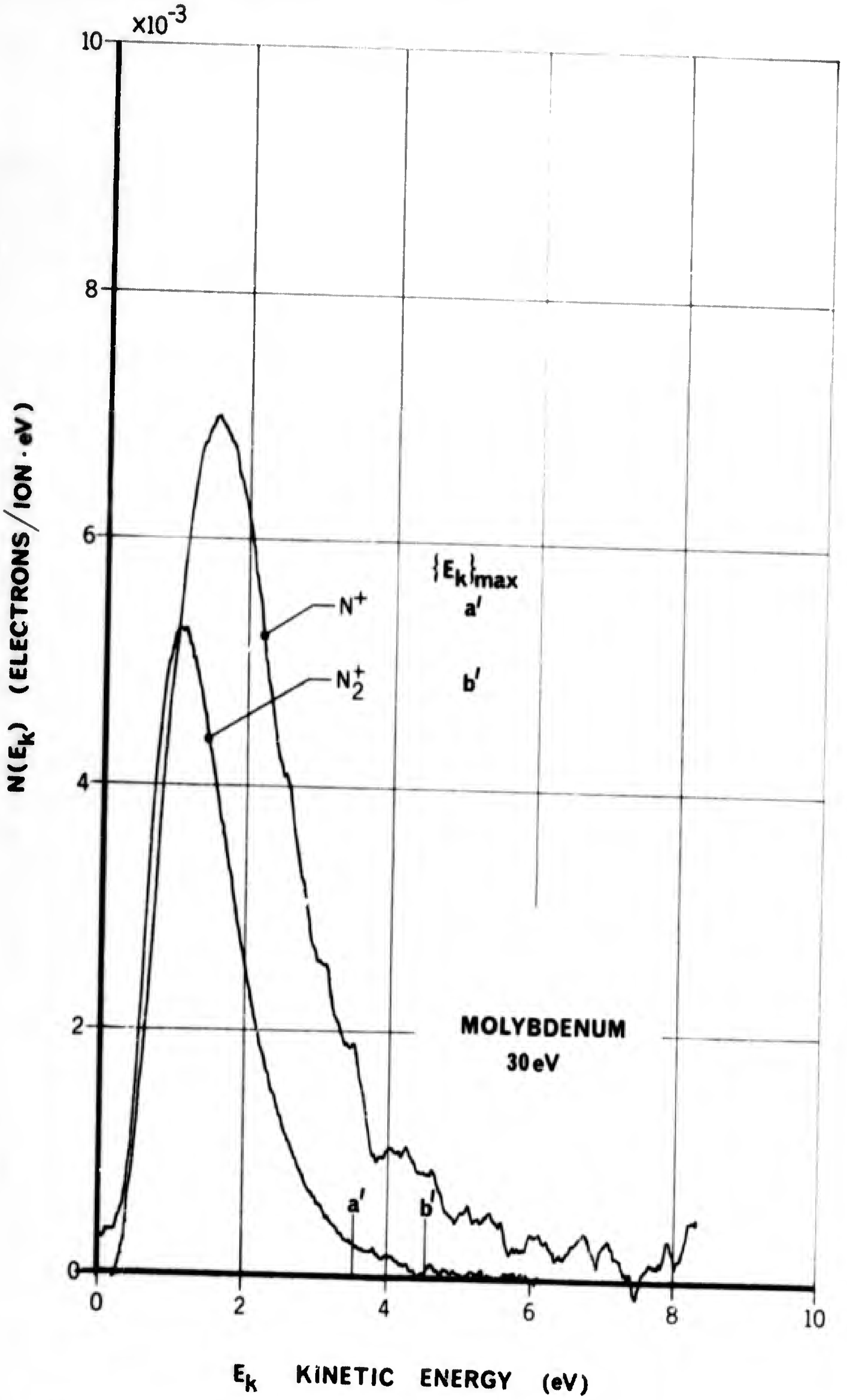

FIG. 39 ENERGY DISTRIBUTION OF SECONDARY ELECTRONS PRODUCED BY 30 eV N^+, N_2^+ IONS AT A CONTAMINATED MOLYBDENUM SURFACE

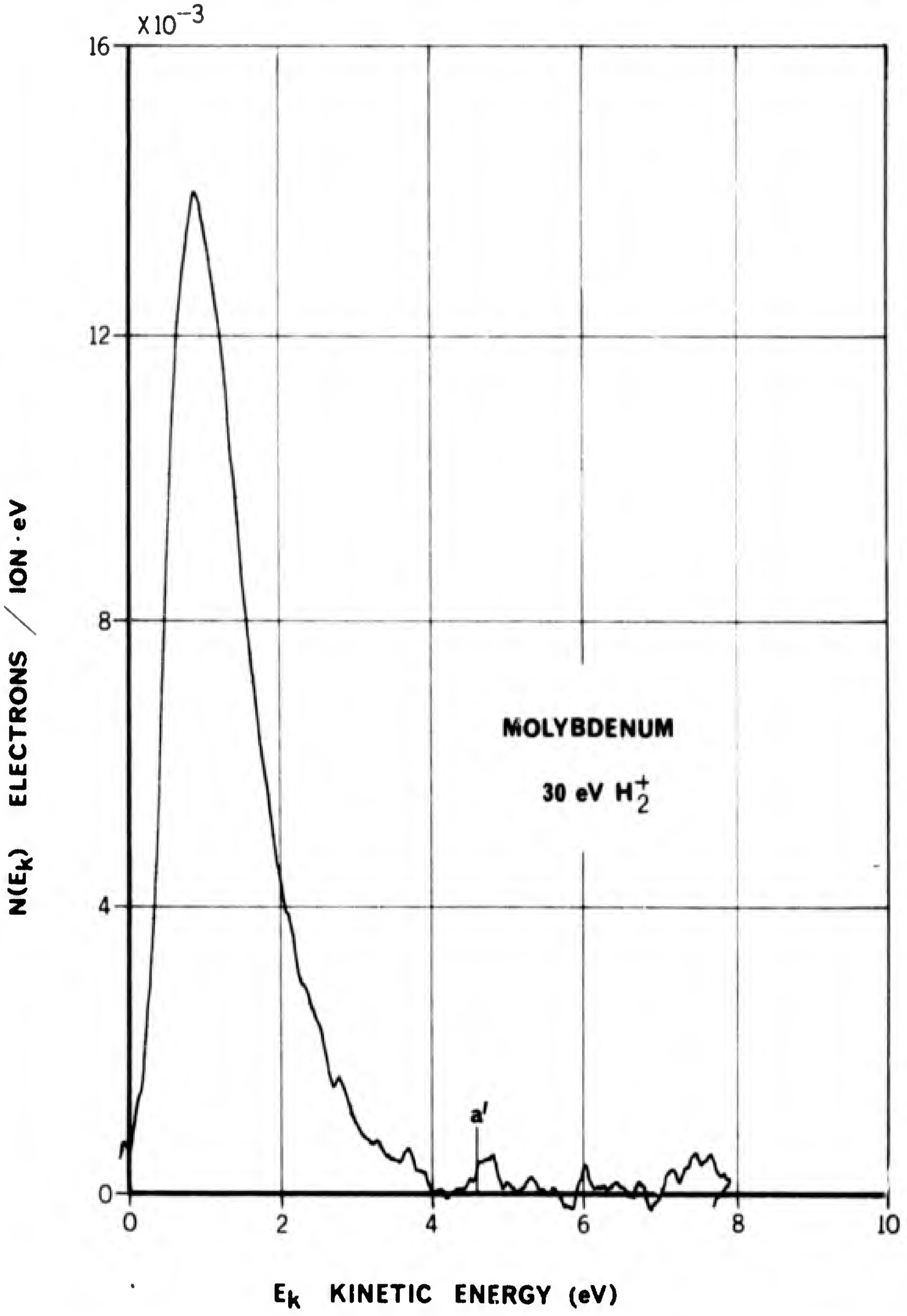

FIG. 40 ENERGY DISTRIBUTION OF SECONDARY ELECTRONS PRODUCED BY THE AUGER NEUTRALIZATION OF 30 eV H_2^+ IONS AT A CONTAMINATED POLYCRYSTALLINE MOLYBDENUM SURFACE

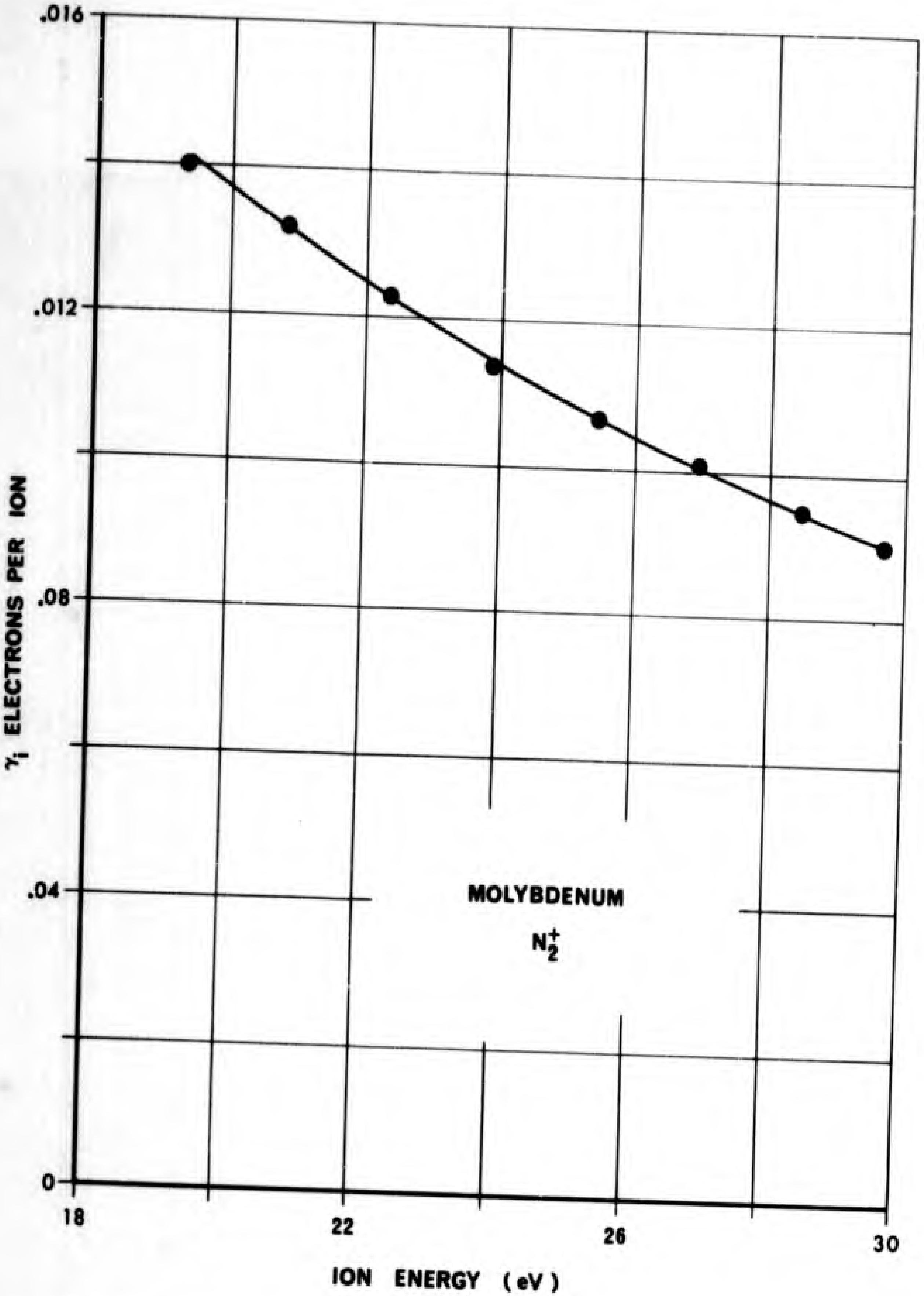

FIG. 41 DEPENDENCE OF ELECTRON YIELD ON INCIDENT ION KINETIC ENERGY FOR N_2^+ IONS AT A CONTAMINATED POLYCRYSTALLINE MOLYBDENUM SURFACE

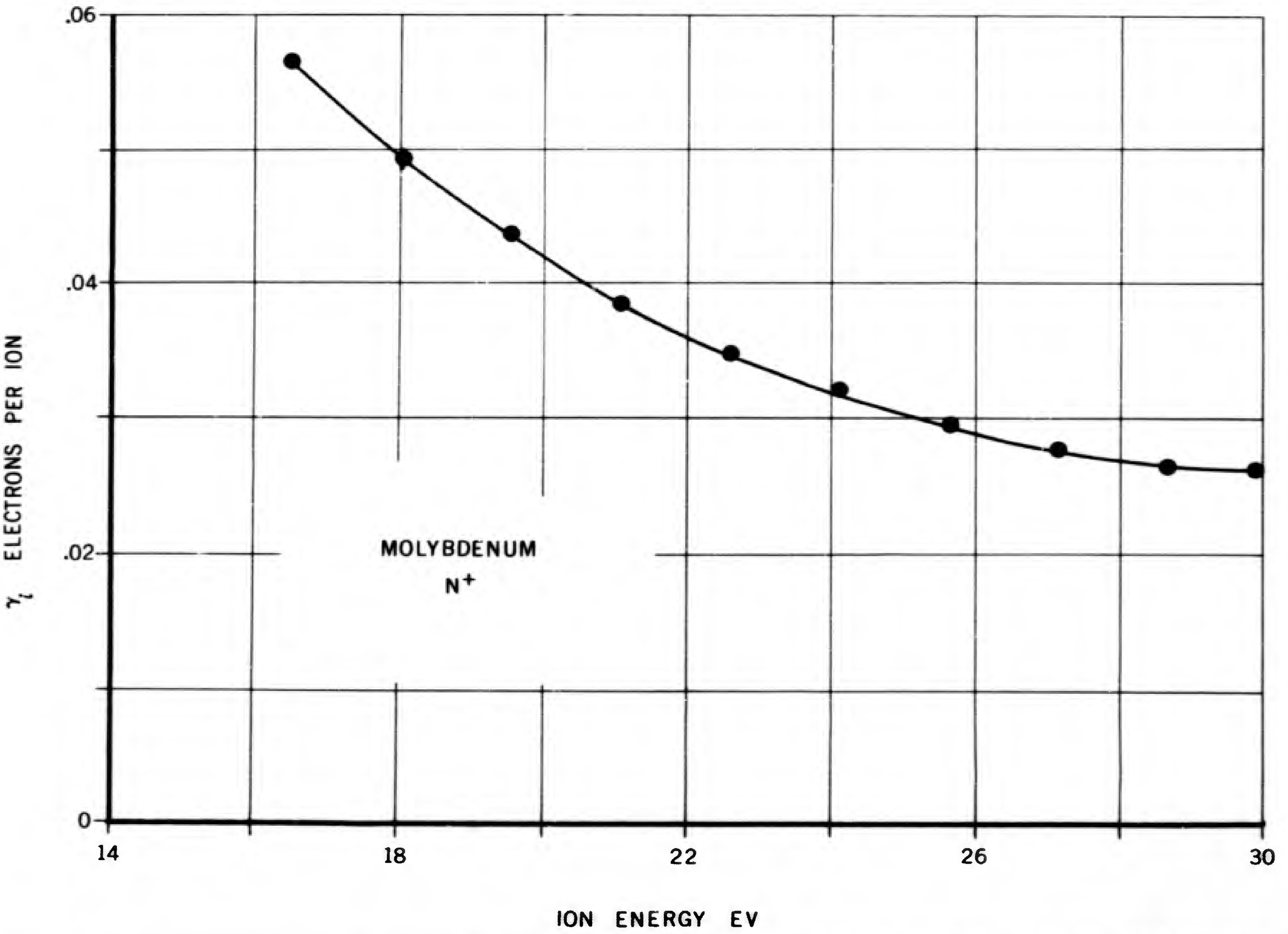

FIG. 42 DEPENDENCE OF ELECTRON YIELD ON INCIDENT ION KINETIC ENERGY FOR N^+ IONS AT A CONTAMINATED POLYCRYSTALLINE MOLYBDENUM SURFACE

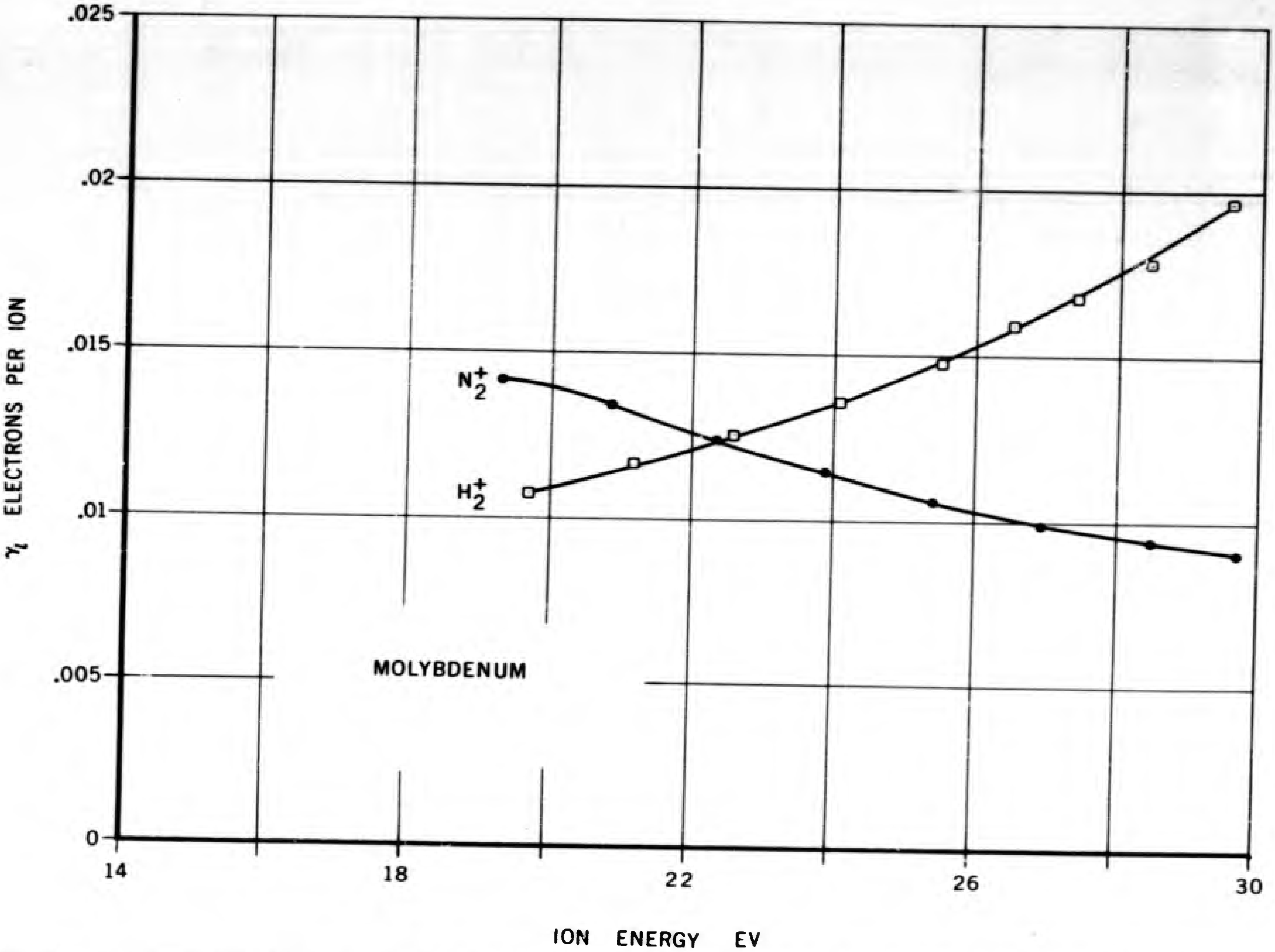

FIG. 43 DEPENDENCE OF ELECTRON YIELD ON INCIDENT ION KINETIC ENERGY FOR DIATOMIC IONS AT A CONTAMINATED POLYCRYSTALLINE MOLYBDENUM SURFACE

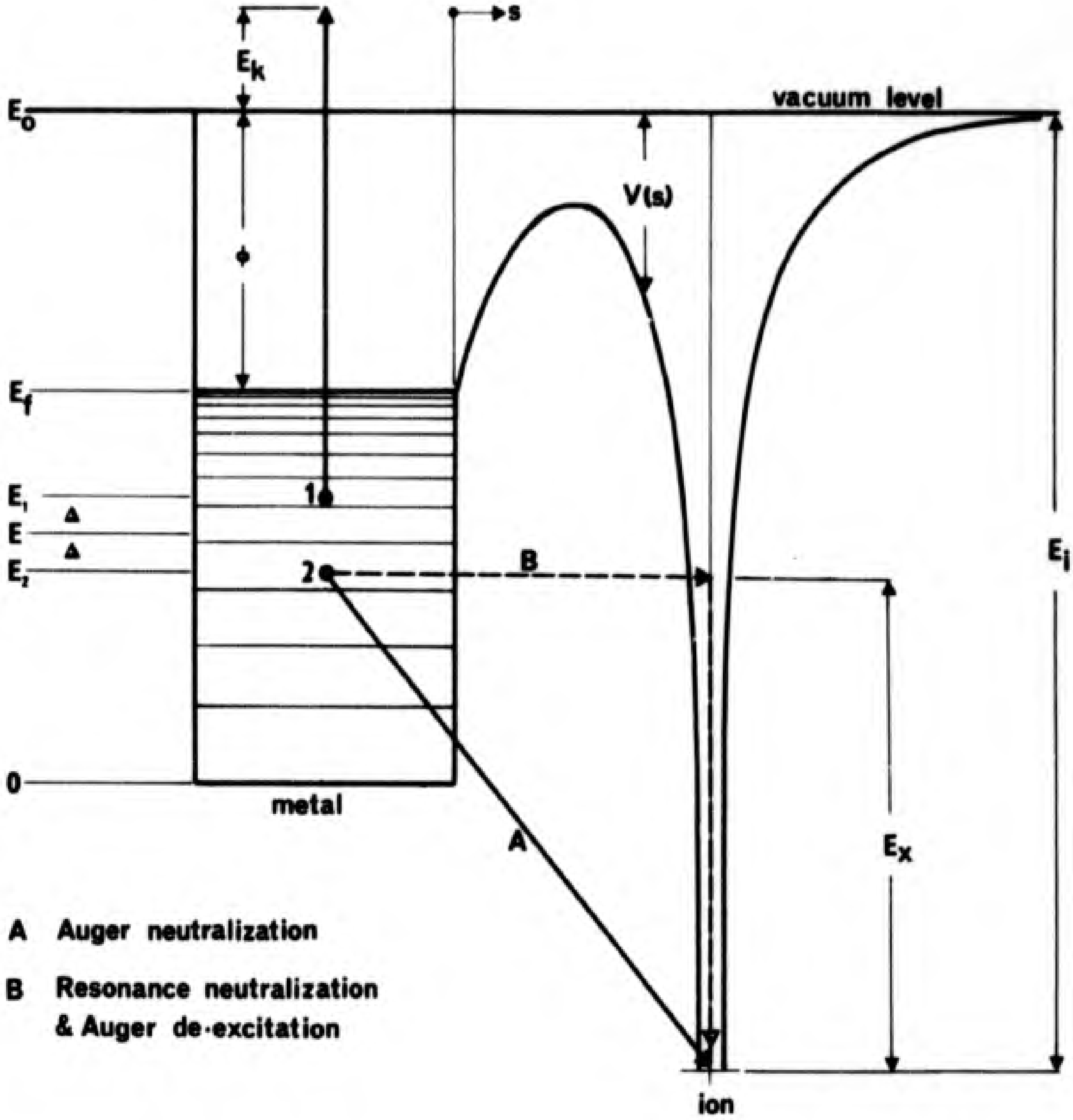

FIG. 44 SCHEMATIC DIAGRAM ILLUSTRATING THE AUGER PROCESSES RESULTING IN THE NEUTRALIZATION OF LOW-ENERGY IONS AT A METAL SURFACE. (APPROXIMATELY TO SCALE FOR THE N_2^+-TUNGSTEN SYSTEM) Energy released by electron (2) as a result of either transition A or B is totally absorbed by electron (1) which may be excited beyond the vacuum level. (Secondary electron emission).

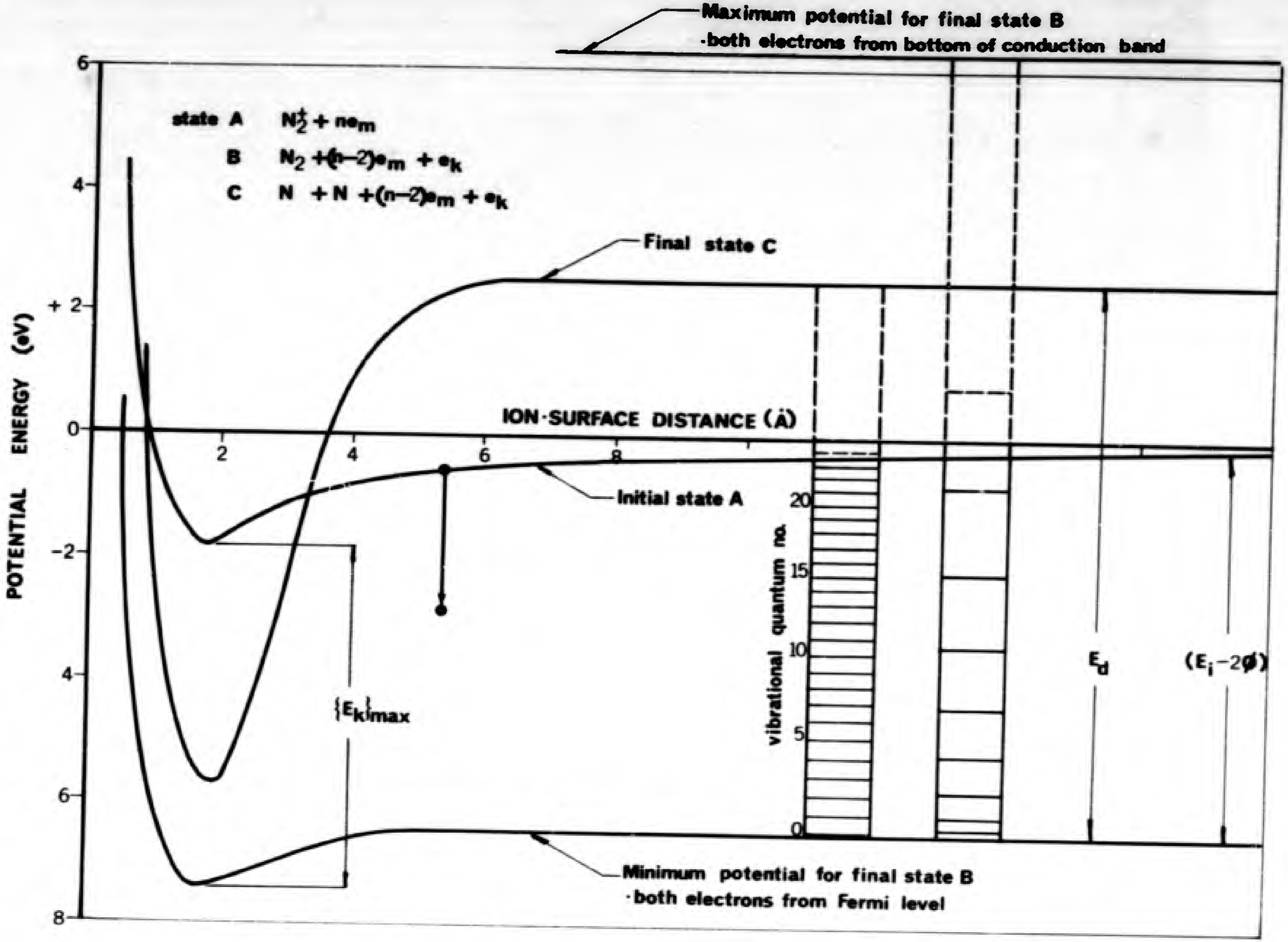

FIG. 45 POTENTIAL ENERGY CURVES OF THE INITIAL AND FINAL STATES FOR NITROGEN-TUNGSTEN CASE.

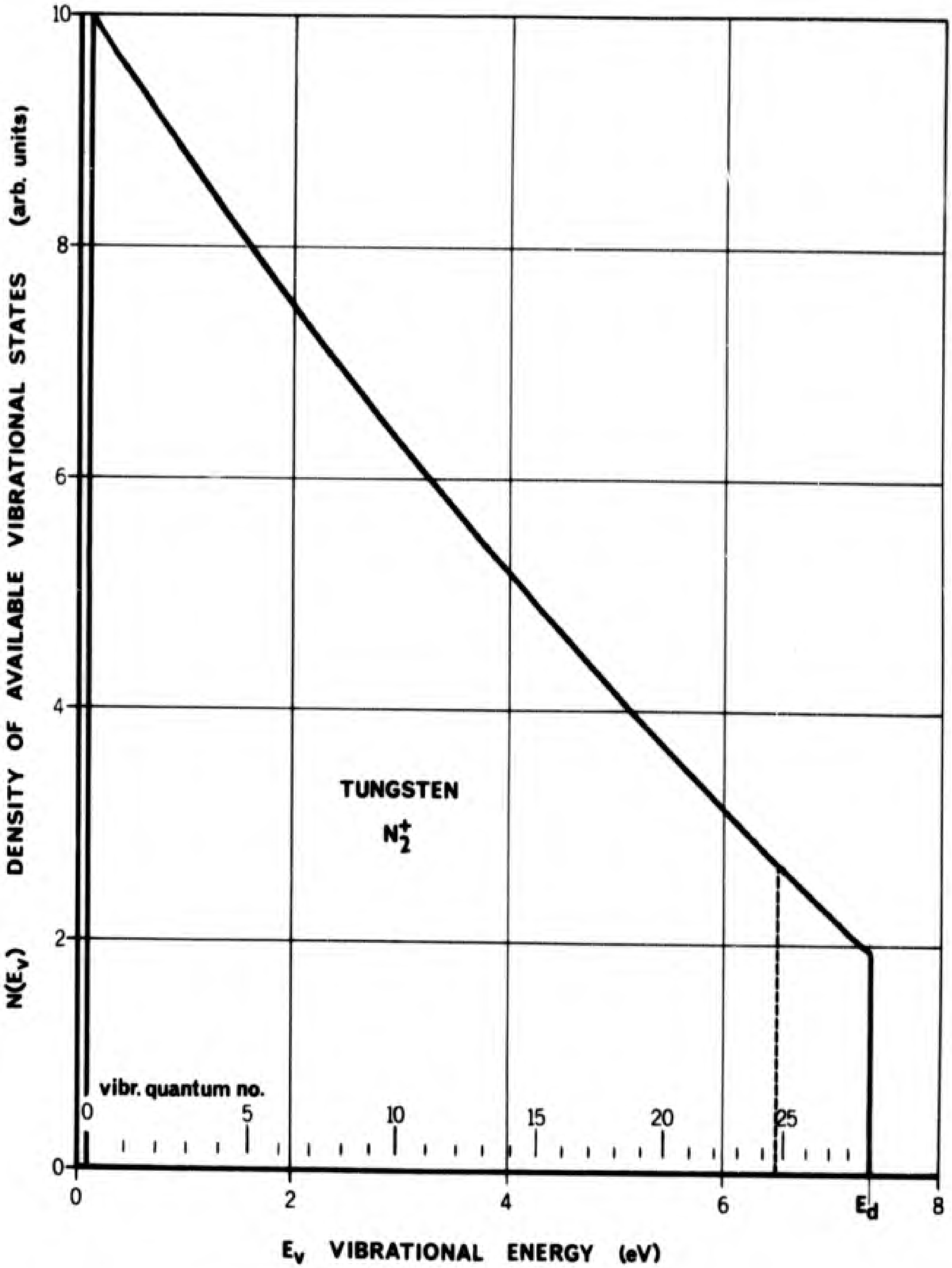

FIG. 46 THE CALCULATED VIBRATIONAL ENERGY DISTRIBUTION FUNCTION FOR N_2^+ IONS NEUTRALIZED AT A TUNGSTEN SURFACE. Excitation beyond $E_V = (E_i - 2\phi)$, shown dotted, cannot occur in conjunction with the production of a free electron.

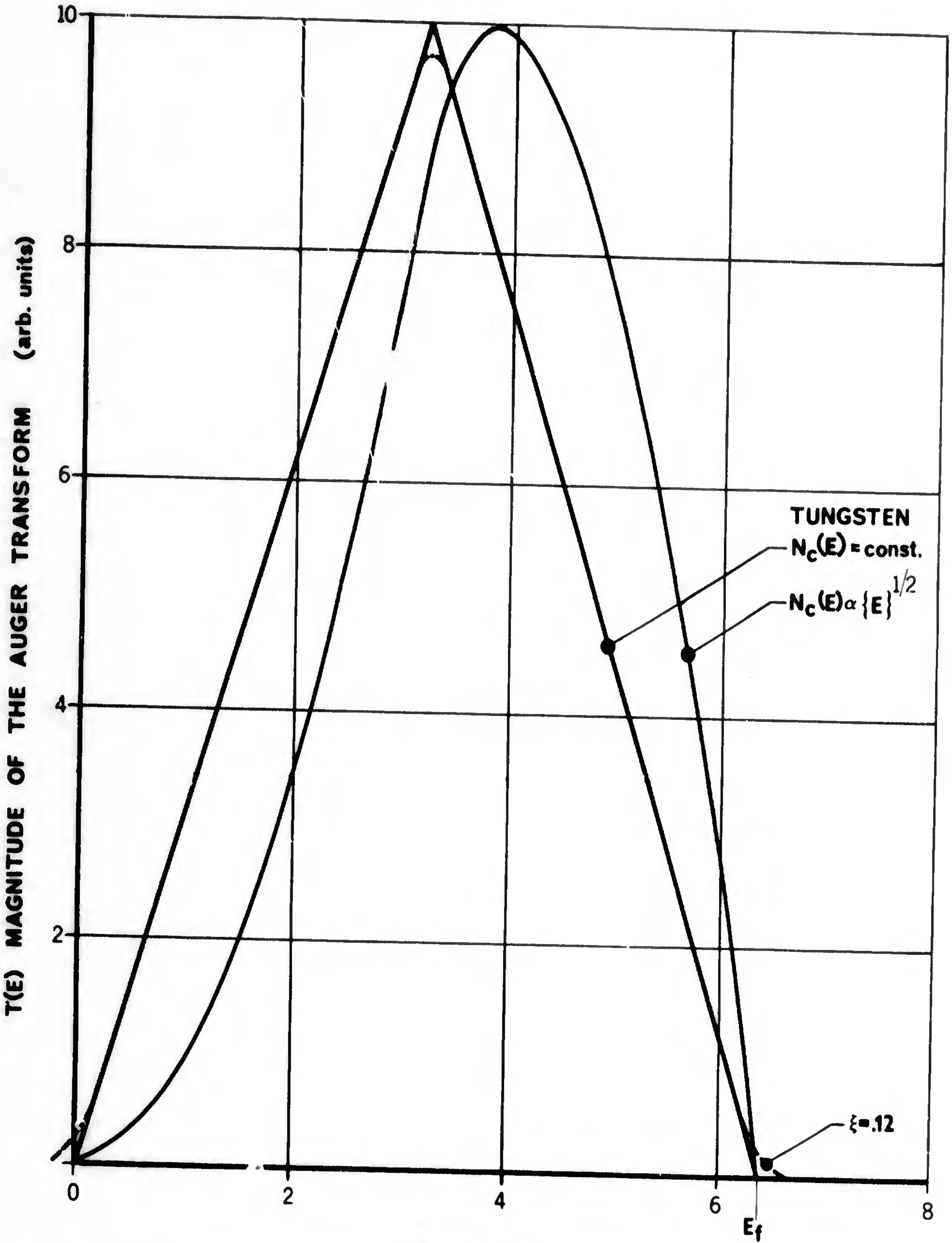

FIG. 47 THE AUGER TRANSFORM FOR TUNGSTEN ASSUMING TWO FORMS OF THE DENSITY OF CONDUCTION BAND STATES.

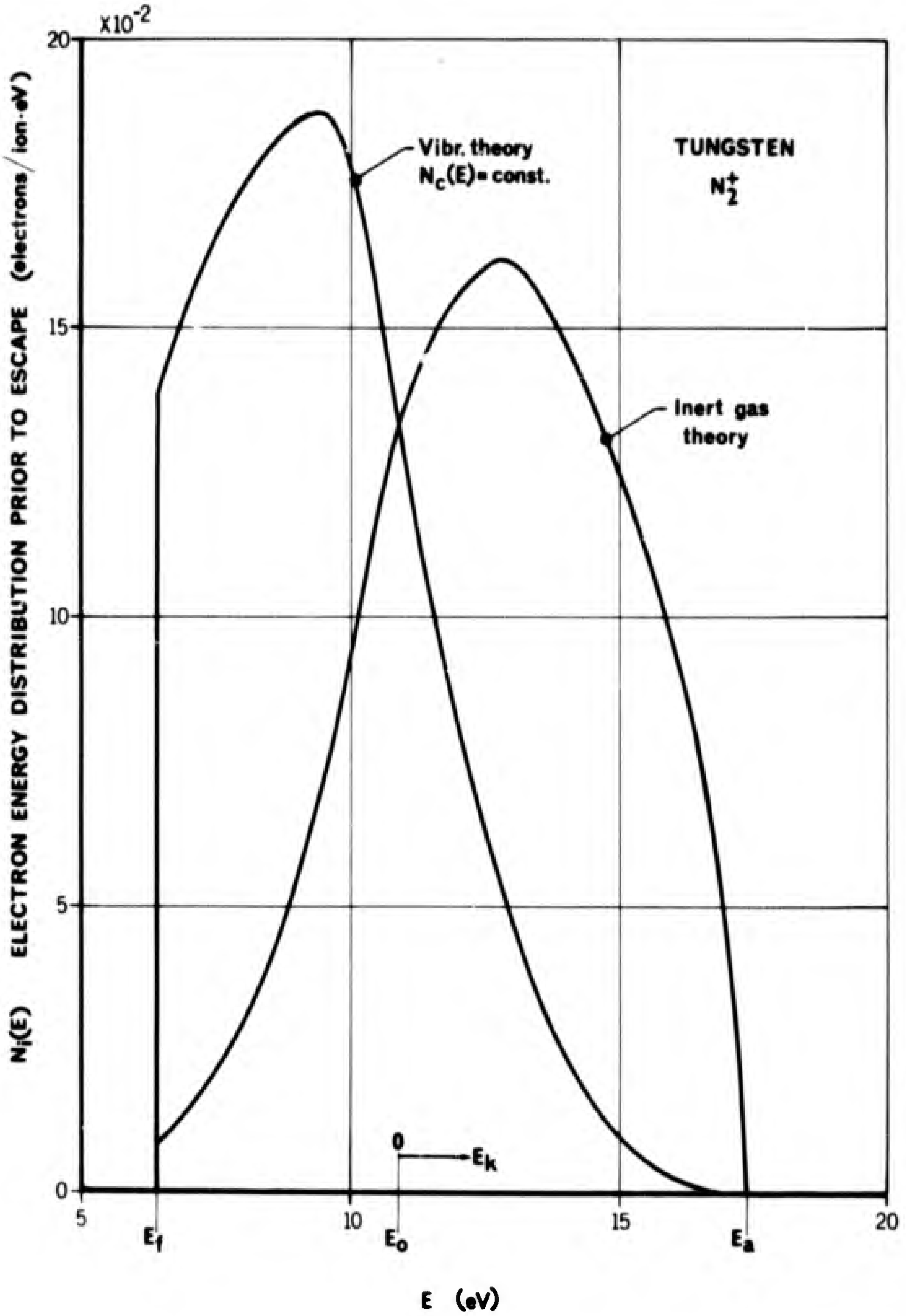

FIG. 48 THE DISTRIBUTION IN KINETIC ENERGY OF ELECTRONS EXCITED BY THE AUGER NEUTRALIZATION OF N_2^+ IONS AT A TUNGSTEN SURFACE, PRIOR TO THEIR ESCAPE. Only those electrons at energies beyond E_0 have finite escape probability. The form of the distribution function without including the possibility of molecular vibrational excitation is shown for comparison.

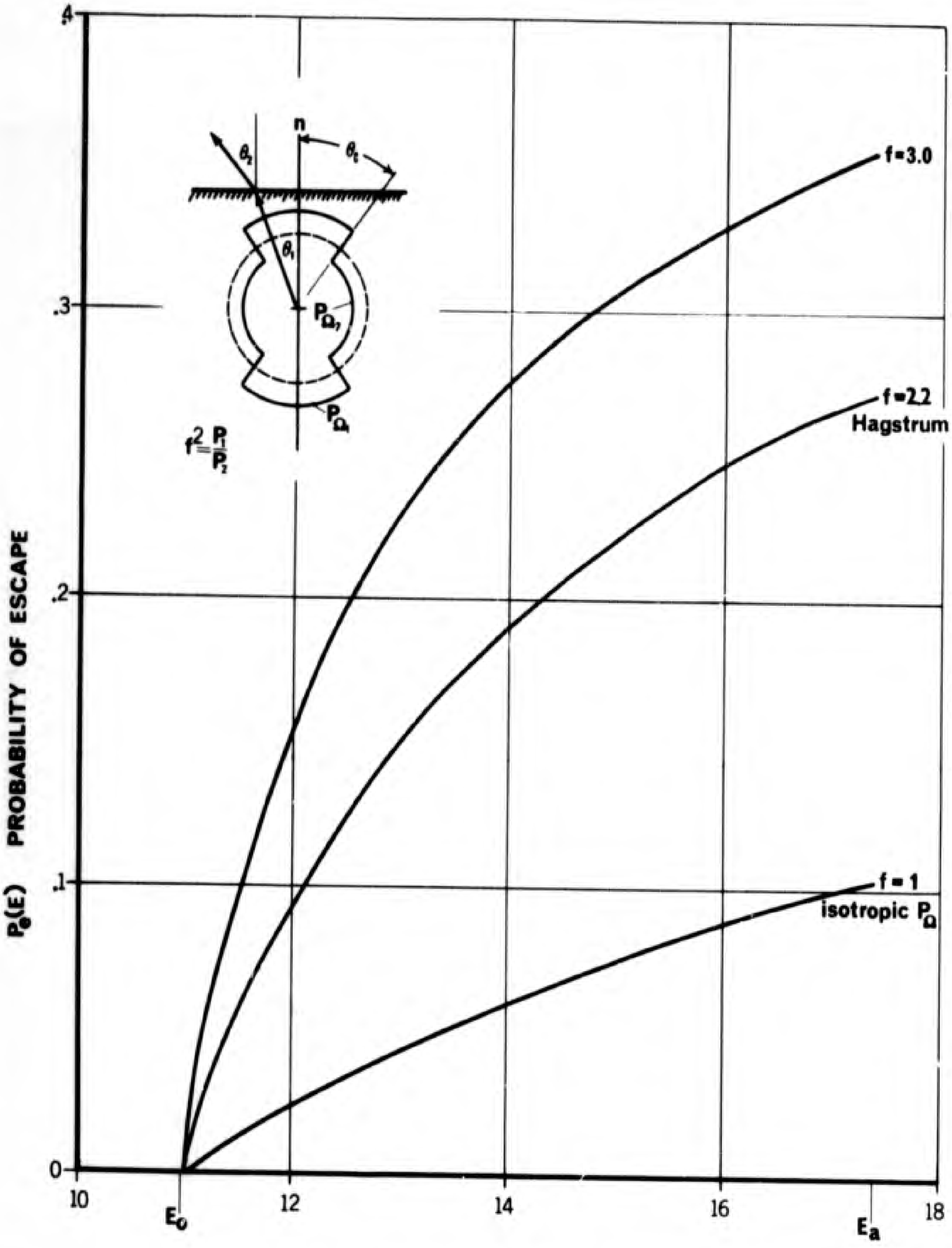

FIG. 49 PLOTS OF THE ESCAPE FUNCTION FOR THREE CHOICES OF THE PARAMETER f.

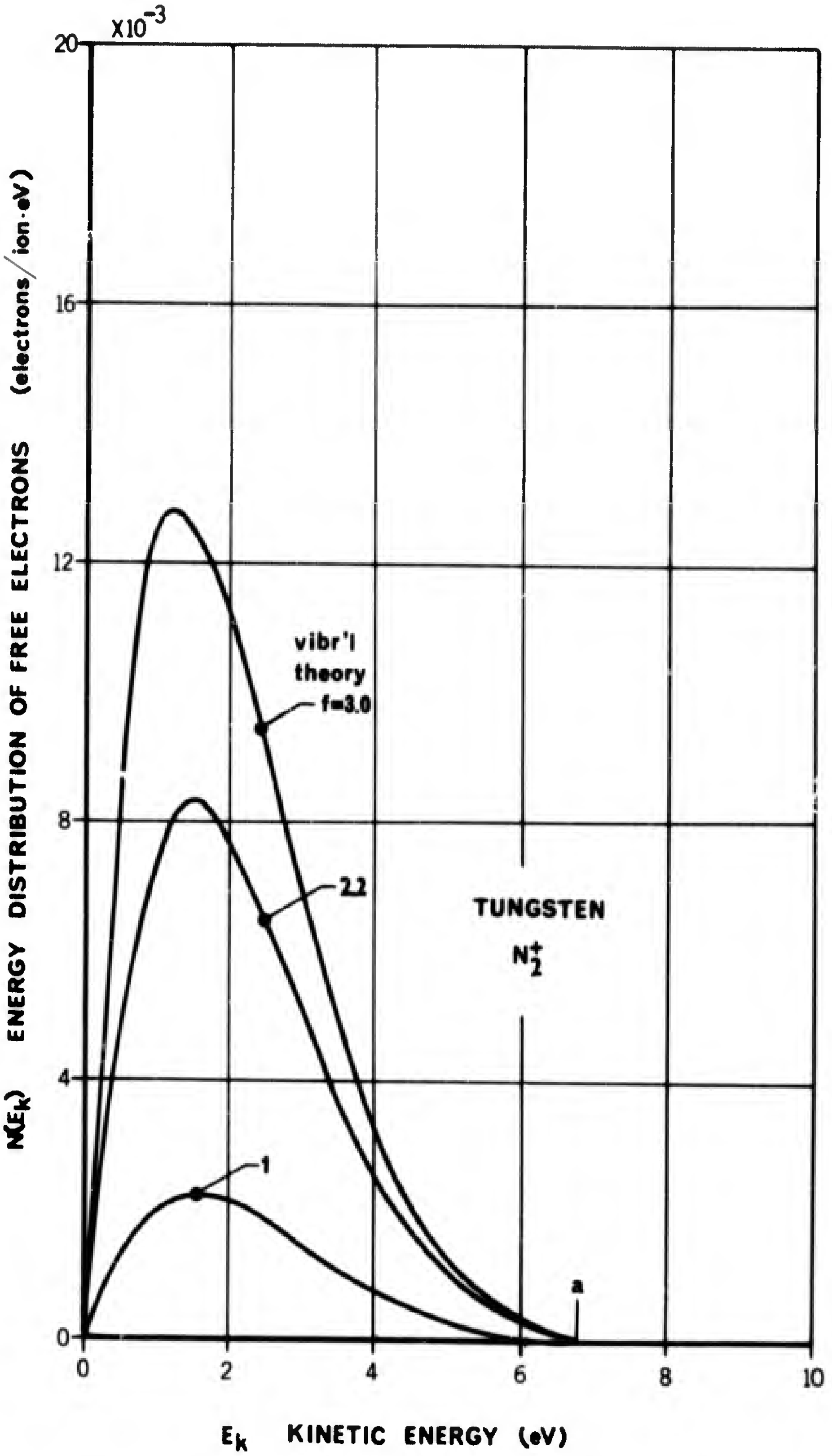

FIG. 50 ENERGY DISTRIBUTION FUNCTIONS OF FREE ELECTRONS PRODUCED BY THE AUGER NEUTRALIZATION OF N_2^+ IONS AT A CLEAN TUNGSTEN SURFACE FOR THE THREE VALUES OF THE ESCAPE FUNCTION PARAMETER f.

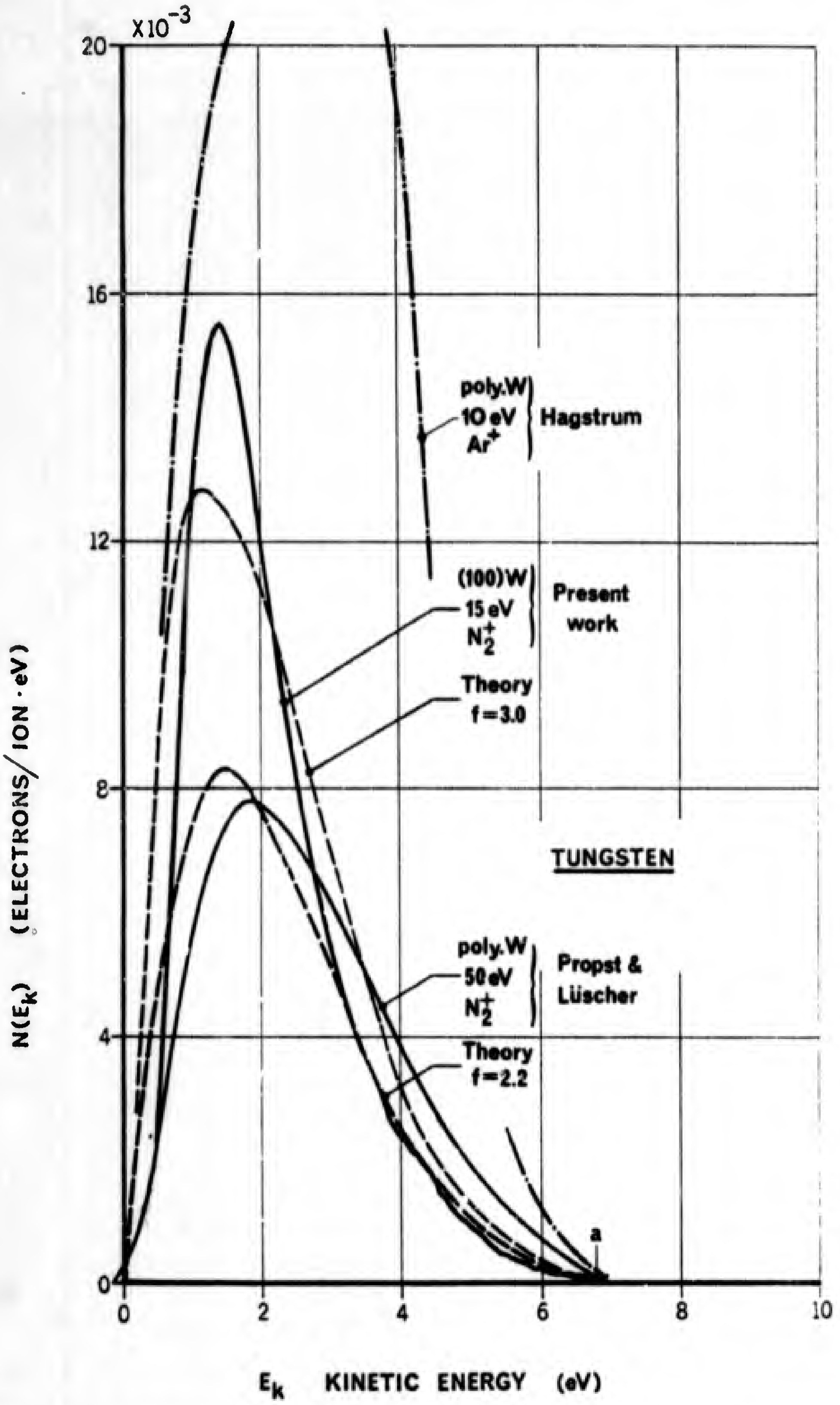

FIG. 51 A COMPARISON OF EXPERIMENTAL AND THEORETICAL ENERGY DISTRIBUTION FUNCTIONS FOR THE PRESENT WORK AND THAT OF PROPST AND LUSCHER (REF. 19).

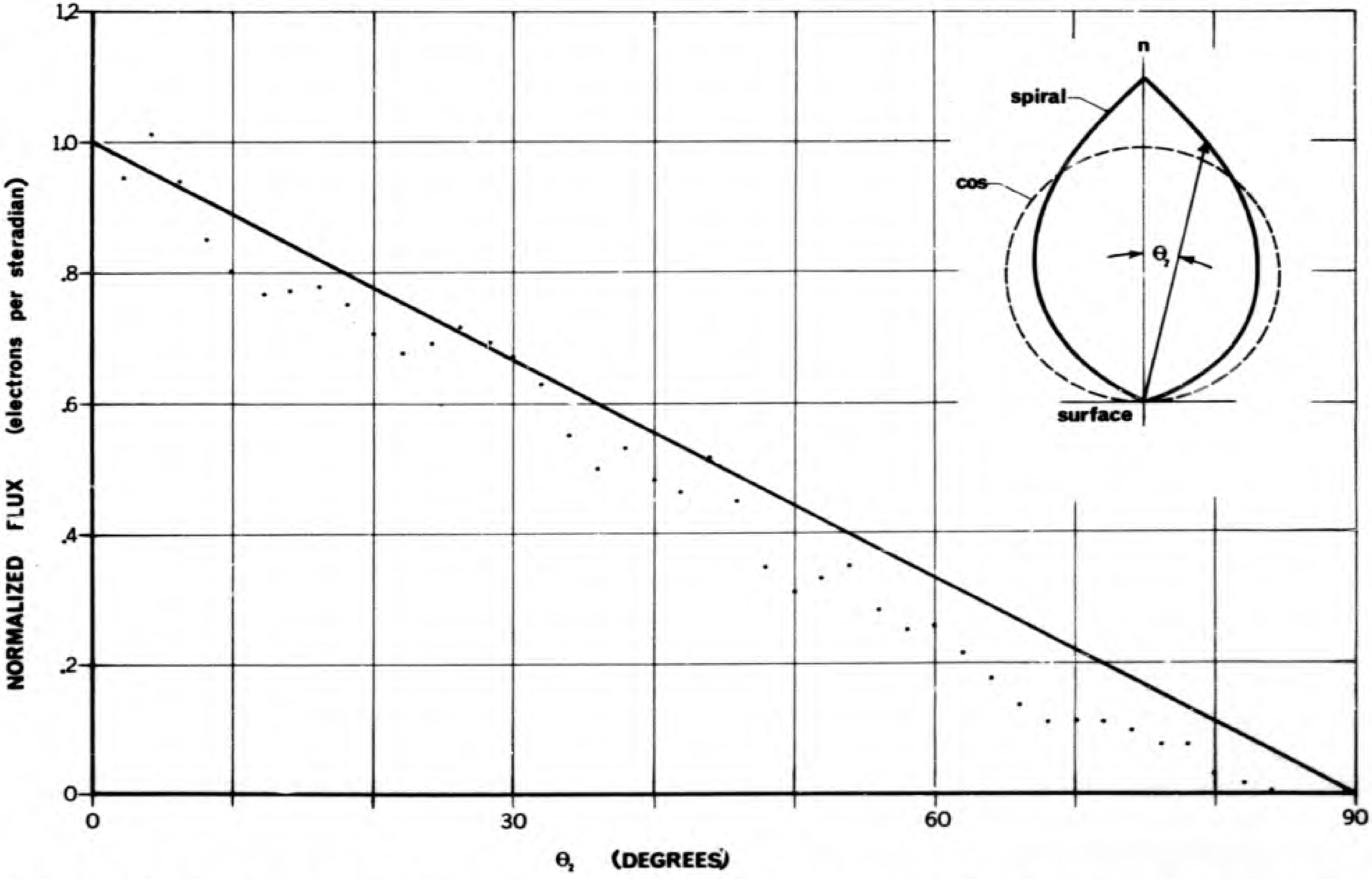

FIG. 52 THE RESULT OF THE CALCULATION OF THE SPATIAL DISTRIBUTION OF FREE ELECTRONS FOR THE NITROGEN-TUNGSTEN SYSTEM ASSUMING f=2. 2

UNCLASSIFIED

Security Classification

DOCUMENT CONTROL DATA - R&D

(Security classification of title, body of abstract and indexing annotation must be entered when the overall report is classified)

1. ORIGINATING ACTIVITY *(Corporate author)* Institute for Aerospace Studies University of Toronto Toronto, Canada	2a. REPORT SECURITY CLASSIFICATION UNCLASSIFIED 2b. GROUP

3. REPORT TITLE
The Interaction of Low-Energy Atmospheric Ions with Controlled Surfaces.

4. DESCRIPTIVE NOTES *(Type of report and inclusive dates)*
Final Report

5. AUTHOR(S) *(Last name, first name, initial)*
Prince, R. H.
French, J. B.

6. REPORT DATE December 1968	7a. TOTAL NO. OF PAGES 124	7b. NO. OF REFS 50
8a. CONTRACT OR GRANT NO. AF33(615)-3855 b. PROJECT NO. c. d.	9a. ORIGINATOR'S REPORT NUMBER(S) UTIAS Report No. 133 9b. OTHER REPORT NO(S) *(Any other numbers that may be assigned this report)* AFFDL-TR-68-148	

10. AVAILABILITY/LIMITATION NOTICES
This document has been approved for public release and sale; its distribution is unlimited.

11. SUPPLEMENTARY NOTES N(+), H2(+)	12. SPONSORING MILITARY ACTIVITY Air Force Flight Dynamics Laboratory (AFSC) Wright-Patterson Air Force Base, Ohio 45433

13. ABSTRACT

The ejection of electrons associated with the Auger Neutralization of N_2^+, H_2^+, and N^+ ions at the (100) face of a tungsten single crystal and a polycrystalline molybdenum surface ~~has been~~ studied for the first time in the energy range 10 to 30 eV under controlled surface conditions. The dependence of the electron yields and energy distributions on ion energy ~~has been~~ investigated in detail for the above ion-surface combinations. The combination of ultrahigh vacuum techniques to lengthen the time required to reach adsorption equilibrium after flashing, and special guarding and analog data-reduction techniques to reduce instrumentation time response, permitted the study of transient adsorption effects as well as the more usual equilibrium studies. Surface contamination was inferred using the measurement of work function which is sensitive to surface adsorption levels. The fact that the electron yields for diatomic ions are considerably lower than those for the inert gas ions treated well by Hagstrum's theory led Propst and Luscher to propose that the neutralized ion may be vibrationally excited as a consequence of the interaction. ~~They suggested a qualitative procedure by which the inert-gas theory could be modified.~~ In the present report, a quantitative calculation ~~has been~~ performed in this low-energy regime for which kinetic broadening effects may be safely neglected. The simplified theoretical treatment provides good agreement with Propst and Luscher's data for 50 eV N_2^+ ions on polycrystalline tungsten, using a value of the escape parameter f (the anisotropy of excited metal electrons) taken from Hagstrum's work. A slightly larger anisotropy permits good agreement with the present data for the (100) face of a tungsten single crystal.

DD FORM 1 JAN 64 1473

UNCLASSIFIED

Security Classification

14. KEY WORDS	LINK A ROLE	LINK A WT	LINK B ROLE	LINK B WT	LINK C ROLE	LINK C WT
Ion-Surface Interactions						
Ion Beams						
Auger Neutralization						
Secondary Electron Emission						

INSTRUCTIONS

1. ORIGINATING ACTIVITY: Enter the name and address of the contractor, subcontractor, grantee, Department of Defense activity or other organization *(corporate author)* issuing the report.

2*a*. REPORT SECURITY CLASSIFICATION: Enter the overall security classification of the report. Indicate whether "Restricted Data" is included. Marking is to be in accordance with appropriate security regulations.

2*b*. GROUP: Automatic downgrading is specified in DoD Directive 5200.10 and Armed Forces Industrial Manual. Enter the group number. Also, when applicable, show that optional markings have been used for Group 3 and Group 4 as authorized.

3. REPORT TITLE: Enter the complete report title in all capital letters. Titles in all cases should be unclassified. If a meaningful title cannot be selected without classification, show title classification in all capitals in parenthesis immediately following the title.

4. DESCRIPTIVE NOTES: If appropriate, enter the type of report, e.g., interim, progress, summary, annual, or final. Give the inclusive dates when a specific reporting period is covered.

5. AUTHOR(S): Enter the name(s) of author(s) as shown on or in the report. Enter last name, first name, middle initial. If military, show rank and branch of service. The name of the principal author is an absolute minimum requirement.

6. REPORT DATE: Enter the date of the report as day, month, year; or month, year. If more than one date appears on the report, use date of publication.

7*a*. TOTAL NUMBER OF PAGES: The total page count should follow normal pagination procedures, i.e., enter the number of pages containing information.

7*b*. NUMBER OF REFERENCES: Enter the total number of references cited in the report.

8*a*. CONTRACT OR GRANT NUMBER: If appropriate, enter the applicable number of the contract or grant under which the report was written.

8*b*, 8*c*, & 8*d*. PROJECT NUMBER: Enter the appropriate military department identification, such as project number, subproject number, system numbers, task number, etc.

9*a*. ORIGINATOR'S REPORT NUMBER(S): Enter the official report number by which the document will be identified and controlled by the originating activity. This number must be unique to this report.

9*b*. OTHER REPORT NUMBER(S): If the report has been assigned any other report numbers *(either by the originator or by the sponsor)*, also enter this number(s).

10. AVAILABILITY/LIMITATION NOTICES: Enter any limitations on further dissemination of the report, other than those imposed by security classification, using standard statements such as:

(1) "Qualified requesters may obtain copies of this report from DDC."

(2) "Foreign announcement and dissemination of this report by DDC is not authorized."

(3) "U. S. Government agencies may obtain copies of this report directly from DDC. Other qualified DDC users shall request through
________________________________."

(4) "U. S. military agencies may obtain copies of this report directly from DDC. Other qualified users shall request through
________________________________."

(5) "All distribution of this report is controlled. Qualified DDC users shall request through
________________________________."

If the report has been furnished to the Office of Technical Services, Department of Commerce, for sale to the public, indicate this fact and enter the price, if known.

11. SUPPLEMENTARY NOTES: Use for additional explanatory notes.

12. SPONSORING MILITARY ACTIVITY: Enter the name of the departmental project office or laboratory sponsoring *(paying for)* the research and development. Include address.

13. ABSTRACT: Enter an abstract giving a brief and factual summary of the document indicative of the report, even though it may also appear elsewhere in the body of the technical report. If additional space is required, a continuation sheet shall be attached.

It is highly desirable that the abstract of classified reports be unclassified. Each paragraph of the abstract shall end with an indication of the military security classification of the information in the paragraph, represented as *(TS)*, *(S)*, *(C)*, or *(U)*.

There is no limitation on the length of the abstract. However, the suggested length is from 150 to 225 words.

14. KEY WORDS: Key words are technically meaningful terms or short phrases that characterize a report and may be used as index entries for cataloging the report. Key words must be selected so that no security classification is required. Identifiers, such as equipment model designation, trade name, military project code name, geographic location, may be used as key words but will be followed by an indication of technical context. The assignment of links, rules, and weights is optional.